Dissertation

submitted to the

Combined Faculties for the Natural Sciences and for Mathematics

of the Ruperto-Carola University of Heidelberg, Germany

for the degree of

Doctor of Natural Sciences

Put forward by

M.Sc. Olga Zacharopoulou

born in Athens, Greece

oral examination: 13.12.2010

On the Origin of the Unusually Hard γ-ray Spectra of TeV Blazars

Referees:

Prof. Dr. Felix Aharonian

PD Dr. Christian Fendt

to my grandmother

Abstract

The observed Very High Energy (VHE) spectra from blazars may be significantly modified due to interactions of γ-rays with intergalactic radiation fields. To study the emission production in these kind of objects, one should reconstruct the intrinsic spectra using an Extragalactic Background Light (EBL) model. Interestingly, this correction often leads to unusually hard spectra. In this dissertation we take into account the EBL absorption by using different models to reconstruct blazars' spectra and we study the formation of broad-band spectra in the framework of a proton synchrotron scenario with non-negligible $\gamma\gamma$ absorption in the production region. This internal absorption leads to rather hard VHE spectra. Moreover, a significant fraction of the energy absorbed in the VHE band may be transferred into secondary electron-positron pairs providing an additional radiation channel that explains the observed radiation in the Optical/X-ray regimes. In order to demonstrate the potential of the model, we model two relatively distant blazars, 1ES 0229+200 (z=0.1396) and 3C 66A (z=0.444). In addition, we perform numerical simulations using relativistic Magnetohydrodynamic (MHD) in time variable injection setup, in an attempt to understand better the conditions under which radiation is produced in relativistic jets.

Zusammenfassung

Die Wechselwirkung hoch-energetischer (VHE) Gammastrahlen mit dem intergalaktischen Strahlungsfeld kann die beobachteten, Hochenergie-Spektren von Blazaren signifikant beeinflussen. Um die Entstehung der Strahlung in diesen Objekten genauer untersuchen zu können, muss man daher die intrinsischen Spektren mit einem Extragalaktischen Strahlungshintergrund Model (EBL) rekonstruieren. Diese Korrektur führt interessanterweise oft zu ungewöhnlich harten Quellspektren. In der vorliegenden Arbeit wird diese EBL-Korrektur anhand verschiedener Modelle vorgenommen. Wir studieren dabei die erhaltenen, intrinsischen Breitband-Spektren im Kontext eines Proton-Synchrotronstrahlung-Modells mit nicht-vernachlässigbarer Gamma-Gamma-Absorption in der Quellregion selbst. Wie sich zeigt, können sich hierbei sehr harte VHE Spektren ausbilden. Darüberhinaus kann ein signifikanter Anteil der im VHE Bereich absorbierten Energie in (sekundäre) Elektron-Positron Paarbildung übertragen werden. Dies kann eine Erklärung der beobachteten Strahlung im optischen bzw. Röntgen-Bereich ermäglichen. Wir weisen das Potential eines derartigen Modells durch Anwendung auf die beiden, relativ entfernten Blazare, 1ES 0229+200 (z=0.1396) und 3C 66A (z=0.444), nach. Zusätzlich führen wir numerische MHD-Simulationen mit zeitlich-variabler Injektion durch, um die Bedingungen unter denen Strahlung in relativistischen Jets erzeugt wird besser verstehen zu können.

Contents

Contents

Contents

4

List of Figures

List of Figures

List of Tables

List of Tables

10

Introduction

> Man is not born to solve the problems of the universe,
> but to find out where the problems begin,
> and then to take his stand within the limits of the intelligible.
> *-Johann Wolfgang von Goethe*

Over the last few years a number of Active Galactic Nuclei (AGN) with redshifts $z \geq 0.1$ have been detected in the VHE regime ($E \geq 100\,\mathrm{GeV}$)[1]. The fact of detection of VHE gamma-rays from such distant objects raises questions on the intensity and spectral shape of the Extragalactic Background Light (EBL). EBL consists of the light coming from stars (UV/O-regime) and a component in the IR-region coming from the absorbed and re-emitted star light by dust. γ-rays are significantly absorbed while traveling over cosmological distances due to pair-production interactions with the EBL photons (Nikishov, 1962; Gould & Schréder, 1967). The level of attenuation depends strongly on the intensity, spectral shape and redshift-dependence of EBL, factors that needs to be estimated in order to obtain the intrinsic AGN spectra. However, direct measurements of EBL contain large uncertainties especially in the mid-infrared region because of dominant foregrounds (see for a review Hauser & Dwek, 2001a; Hauser et al., 1998). Theoretical calculations are not robust neither since they contain several assumptions on

---

[1]see *http://tevcat.uchicago.edu/* for an updated list of VHE gamma-ray sources

the formation and evolution of galaxies. The only robust conclusion about the EBL spectrum is its lower limits derived from galaxy counts (Madau & Pozzetti, 2000). Differences in the theoretical modeling of processes result in different EBL models (see e.g. Primack et al., 2008; Kneiske & Dole, 2010; Franceschini et al., 2008; Dominguez et al., 2010).

The mean free path of γ-rays due to interactions with EBL strongly depends on energy, therefore the intergalactic absorption leads not only to the attenuation of the absolute fluxes, but also changes significantly the spectral shape of γ-rays. The proper understanding of spectral deformation is crucial for correct interpretation of VHE observations of distant AGN. It is important to note that because of strong Doppler boosting of non-thermal emission, $F_\gamma \propto \delta^4$, γ-ray emission from the brightest blazars remain detectable even after severe intergalactic absorption. Thus the fact of intergalactic absorption alone does not allow robust constraints on the EBL models. In this regard, the distortion of the initial spectral shape of gamma-rays contains more information. The optical depth in the absorption regime is $\tau \geq 1$, so even a slight change of the EBL flux can lead to strong change in the energy-dependent spectral deformation factor $exp[-\tau(E)]$. This allows quite meaningful upper limits on EBL at relevant energy bands, based on a condition that the intrinsic spectrum of γ-rays should have a decent form, e.g. to be not much harder than E^{-2}. On the other hand, the absorption corrected VHE γ-ray spectra of some AGN with $z \geq 0.1$ in some cases appear very hard with a power-law photon index quite close to the hardest conventional value of $\Gamma_{ini} = 1.5$, even for very low EBL models (Aharonian et al., 2006; Franceschini et al., 2008). In the case of slightly higher flux of EBL, the reconstructed spectra are getting harder, with $\Gamma_{ini} < 1.5$.

Although currently there is a general consensus in the community that EBL should be quite close to the robust lower limit derived from the galaxy counts, the possibility of slightly higher fluxes of EBL cannot be excluded. In particular, using Spitzer data and a profile fitting of the faint fringes of galaxies, Levenson & Wright (2008) claimed a new fiducial value for the contribu-

tion of galaxies to the EBL at $3.6\,\mu$m of $9.0^{+1.7}_{-0.9}\,$nWm^{-2}sr^{-1}, which exceeds by a factor of ~ 1.6 the corresponding flux in the EBL model suggested by Franceschini et al. (2008). Following Levenson & Wright (2008), Krennrich et al. (2008) indicated that for this EBL intensity the initial (absorption corrected) VHE spectra of distant blazars 1ES 0229+200, 1ES 1218+30.4 and 1ES 1101-232 (located at redshifts $z = 0.1396$, 0.182 and 0.186, respectively) would have a photon index ≤ 1.3. This result apparently challenges the conventional models for VHE production in AGN.

Generally, the X- and γ-ray non-thermal emission of blazars is interpreted as a sum of synchrotron and IC components of radiation of relativistic electrons in the framework of the so-called synchrotron self-Compton (SSC) or external Compton scenarios. In the case of radiation-efficient models, i.e. assuming *radiatively cooled* particle distribution, the IC spectrum in the Thomson limit is expected to be steeper than the power law distribution with photon index 1.5. This limit does not depend on the electron initial (injection) spectrum and can be achieved, for example, in the case of a mono-energetic injection. At higher energies, the gamma-ray spectrum becomes steeper due to the Klein-Nishina effect. We note however, that typically the spectra obtained in the frameworks of SSC scenario are steeper, with photon indexes ~ 2. Therefore, the spectrum with photon index $\Gamma = 1.5$ is often referred as the hardest spectrum allowed by standard blazar models. However, at expense of radiation efficiency it is possible to produce harder VHE spectra being still in the framework of SSC models, for example assuming high lower-energy cutoff in the electron spectrum. In particular, Katarzyński et al. (2006) have proposed a SSC scenario which allows photon index as small as $\Gamma_{\mathrm{ini}} = 0.7$. The postulation such a cutoff in the electron spectrum implies very low efficiency of radiative cooling which, in its turn, increases the requirements to the energy in accelerated electrons and, on the hand, requires very small magnetic field. Thus, in such scenarios we face a significant (by orders of magnitude) deviation from equipartition, $W_{\mathrm{e}} >> W_{\mathrm{B}}$.

Alternatively, Aharonian et al. (2008) have suggested a scenario for the

formation of VHE spectra of almost *arbitrary* hardness by involving additional absorption of VHE γ-rays interacting with dense radiation fields in the vicinity of the γ-ray production region. The key element in this scenario is the presence of a photon field with a narrow energy distribution or with a sharp low energy cut-off around $> 10\,\mathrm{eV}$. In this case, γ-rays are attenuated most effectively at energies $\sim 100\,\mathrm{GeV}$ compare to energies $\sim 1-10\,\mathrm{TeV}$, and therefore, for large optical depths ($\tau \geq 1$), the spectrum in the VHE band should gradually harden towards higher energies (for detail, see Aharonian et al., 2008).

While, the absorption of high energy γ-rays in the inner parts of AGN jets generally is possible, or even unavoidable (McBreen, 1979; Liu & Bai, 2006; Reimer, 2007; Sitarek & Bednarek, 2008; Liu et al., 2008; Bai et al., 2009; Tavecchio & Mazin, 2009), the detailed modeling of this process requires additional assumptions concerning the presence of low-frequency radiation fields, the location and size of the gamma-ray production region, the Doppler factor of the jet, *etc.* We note that currently there is no observational evidence excluding the photon field properties required by Aharonian et al. (2008), also in the case of BL Lacs. Remarkably, the internal absorption hypothesis provides an alternative explanation for the non-thermal X-ray emission, namely as synchrotron radiation of secondary (pair-produced) electrons (Aharonian et al., 2008), which suggests a possible solution to the problem of low acceleration efficiency in leptonic models of high energy emission of blazars (Costamante et al., 2009).

In the original paper, Aharonian et al. (2008) presented a general description of the scenario with calculations of model SEDs, but the obtained spectra were not compared with available data. In the present dissertation we discuss the multiwavelength properties of radiation in the framework of the internal absorption scenario, and apply the model to the data of two distant AGN (1ES 0229+200 and 3C 66A, with redshifts $z = 0.1396$ and $z = 0.444$, respectively, detected in TeV energy band (Aharonian et al., 2007; Aliu et al., 2009; Acciari et al., 2009; Reyes et al., 2009). We start from the observa-

tional data that need to be reconstructed because of the EBL absorption. We demonstrate how sensitive is the absorption to the EBL spectrum by using different models. Two of the reconstructed spectra (using two different EBL spectra) are chosen for each source to apply the theoretical γ-ray production model to. We adopt the proton synchrotron radiation as the source of primary γ-rays which leave the source after significant absorption due to γ-γ pair production both in the γ-ray production region and in the surroundings. The absorption-created pairs in the production region give rise to an additional lower energy non-thermal component through synchrotron radiation of secondary electrons. The latter is calculated self-consistently and depends on the primary γ-ray spectrum, the target photon field and the relativistic motion of the γ-ray production region.

In Chapter 1 an overview of the AGN is given and especially of the blazars. The radiation and absorption processes that take place in such extreme environments are presented in Chapter 2, while in Chapter 3 there is an introduction of the instruments with which we detect the γ-rays from astrophysical objects. There is a discussion on the space- and ground-based telescopes, how γ-ray photons interact with the Earth's atmosphere when they enter it (air-showers) and what are the advantages and disadvantages of each method of observation.

The interaction of EBL with high energy photons is discussed in Chapter 4. The different theoretical models and their assumptions are presented, as well as examples on how different EBL spectra result into different reconstructed blazar spectra. Once the reconstructed blazar spectra is ready we move into Chapter 5 where our proton-synchrotron model is presented in detail. The results of the successful fitting of 1ES 0229+200 and 3C 66A multiwavelength spectra are presented in Chapter 6.

Chapter 7 deals with a different topic, MHD jets. AGN are associated with relativistic jets and synchrotron radiation. Compression of the magnetic field is consider to produce the right environment for emission of synchrotron radiation. Here we run some numerical simulations solving the relativistic

MHD equations to understand how we can obtain strong shocks that will lead to radiation. The results presented are only preliminary but promising. A jet configuration with and without variable injection is discussed, as well as the case of different plasma β parameters.

Chapter 1

AGN - Blazars

The night has a thousand eyes,
And the day but one;
Yet the light of the bright world dies,
With the dying Sun.
-Francis William Bourdillon

Normal galaxies emit in UV and Optical wavebands since their light comes from stars. However, around one-in-ten galaxies – the "active galaxies" – host an AGN in their centre. This is a compact region (less than $0.1\,pc$) that shows higher emissivity (in most or even all of the wavebands) than the rest of the galaxy. The nuclei of active galaxies are spatially unresolved, even for nearby AGN. The only parts of AGN that are resolvable, sometimes, in the radio are their jets, observed to extend to hundreds of kpc. AGN include the most powerful, steady sources of luminosity in the universe. Their apparent luminosity can be up to $10^{47-48}\,erg/s$ for some distant examples. Their emission is spread across the electromagnetic spectrum, often peaking in the UV, but with significant luminosity in the X-ray and infrared bands. The favoured picture of AGN holds that they each host a massive black hole of
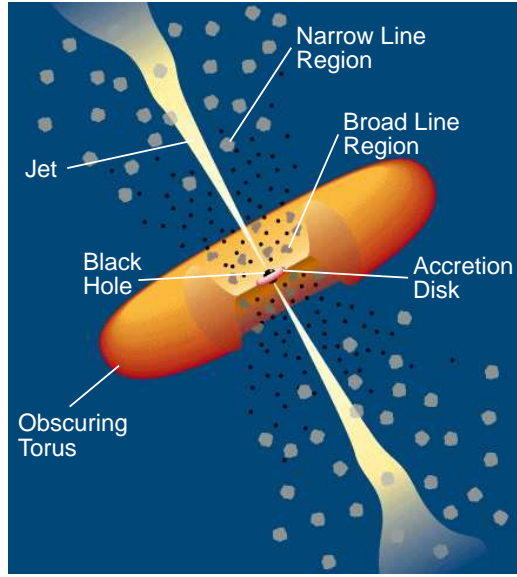
Figure 1.1 The AGN unification scheme for radio loud galaxies (Urry & Padovani, 1995).

mass $\gtrsim 10^8 \, M_\odot$ in their centre which is surrounded by an accretion disc. The matter falling into the black hole emits the excess of radiation we observe.

In Fig. 1.1 one can see the main components of the AGN paradigm (Urry & Padovani, 1995). In the centre there is a massive black hole surrounded by an accretion disc of size $2-100$ Schwarzschild radii, R_{sw}. Matter is accreting on to the black hole. Around the accretion disc, there is a torus of dust that extends up to $10^3 \, R_{sw}$ and surrounds the main region of the active galaxy, obscuring the central region from us. Within distances up to $10^3 \, R_{sw}$ from the centre are found the Broad Line Regions (BLR) thought to be clouds of fast-moving gas which are responsible for the broad emission lines observed in the spectra of some galaxies. At distances of $10^4 - 10^6 \, R_{sw}$ from the black hole are found Narrow Line Regions (NLR), slow moving clouds of gas, which are responsible for the narrow emission lines observed in some cases. Perpendicular to the accretion disc, outflows may be observed. These may be highly collimated into a relativistic jet.

1.1 AGN Classification

AGN are observed with a variety of characteristics, e.g. with or without emission lines, with or without γ-ray emission. The presence of an accretion disc and of an outflow – which break spherical symmetry – imply that even otherwise identical AGN may appear different for purely geometrical reasons. Consequently, a "unification" scheme (Urry & Padovani, 1995) has been postulated that asserts that AGN are all members of a single class of object (which differ only in terms of viewing angles and the degree to which their outflows are collimated).

In Fig. 1.2 one can see the different geometries. The first categorization depends on the degree of outflow collimation. If an outflow is loosely collimated and creates two cones with large opening angle, a radio-quiet source results, i.e., Seyfert galaxies and Broad Absorption Line Quasi Stellar Objects (QSO). If the outflow is collimated then a radio-loud source results, narrow line radio galaxies (NLRG) (Fanaroff-Riley I and II), broad line radio galaxies (BLRG), steep spectrum radio Quasars (SSRQ), BL Lac Objects and flat spectrum radio Quasarss (FSRQs). In practice, a working definition of radio-quiet or radio-loud sources is that the radio/optical flux ratio (at 5 GHz and in B band) is smaller or larger than 10, respectively. The radio loud sources constitute $5-10\%$ of the AGN class.

The other relevant parameter is the angle at which we observe the source. Variation of this results in different optical spectra. In the case of radio-quiet active galaxies, if the angle is big then we get Seyfert 1 or Seyfert 2-type galaxies. In the spectrum of Seyfert 2 galaxies we observe narrow lines and according to Fig. 1.1, this is because their torii are almost parallel to our line of sight so that the NLRs can be observed whereas the BLRs are obscured (and broad lines are missing from their spectra). In Seyfert 1 galaxies, the torus and our line of sight form such an angle that the BLRs are visible and in their spectra we observe both broad and narrow lines. In the case that the torus is almost perpendicular to us we observe a QSO. Here the outflow is moving towards the observer and the radiation emitted by matter falling on
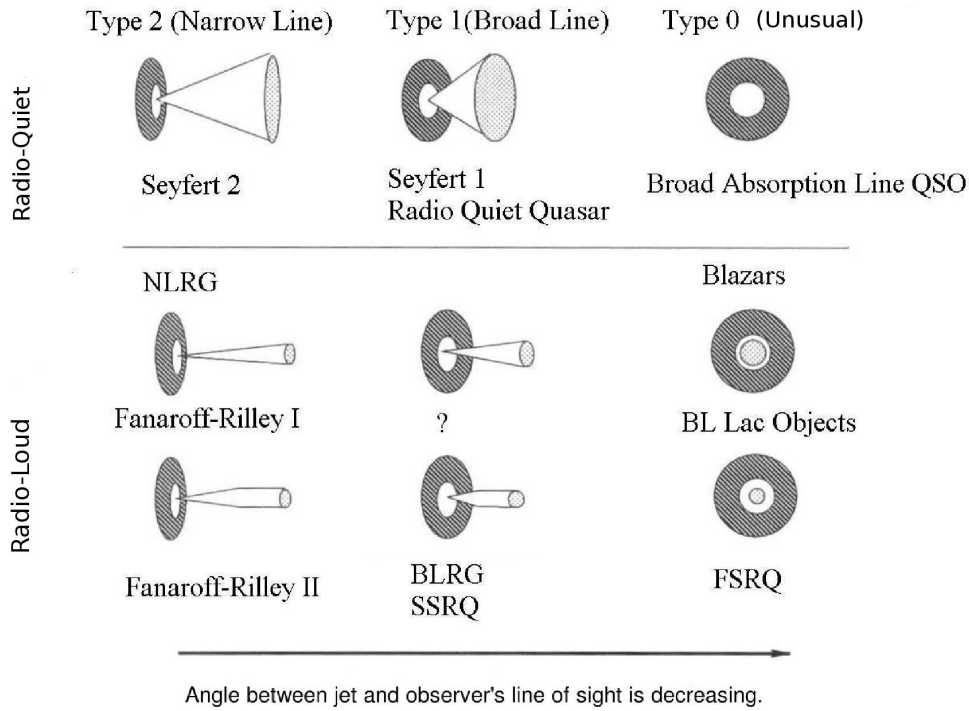
Figure 1.2 The AGN classification (Urry & Padovani, 1995).

to the black hole is stronger than the disc radiation and that coming from the surrounding galaxy.

On the other hand, radio-loud galaxies have collimated outflows. Fanaroff-Riley I galaxies have their jets almost perpendicular to the observer's line of sight. If a jet is moving towards us a (strongly-polarized and luminous) BL Lac Object is observed. Fanaroff-Riley II galaxies are similar to Fanaroff-Riley I, with the jet perpendicular to the observer, but have less collimated jets. As the angle between jet and line of sight is decreased, we get BLRG or SSRQ and when the angle is close to 0°, FSRQs result. The observational advantage of BLRG is that the observer is not blinded by non-thermal emission coming from the jet and can observe both jet and accretion disc. Moreover, unlike the NLRG, these are not generally obscured by large torii and offer a direct view of their inner regions.

A small number of radio loud AGN show lack of strong emission or ab-

sorption lines; they are called "BL Lac" objects after the prototype of this class, BL Lacertae. These objects are similar to FSRQs, except from their almost featureless spectra; they both display compact radio cores, flat radio spectra, high polarization (BL Lac often more than FSRQs), some times superluminal motion, high brightness temperatures and a high and rapid variability. Since these two classes of objects are so similar, they are called together "Blazars"(blazing quasi-stellar objects).

1.2 γ-rays from AGN

Not all AGN are detectable in γ-rays, e.g. the Seyfert galaxies emit only soft γ-rays, $0.1 - 1\,MeV$. If we divide AGN into radio-loud and -quiet, then only radio-loud AGN show significant emission of γ-rays. So if we are interested in γ-rays from AGN we need consider Quasars and BL Lac objects (which both produce emission up to $10\,TeV$).

The accepted picture of γ-ray production in AGN is the following: Disc material slowly accretes on to the black hole. Due to friction, the disc radiates into infrared and X-rays. At the same time electrons are accelerated and give us synchrotron radiation in X-rays. These energetic electrons also interact with the soft photons present because of disc radiation and produce γ-rays through inverse Compton emission.

Since γ-rays can interact through pair-production on the soft photon fields, one could claim that the reason we do not observe γ-rays in all of the active galaxies is because the optical depth of the $\gamma\gamma$ interaction is high and all of the radiation is attenuated. In the case of Seyferts, however, this can not be true. Their luminosity is quite low and any γ-rays formed there could escape. So we may infer that γ-ray production does not occur. If the non detection of γ-rays in the radio-quiet galaxies is *not* due to the low sensitivity of γ-ray telescopes, then it should be connected with the absence of collimated jets. In the case of some radio-loud galaxies with no detectable γ-rays, this could be because of the orientation of the jet. Blazars and Quasars

have jets pointing at us, and the radiation from these jets is boosted and is therefore easier to observe.

There is a possibility that the radio-quiet galaxies emit γ-rays but that their emission is very faint. Sources are easier to detect when (a) they have collimated outflows and high photon fluxes and (b) they have strong, non-thermal emission. In the case of radio-quiet AGN (a) could be true, but not (b). The ratio between the luminosity in the radio and in the optical, L_{radio}/L_{opt} is considered to be connected with the ratio of the non thermal to the thermal luminosity, $L_{non-thermal}/L_{thermal}$. But the radio-quiet galaxies have lower luminosity in the radio than in the optical, so their ratio $L_{non-thermal}/L_{thermal}$ is smaller than what the radio-loud have. This does not necessarily mean the absence of γ-ray emission but the emission could be very faint. Future observations with instruments of higher sensitivity could give us more information on these objects.

Some AGN show emission at GeV energies and in others the spectrum extends up to some TeV. One of the reasons why some sources do not show VHE emission could be absorption of γ-rays by the EBL. This is more probable for sources with high redshift since the optical depth increases with distance. For more details on the topic see Chapter 4. Another reason for the absence of TeV γ-rays could be differences in some physical properties. According to the Spectral Energy Distribution (SED) of blazars, we can divide these objects into "Red" Blazars or Low-energy peaked Blazars (LBL) and "Blue" or High-energy peaked Blazars (HBL). All Blazar spectra show two peaks. However, for the ones coming from "Red" Blazars, like 3C 279, the first peak is in the infrared or optical and the second one is in the energy range around 1 GeV. On the other hand, in the "Blue" Blazars spectra, like Mrk 421, the first peak is in the ultraviolet or in soft X-rays and the second one in the energy range around 1 TeV. Obviously, only the "Blue" Blazars give us photons of TeV energies. The first peak in the HBL is at energies at least 4 times higher than the first peak in the LBL. If we assume that the first peak comes from synchrotron radiation, then the maximum of it will be in the

frequency $\nu_{syn} \propto \gamma_{max}^2 B \delta$, where γ_{max} is the maximum Lorentz factor of the particles, B is the magnetic field amplitude and δ the Doppler factor. If the second peak is produced by inverse Compton scattering, then the maximum of the emission is proportional to ν_{syn} and the higher this frequency is, the higher the energy of the photons produced by inverse Compton scattering will be. The processes producing γ-rays in the HBL and in the LBL are common. Therefore, depending on the combination of the parameters B, γ_{max} and δ, we could have the right conditions for high values of ν_{syn} or equivalently the right conditions for TeV emission.

1.3   Blazars properties

As previously mentioned, blazars constitute a small subset of AGN whose members are less than a few percent of the total AGN population. The characteristics that distinguish them from the rest of the AGN are the following (Miller, 1989; Bregman, 1990):

- Their emission in the IR-optical-UV is a smooth continuum from a stellar-like nucleus.

- There is high optical polarisation ($p > 3\%$).

- There is rapid optical variability on a time scale of days or less in both flux and polarization.

- The spectrum in radio is a strong and time-variable continuum.

Blazars are further subdivided into BL Lac objects and optically violent variables (OVVs). When emission lines are unusually weak compared to the continuum, the source is classified as a BL Lac object. This is also the reason why in many cases there are large uncertainties in the estimation of redshift in BL Lacs. When lines are detectable, the redshifts tend to be small ($z \lesssim 0.1$). On the other hand, in the case of the OVVs, one can see

broad emission lines, except from periods with intense continuum flares. The redshift of OVVs is usually large ($z \gtrsim 0.5$).

The IR brightness temperatures of blazars are sometimes found to be greater than $10^6 \, K$, and the radio brightness temperatures of these sources are in excess of $10^{12} \, K$, in some cases greater than $10^{19} \, K$. Some blazars also show superluminal motion.

Variability in all spectral bands and even correlated variabilities in different bands are another fundamental observational characteristic of blazars. Their presence can give us insights into the size of the source since $R \lesssim c\Delta t$, and, together with the observed flux, we can get information on the photon energy densities. Most of the information can be obtained from the low energy bands because there it is possible and easier to monitor the source for a long time (tens of years). In the radio band blazars usually show long term variability of the order of years and at the same time a rapid one with timescales from days to hours, called IntraDay Variability (IDV). We use fast variability to get estimations on the size of the source since the long term variability could be dominated by radiative cooling or heating or slow changes in the structure of the system. At the same time very fast variabilities (daily) are likely to have an extrinsic origin due to scintillation by interstellar clouds. Approximately, the variability in relation with the observed frequency is $\Delta t \propto \nu^{-1/2}$.

1.4   Models of Blazar Emission

As previously discussed, blazars' SED show two peaks. The first one in low energies is widely accepted to come from synchrotron radiation by relativistic electrons. However, there are different scenarios for the origin of the high energy peak. Indeed, there are two fundamentally different approaches to explain it. Its origin could be hadronic or leptonic (Böttcher, 2007).

Leptonic Blazar Models

In leptonic models the high energy peak in the blazar SED comes from the inverse Compton scattering produced by the same relativistic electron population that created the synchrotron peak at the lower energies. It is possible that the up-scattered photons are the same ones forming the low energy peak within the jet, or external photons. The external photons could be photons from the accretion-disc entering the emission region directly or after reprocessing surrounding material like the BLR, or they could be jet synchrotron emission reprocessed by circumnuclear material, infrared emission from the surrounding dust or even synchrotron radiation from other emission regions along the jet. However the γ-rays are produced, they will undergo $\gamma\gamma$ absorption externally and maybe even internally, producing electron-positron pairs. That is why in leptonic models synchrotron self absorption should be estimated for a self-consistent model. Additionally, as the emission region is propagating relativistically along the jet, continuous particle injection and/or acceleration and subsequent radiative and adiabatic cooling and particle escape have to be considered. Nevertheless, blazar spectra and spectral variability has been successfully modeled with time-dependent leptonic jet models.

Hadronic Blazar Models

In these models protons are accelerated to high energies, so they reach the threshold for $p\gamma$ pion production. As a consequence pair cascades are developed through synchrotron emission. These models require high magnetic fields of at least several tens of Gauss, in order for the proton acceleration in ultrarelativistic energies to take place. In such an environment also the synchrotron radiation of the primary protons is important and must be taken into consideration, as well as of secondary muons and mesons. In general, in these models the high energy peak comes from primary proton synchrotron radiation and the low energy peak from the primary and from the secondary

electrons.

According to a variation of these models, the production of high energy γ-rays could come directly from protons. Also in this case the protons are accelerated in very high energies due to strong magnetic fields, but then they produce synchrotron radiation in the TeV regime forming the high energy peak. The low energy peak comes from the primary and the secondary e^-. We are dealing with such a model in this study and as explained thoroughly in the following chapters, internal absorption can be the reason for the generation of a large population of electron-positron pairs whose synchrotron radiation can describe the low energy peak.

Chapter 2

γ-ray Radiation Processes and Absorption Mechanisms in AGN

> In order to make an apple pie from scratch,
> you must first create the universe.
> *-Carl Sagan*

2.1 Production Mechanisms

It is essential to understand the underlying production mechanisms of high energy photons before we continue modeling spectra. So, in this section we are going to discuss the most important ones in astrophysics from which we can get high energy photons, in X- and/or γ-rays. All of these topics are covered in Blumenthal & Gould (1970), Rybicki & Lightman (1986), Aharonian (2004) and Longair (1992).

2.1.1 Bremsstrahlung

Bremsstrahlung radiation means literally "braking radiation" because it is produced by charged particles that are decelerated while they move inside Coulomb fields produced by nuclei or ions. In order to understand fully the process, quantum treatment of the problem is needed, since photons with almost the energy of the particle can be emitted. But in some regimes, the classical case can describe the problem sufficiently and is preferred.

The Bremsstrahlung emission coefficient for electrons of mass m_e interacting with ions of charge $Z_i e$ is

$$
\begin{aligned}
j_\nu &= \frac{8}{3} \left(\frac{2\pi}{3} \right)^{1/2} \frac{Z_i^2 e^6}{m_e^{3/2} c^3 (kT)^{1/2}} g_{ff} n_e n_i e^{-h\nu/kT} \\
&= 5.44 \times 10^{-39} Z_i^2 n_e n_i T^{-1/2} g_{ff} e^{-hn/kT} \quad erg\, cm^{-3} s^{-1} sr^{-1} Hz^{-1} \quad (2.1)
\end{aligned}
$$

where T is the temperature of the Maxwellian velocity distribution of the electrons, g_{ff} is the free-freegaunt factor, a quantum mechanical correction to the classically derived expression for j_ν,

$$
g_{ff} = \frac{\sqrt{3}}{\pi} \left\{ \frac{\ln(2kT)^{3/2}}{\pi e^2 \nu m_e^{1/2}} - \frac{5\gamma}{2} \right\} \tag{2.2}
$$

with γ the Euler's constant, $\gamma = 0.577$.

The average energy loss-rate for the electrons is proportional to the energy of the electron and is given by the equation:

$$
-\frac{d\varepsilon_e}{dt} = \left(\frac{c m_p n}{X_0} \right) \varepsilon_e, \tag{2.3}
$$

where X_0 is the radiation length, $X_0 = 7/9(n\sigma_0)^{-1}$ with σ_0 the cross section of the interaction, which is the average distance over which the relativistic electron loses all but $1/e$ of his energy due to bremsstrahlung radiation. The

lifetime of electrons because of their losses is

$$t_{br} = \frac{\varepsilon_e}{-d\varepsilon_e/dt} \simeq 4 \times 10^7 (n/1 \ cm^{-3})^{-1} \ yr. \tag{2.4}$$

We should note that the lifetime of the electrons does not depend on their energy since $-d\varepsilon_e/dt \propto \varepsilon_e$.

If the distribution of electrons is a power law, then its shape will not change because of energy losses since the lifetime is energy independent. The produced spectrum of photons will be also a power law with the same spectral index as the electrons, when bremsstrahlung is the dominant mechanism for energy losses.

2.1.2 Inverse Compton Scattering

Compton scattering is occurring when a high energy photon is scattering an electron and part of its energy is transfered to the electron. Inverse Compton scattering is the reverse phenomenon. A relativistic electron of energy ε_e moving inside a photon field will scatter photons in higher energies. In the rest frame of the electron (primed quantities), the energy of the photons, ε, appear to be $\varepsilon' = \gamma \varepsilon (1 - \beta \cos \theta)$, and the angle which it sees the photons coming towards it, is given by the equation $\cos \theta' = \frac{\cos \theta - \beta}{1 - \beta \cos \theta}$. From the above it comes out that the minimum and maximum energy of the photons, as seen by the electron, are $\varepsilon_{min} \approx \varepsilon/2\gamma$ for $\theta = 0$ and $\varepsilon_{max} \approx 2\gamma\varepsilon$ for $\theta = \pi$.

Using the four dimension vectors of momentum for the photon and the electron, before and after the scattering, the relation between the energy of the photon after the scattering ε_{final}, before the scattering ε_{init} and the electron energy ε_e is:

$$\frac{\varepsilon_{final}}{\varepsilon_{init}} = \frac{1 - \beta \cos \theta_i}{1 - \beta \cos \theta_f + (\varepsilon_e/(\gamma m_e c^2))(1 - \cos \alpha)} \tag{2.5}$$

where θ_i and θ_f are the angles between the photon and the electron before and after the scattering, respectively, α is the angle between the directions

of the photon before and after the scattering. In the Thomson limit where $\varepsilon_{init} << \gamma m_e c^2$, the photon gets the maximum possible energy in the case of head on scattering, when $\theta_i = \pi$ and $\theta_f = 0$, and that is:

$$\varepsilon_{final} = 4\gamma^2 \varepsilon_i \qquad (2.6)$$

The energy losses for the relativistic electrons in the Thomson regime is:

$$-\left(\frac{dE}{dt}\right) = \frac{4}{3}\sigma_T c U_{ph} \beta^2 \gamma^2 \qquad (2.7)$$

and in the Klein-Nishina regime:

$$-\left(\frac{dE}{dt}\right) = \frac{3}{8}\frac{\sigma_T c n_{ph}}{\omega_0}(\ln b - 11/6) \qquad (2.8)$$

and this is the energy that the photons are gaining from the electrons. U_{ph} is the energy density of the photons.

When the electrons have a power law distribution $N_e(\gamma) = k_e \gamma^{-p}$ for a range of energies $\gamma_{min} \leq \gamma \leq \gamma_{max}$, the total scattered power per unit volume per energy due to the non-thermal power law distribution of the electrons is:

$$I(\varepsilon) = \frac{1}{2}k_e n_0 \sigma_T c \varepsilon_0^{\frac{p-1}{2}} \varepsilon^{-\frac{p-1}{2}} \qquad (2.9)$$

for $\varepsilon_{min} = \frac{4}{3}\varepsilon_0 \gamma_{min}^2$ and $\varepsilon_{max} = \frac{4}{3}\varepsilon_0 \gamma_{max}^2$. The emission is a power law with index $a = \frac{p-1}{2}$.

Inverse Compton scattering is important because indeed it is observed that electrons can upscatter low energy photons in high energies, at the same time electrons are loosing their energy severely when they pass through a photon field. For example electrons with $\gamma = 1000$ will upscatter optical photons of $\nu = 4 \times 10^{14}\ Hz$ to a 10^6 higher energy and they become γ-ray photons of $4 \times 10^{20}\ Hz$.

2.1.3 Synchrotron Radiation

Relativistic charged particles accelerated in strong magnetic fields produce synchrotron radiation. The radiation produced by a particle with mass m and charge q moving through a magnetic field of strength B when its velocity is βc and the angle between its velocity vector and its acceleration is α, is

$$P = \frac{2}{3}\left(\frac{q}{mc^2}\right)^4 c\beta^2 E^2 B^2 \sin\alpha^2, \tag{2.10}$$

where E is the energy of the particle. If the particles are distributed isotropically, then we can integrate the angle α through the solid angle, and the relation 2.10 becomes :

$$P = \frac{4}{3}\left(\frac{q}{mc^2}\right)^4 c\beta^2 E^2 U_B \tag{2.11}$$

where $U_B = B^2/2\mu_0$ is the magnetic field energy density. The critical frequency ν_c of synchrotron radiation is the frequency where most of the energy is emitted and beyond this frequency the spectrum falls off sharply,

$$\nu_c = \frac{3}{2}\frac{qB}{m}\gamma^2 \sin\alpha \tag{2.12}$$

For a power law distribution of relativistic particles, $dN/dE = CE^{-p}$, over the range $E_1 \leq E \leq E_2$ the total power emitted per unit time per unit frequency is

$$P(\nu) = \frac{\sqrt{3}q^3 CB \sin\alpha}{2\pi mc^2(p+1)}\Gamma\left(\frac{p}{4}+\frac{19}{12}\right)\Gamma\left(\frac{p}{4}-\frac{1}{12}\right)\left(\frac{mc\nu}{3qB\sin\alpha}\right)^{-\frac{p-1}{2}} \tag{2.13}$$

where Γ is the $\Gamma(x)$ function. This is a power law spectrum with spectral index

$$\alpha = \frac{p-1}{2} \tag{2.14}$$

In our case we are interested in the radiation from protons since the model we are going to described is based on such. According to Eq. 2.11 $P \propto m^{-4}$, it is clear that the radiation coming from electrons is much higher than the

one coming from protons

$$\frac{P_e}{P_p} = \left(\frac{m_p}{m_e}\right)^4 \simeq 10^{13}, \tag{2.15}$$

since $m_p \simeq 1836 m_e$, when both of the particle species have the same energy. However, the synchrotron cooling time is

$$\tau_{syn} = \frac{E_e}{P} = \frac{\gamma m c^2}{\frac{4}{3}\sigma_T c \gamma^2 U_B} = \frac{6\pi m^4 c^3}{\sigma_T m_e^2 E B^2}, \tag{2.16}$$

where $\sigma_T = \left(\frac{q^2}{mc^2}\right)^2$ is the Thomson cross section. In the case of protons

$$t_{syn} = 4.5 \times 10^4 B_{100}^{-2} E_{19}^{-1} \ s. \tag{2.17}$$

2.1.4 Electron-Positron Annihilation

When an electron collides with a positron, they create two photons, $e^- + e^+ \rightarrow \gamma + \gamma$. In the case that the two primary particles have no kinetic energy, then then two photons are produced having the energy of the particles, 511 keV each. This process is well identified since we observe emission lines from our galaxy in the energy of 511 keV, coming from the annihilation of electrons-positrons.

If positrons are injected with relativistic energies $\varepsilon_+ = E_+/m_e c^2$ in a medium with electrons of density n_e, then the differential spectrum of the produced γ-rays due to their annihilation is:

$$
\begin{aligned}
q_{ann}(E_\gamma) = {} & \frac{3\sigma_T^2 c n_e}{8\varepsilon_+ p_+} \left[\left(\frac{E_\gamma}{\varepsilon_+ + 1 - E_\gamma} + \frac{\varepsilon_+ + 1 - E_\gamma}{E_\gamma} \right) + \right. \\
& \left. 2\left(\frac{1}{E_\gamma} + \frac{1}{\varepsilon_+ + 1 - E_\gamma} \right) - \left(\frac{1}{E_\gamma} + \frac{1}{E_\gamma} + \frac{1}{\varepsilon_+ + 1 - E_\gamma} \right) \right]
\end{aligned}
\tag{2.18}
$$

where $p_+ = \sqrt{\varepsilon_+^2 - 1}$ is the dimensionless momentum of the positron and the photon energy $E_\gamma = E/m_e c^2$ varies in the limits $\varepsilon_+ + 1 - p_+ \leq 2\varepsilon_\gamma \leq \varepsilon_+ + 1 + p_+$.

If the steady-state spectrum of positrons is a power law, $N_+ \propto \varepsilon_+^{-\Gamma+1}$ (Γ can be the primary positron spectral index that gets harder because of ionization losses, $\Gamma \to \Gamma - 1$), then the spectrum of annihilation radiation at $E_\gamma \gg 1$ is also a power law

$$j_{ann}(E_\gamma) \propto E_\gamma^{-\Gamma}[\ln(2E_\gamma) - 1]. \tag{2.19}$$

The annihilation time of a relativistic positron is

$$
\begin{aligned}
t_{ann} &= \frac{8}{3\sigma_T^2 cn} \frac{\varepsilon_+}{\ln(e\varepsilon_+ - 1)} \\
&\simeq 4 \times 10^6 \frac{\varepsilon_+}{\ln(2\varepsilon_+) - 1}(n/1\ cm^{-3})^{-1}\ yr
\end{aligned}
\tag{2.20}
$$

2.1.5 Proton-Nucleon Interaction

Protons and nuclei going through inelastic collisions with ambient gas produce high energy γ-rays due to the production and decay od secondary pions, kaons and hyperons. If the energy of the proton is higher than $E_{th} = 2m_\pi c^2(1+m_\pi/4m_p) \approx 280\ MeV$ (threshold energy) where $m_\pi = 134.97\ MeV$ is the mass of the π^0-meson, then π^0-mesons are produced. This is the particle that will provide the γ-rays by immediately decaying to two γ-rays, $pp \to \pi_0 \to 2\gamma$.

The γ-ray spectrum coming from π_0-decay has a maximum at $E_\gamma = m_\pi c^2/2 \simeq 67.5\ MeV$, independent of the energy distribution of the π_0 mesons, and of course independently of the parent protons distribution. The characteristic cooling time of relativistic protons due to inelastic p-p interactions inside a hydrogen medium with number density n_0 is almost independent of the energy. If we use an average cross-section at very high energies and the we assume that on average the proton loses about half of its energy after each interaction, $f \approx 0.5$, the cooling time is

$$t_{pp} = (n_0\sigma_{pp}fc)^{-1} \simeq 5.3 \times 10^7(n/1\ cm^{-3})^{-1}\ yr. \tag{2.21}$$

33

Because of the way the cross section σ_{pp} depends on the energy, the cooling time is almost energy independent for energies $E > 1 \ GeV$, the initial proton spectrum remains unchanged. If we take, also, into account that the γ-ray spectrum essentially repeats the spectrum of the protons, then, it is clear that the γ-ray spectrum in high energies carries direct information about the acceleration spectrum of protons.

2.1.6   Nucleon de-excilation

As we saw in Section 2.1.5, the threshold energy for γ-ray production through π_0 decay is $\sim 280 \ MeV$. However, protons with lower energy can still produce γ-rays through another mechanism. Those protons can excite the nuclei of the ambient medium and the de-excitation of the target nuclei leads to γ-ray lines in the energy region between several hundred keV and several Mev. The spectrum of the produced γ-ray line emission depends of the abundance of elements in cosmic rays (very broad lines) and in the ambient medium, the gaseous component (broad lines) and grains (narrow lines).

This method of producing γ-rays is very inefficient, only a fraction of 10^{-5} to 10^{-6} of the kinetic energy of fast particles is transferred to γ-rays. The rest goes to the ionization and heat of the ambient gas.

2.2   Attenuation Mechanisms

2.2.1   Interaction with Matter
Photoelectric Absorption - Compton Scattering
- Electron-Positron Pair Production

There are three main attenuation mechanisms for γ-rays interacting with matter, the photoelectric absorption, the Compton scattering and the electron-positron pair production. The photoelectric absorption takes place when a photon is absorbed by an atom. The energy is transfered to one of the electrons of the atom and usually the new energy of the electron is higher than

the binding energy of the electron in the atom and the electron leaves the atom in high speed, ionizing the atom. Spectra coming from AGN can show photoelectric absorption in the soft X-rays. On the other hand, during Compton scattering, the photon scatters an electron. Part of the photon's energy is transferred to the electron and the photon appears in lower energies. In the limit that the electron is not moving, Eq. (2.5) gives the relation between the energy of the photon, before and after the scattering. The Compton scattering is important in various astrophysical sources like the interior of stars or supernovae. In the case of electron-positron pair production, the photon needs to have energy at least 2 times the rest mass energy of the electron. In order the momentum to be conserved, a nuclei should be present to absorb the photon. The same interaction can take place when instead of a nuclei we have a photon, as we will discuss later. The electron-positron pair production is important for γ-rays inserting Earth's atmosphere and interacting with nuclei and electrons. Depending on the photon energy, there is a different mechanism that dominates the attenuation. So, for energies $\lesssim 0.5\,MeV$ the Compton scattering is the dominant, for $\sim 0.5 - 5\,MeV$ the photoelectric absorption is stronger but still all three mechanisms contribute to the absorption, and photons with energy $> 5\,MeV$ lose their energy mainly through pair production.

2.2.2 Interaction with Magnetic Fields

Photons moving inside strong magnetic fields can create electron-positron pairs, $\gamma B \rightarrow Be^+e^-$. This process has been suggested as important in the magnetospheres of pulsars since there the magnetic fields are very strong.

2.2.3 Interaction with Photons - Photon-Photon Pair Production

Photons can interact other photons and produce an electron positron pair,

$$\gamma + \gamma \rightarrow e^- + e^+ \tag{2.22}$$

This interaction takes place only if a certain condition is satisfied that is based on the fact that the energy of the two photons should be at least equal with the energy of the pair when created without kinetic energy:

$$E_\gamma \varepsilon \geq \frac{2m_e^2 c^4}{1 - \cos\theta} \tag{2.23}$$

where E_γ is the energy of the high energy photon that interacts with a lower energy photon ε, θ is the angle between the directions of the photons. As seen from this equation, the most efficient collision takes place for $\theta = \pi$, for head on collisions, when the product of the two photons could have the minimum threshold $E_\gamma \varepsilon \geq m_e^2 c^4$. For any other angle, the product of the two energies has to be $> m_e^2 c^4$. The cross section of this interaction is

$$\sigma_{\gamma\gamma}(E_\gamma, \varepsilon, \theta) = \frac{3\sigma_T}{16}(1 - \beta^2)\left[2\beta(\beta^2 - 2) + (3 - \beta^4)ln\left(\frac{1+\beta}{1-\beta}\right)\right] \tag{2.24}$$

where σ_T is the Thompson cross section and β is :

$$\beta \equiv (1 - 4m_e^2 c^4/s)^{1/2}; \ \ s \equiv 2E_\gamma \varepsilon x; \ \ x \equiv (1 - \cos\theta) \tag{2.25}$$

In Fig. 2.1 the cross section is plotted. According to it the absorption is maximum for photon energies

$$\varepsilon \simeq \frac{2(m_e c^2)^2}{E_\gamma} \simeq 0.5\left(\frac{1\,TeV}{E_\gamma}\right)\,eV, \tag{2.26}$$

or, in terms of photon wavelength,

$$\lambda_{max} \simeq 1.24\,(E_\gamma[TeV])\,\,\mu m \tag{2.27}$$

An approximation for the total corss section in monoenergetic isotropic

radiation field with accuracy $\leq 3\%$ is

$$
\begin{aligned}
\sigma_{\gamma\gamma} &= \frac{3\sigma_T}{2s_0^2}\left[\left(s_0 + \frac{1}{2}\ln s_0 - \frac{1}{6} + \frac{1}{2s_0}\right)\ln\left(\sqrt{s_0} + \sqrt{s_0 - 1}\right) - \right. \\
&\left. \left(s_0 + \frac{4}{9} - \frac{1}{9s_0}\right)\sqrt{1 - \frac{1}{s_0}}\right],
\end{aligned} \quad (2.28)
$$

where $s_0 = E_\gamma\varepsilon$, the cross section depends only on the product of the two photons involved in the interaction.

This mechanism is very important for high energy astrophysics. γ-rays traveling through intergalactic radiation fields (Nikishov, 1962) or through radiation fields of compact objects (Bonometto & Rees, 1971) get attenuated. Since in this work we are going to calculate absorption effects due to this mechanism, we give at this point the optical depth of this interaction in a source of size R:

$$
\tau(\varepsilon_\gamma) = \int_0^R \int_{\varepsilon_1}^{\varepsilon_2} \sigma(E_\gamma, \varepsilon) n_{ph}(\varepsilon, r) d\varepsilon dr, \quad (2.29)
$$

where $n_{ph}(\varepsilon, r)$ is the spectral and spatial distribution of the target photon field in the source, ε_1 and ε_2 are the minimum and maximum energy of the photon field, respectively.

The energy spectrum of the electron-positron pairs created through this mechanism, for a low energy monoenergetic photon field ($\varepsilon \ll 1$) (Aharonian et al., 1983), with accuracy of $< 1\%$, is

$$
\begin{aligned}
\frac{dN(\varepsilon_e)}{d\varepsilon_e} &= \frac{3\sigma_T}{32\varepsilon^2\varepsilon_e^3}\left[\frac{4\varepsilon_\gamma^2}{(E_\gamma - \varepsilon_e)\varepsilon_e}\ln\frac{4\varepsilon(E_\gamma - \varepsilon_e)\varepsilon_e}{E_\gamma} - 8\varepsilon E_\gamma + \right. \\
&\left. \frac{2(2\varepsilon E_\gamma - 1)E_\gamma^2}{(E_\gamma - \varepsilon_e)\varepsilon_e} - (1 - \frac{1}{\varepsilon E_\gamma})\frac{\varepsilon_\gamma^4}{(\varepsilon_\gamma - \varepsilon_e)^2\varepsilon_e^2}\right]
\end{aligned} \quad (2.30)
$$

37
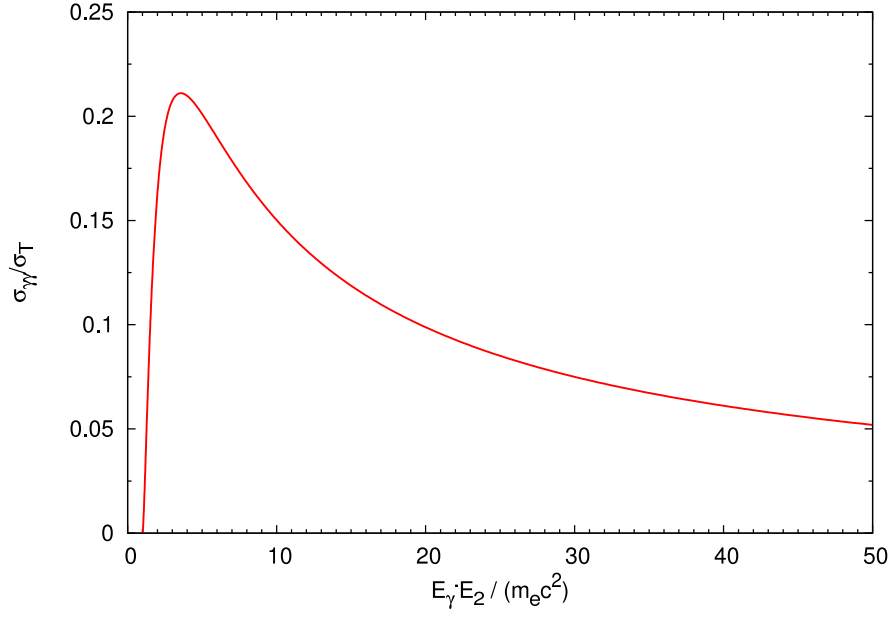
Figure 2.1 The cross section of the $\gamma\gamma$ interaction normalized over the Thomson cross section plotted over the product of the two photons energies normalized over the electron mass energy.

The kinematic range of variation of ε_e is

$$\frac{E_\gamma}{2}\left(1 - \sqrt{1 - \frac{1}{\varepsilon E\gamma}}\right) \leq \varepsilon_e \leq \frac{E_\gamma}{2}\left(1 + \sqrt{1 - \frac{1}{\varepsilon E\gamma}}\right). \qquad (2.31)$$

Chapter 3

γ-ray Telescopes

> Any sufficiently advanced technology is
> indistinguishable from magic.
> *-Sir Arthur C. Clarke*

Light is the only messenger of information from blazars and in this case, we are interested in the γ-ray emission. However, there is a big challenge we need to face trying to observe blazars at VHE. The Earth's atmosphere absorbs most electromagnetic wavebands, including γ-rays. Therefore, the only light that reaches the surface of the Earth and we can observe is optical and radio light, as illustrated in Fig. 3.1. As a consequence, we have to use methods other than optical observations to detect VHE γ-rays. One option is offered by space-based telescopes which can directly detect γ-ray photons. A second is Cherenkov telescopes on the surface of Earth, which detect the by-products of the interaction of the γ-rays with the atmosphere.

Each method has its advantages and disadvantages. Ground based telescopes are cheaper and easier to repair or upgrade than space telescopes. However, their main advantage over the satellite-based GeV instruments, is the collection area. The effective collection area of ground based telescopes
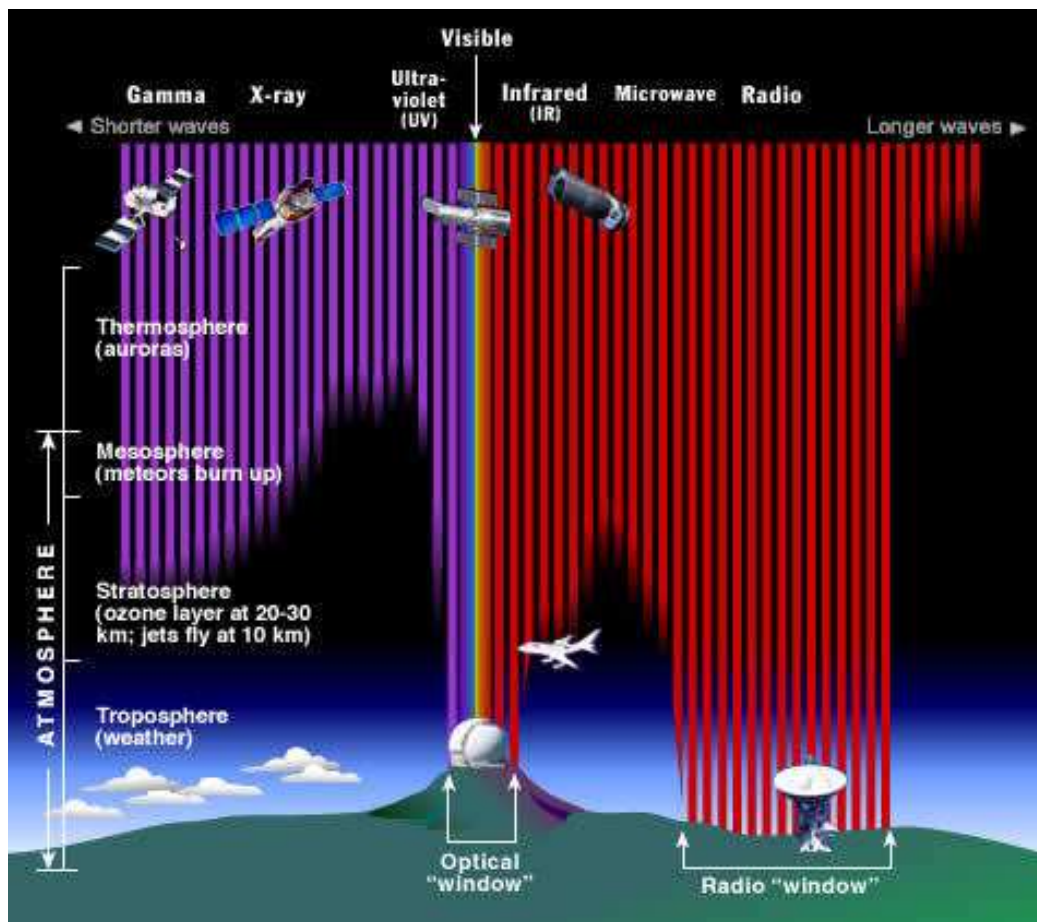
Figure 3.1 The Earth's atmosphere absorbs the electromagnetic waves of different energy in a different way. The altitude scale is logarithmic. (source: Chandra mission website and Space Telescope Science Institute)

does not depend on their size but on the light pool and is $\sim 10^5 \, m^2$, almost five orders of magnitude larger than what realistically can be achieved via direct detection in space. On the other hand, the advantage of the space-based telescopes is the precision with which the properties of the primary γ-rays can be reconstructed. Nevertheless, as we will explain later in this chapter, both space instruments and ground based telescopes are needed to cover the energy region from 1 GeV to a few TeV.

3.1 Ground Based Cherenkov Telescopes

As we saw in Fig. 3.1, the Earth's atmosphere attenuates the high energy γ-rays. However, ground based Cherenkov telescopes use the Earth's atmosphere as a part of the detector. Due to the nature of the technique, recent telescopes have a threshold of $\sim$10-100 GeV.

Once a high-energy photon enters Earth's atmosphere an air shower takes place (see Sec. 3.1.1 for more details). What reaches the ground level is faint optical photons and secondary particles (electrons, hadrons and muons). Based on this, two different types of telescopes have been developed to associate the by-products with the primary photon. One can use air-Cherenkov telescopes to detect the Cherenkov light (e.g. H.E.S.S., MAGIC) or water-Cherenkov telescopes to detect the particles (e.g. Milagro and HaWC). Since air-Cherenkov telescopes detect light, observations are possible only during the night and specifically during moonless, clear nights, since the incoming light is very faint. However, water-Cherenkov telescopes can perform observations all the time because they are not affected by weather conditions or background/foreground light. In addition, they can observe the entire sky of their hemisphere, contrary to air-Cherenkov telescopes which have a much smaller field of view. The disadvantage of water-Cherenkov telescopes is that they have a high energy threshold (a few decades of TeV) and is harder to remove the background signals. In Sec. 3.1.2 we discuss more in detail, air-Cherenkov telescopes, since the γ-ray spectra we use later in this work come

from such telescopes.

3.1.1   Air Showers

High energy ($> GeV$) photons entering Earth's atmosphere initiate electro-magnetic cascades via the processes of electron pair-production and subsequent bremsstrahlung. The initial photon produces an electron-positron pair, whose particles then interact through bremsstrahlung and Compton scattering, producing a number of energetic photons. This procedure repeats until the particles lose all of their energy. The result is a cascade of electrons and photons traveling down through the atmosphere. At these high energies, the particles move faster than the local speed of light, resulting in the emission of Cherenkov radiation. The radiation follows the air shower, is beamed around the direction of the primary photon and illuminates on the ground, an area of about 250 meters in diameter but only $\sim$ 1 meter in thickness. This is often referred to as the Cherenkov light pool.

The depth of the air-shower increases logarithmically with the energy of the primary photon, and the number of electrons at the point of maximum development of the cascade is almost proportional to the primary energy. If the energy of the photon is 1 TeV then the air-shower maximum occurs at 10 km above the sea level for a vertically incident photon. The secondary particles, electrons, muons, hadrons can be detected on the Earth's surface by detectors only if the energy of the primary photon is above $1\,TeV$, even if the detectors are placed in high altitude. However, the produced Cherenkov radiation reaches the surface only if the primary photon has energy higher than a few GeV.

Due to the small thickness of the Cherenkov light pool at the ground level, its illumination lasts only a few nanoseconds. The light spectrum peaks at wavelengths around 300-350 nm and is also quite faint. For a 1 TeV photon, only about 100 photons per m^2 arrive on the ground. Most of the Cherenkov light from the TeV showers is produced around the point of maximum development of the shower. The intensity of light at ground level scales approx-

imately as $1/d^2$, where d is the distance to the point of shower maximum, and conversely the area covered by the Cherenkov light pool is proportional to d^2. As a result the collection area increases as one moves to lower altitudes or equivalently greater zenith angles, but then the energy threshold is higher. Consequently, very high altitude observatories have been suggested as a natural way to achieve low energy thresholds (Hinton, 2009).

The light that reaches the detectors from the brightest, steady sources is still only 0.1% of the background showers rate. Those showers are initiated by cosmic rays (TeV protons and nuclei). Cosmic ray protons and nuclei interact in the atmosphere in the same way as the γ-ray photons, creating their own Cherenkov light pools. The cosmic ray induced showers come uniformly from all parts of the sky, covering the desired photonic signal. One should be able to distinguish between the photon showers and the cosmic ray showers to get reliable results. Fortunately there are some differences between these two kinds of showers. Much of the energy of the primary particle is transferred to pions produced in the first few interactions for CR air-showers. The neutral pions decay to produce electromagnetic sub-showers, with the charged pions decaying to produce muons. Single muons reaching ground level produce ringed images when impacting the telescope dish, or arcs at larger impact distances. The sub-showers often result in substructures in the images. In addition, the larger transverse angular momentum in hadronic interactions leading to showers also produce less Cherenkov light (a factor of $\sim 2 - 3$ at TeV energies), since the energy is channeled into neutrinos and into high-energy muons and hadrons in the shower core. Another difference is that a γ-ray shower gives a smaller angular distribution and tends to have an ellipsoidal shape which aligns itself with the direction of the incoming photon. On the other hand, cosmic rays produce showers with broader emission and they are less well aligned with arrival direction. Almost all of the cosmic ray showers can be removed if we measure the shape of each shower image and select only the ones that look similar to the ones that a photon can produce, (see Fig. 3.2 and 3.3).
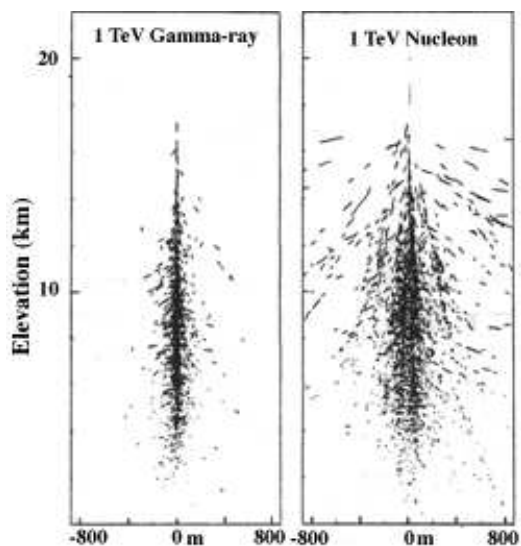
Figure 3.2 The air shower produced by a high energy photon (left) has a smaller angular distribution of a shower induced by a cosmic ray nucleon (right) with the same energy. (source: http://www.nasa.gov/home/index.html)
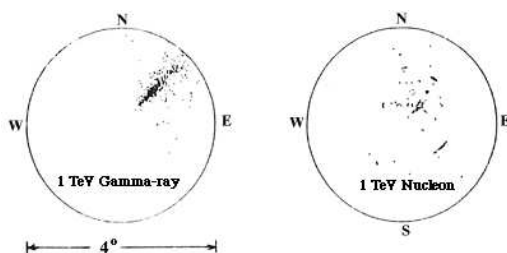
Figure 3.3 The air shower of the photon (left) has a more defined ellipsoidal shape and its emission is aligned with the arrival direction. This does not apply in the case of a nucleon induced air shower (right). (source: http://www.nasa.gov/home/index.html)

44

The primary discriminator between hadron and γ-ray initiated showers is therefore the width of the Cherenkov image. The breakthrough in the technique was the recognition by Hillas in the 1980's that the measurement and simple parameterization of images allows very effective background rejection. Several more sophisticated background rejection and shower reconstruction methods have now been developed, but the "Hillas parameter" approach remains the standard in the field.

3.1.2 Air Cherenkov Telescopes

These types of telescopes consist of one or more mirrors that concentrate the Cherenkov photons onto fast optical detectors (Fig. 3.4). Then, photomultiplier tubes placed in the focal plane of the telescope, are used to detect the Cherenkov photons.

Air Cherenkov telescopes detect Cherenkov light that reaches the ground, and since they are optical instruments, they can operate only on clear moonless nights and they observe only a small piece of the sky at a time. In this case, we want to detect the particles coming from an air shower, we should use an extensive air shower (EAS) array. An EAS array is usually composed of a sparse array of plastic scintillators. The scintillators detect the path of the charged particles traveling through them. These detectors are not ideal for γ-ray detection since the scintillator covers only $\sim 1\%$ of the total area of the array and the γ-rays outnumber electrons and positrons, so the EAS arrays have a quite high energy threshold. However, their advantage over the air Cherenkov Telescopes is that they can operate under any conditions through the whole day and they can observe the whole overhead sky continuously. The method that EAS arrays use to distinguish a photon induced air shower from a cosmic-ray induced one is using counters to detect the muons coming from air showers generated by cosmic-ray particles. However, this method is not as precise as the one used in the air Cherenkov telescopes. Table 3.1 below shows the advantages and disadvantages of each type of instrument.

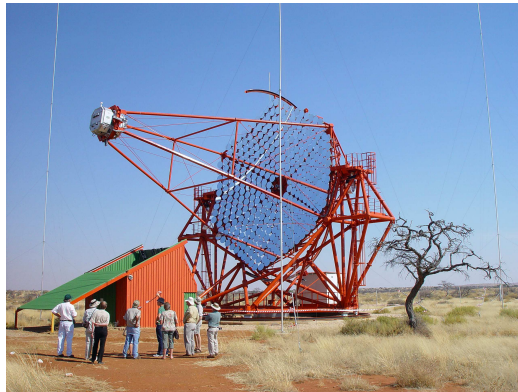A big improvement in the ACT telescopes comes from the use of multi-

Figure 3.4 One of the four identical telescopes of H.E.S.S. that detect the Cherenkov light coming from the air shower created by a high energy photon entering Earth's atmosphere. (source: http://www.mpi-hd.mpg.de/)

ple telescope observations of individual air-showers. In the case of an array with a multi-telescope trigger system, the vast majority of single muons are removed and also many hadron initiated showers. Other advantages arise at the analysis stage, primarily in the reconstruction of the shower geometry and hence in the reconstruction of the direction and energy of the primary γ-ray. Shower axis reconstruction with a single Cherenkov telescope is possible using the length of the image to estimate the angular distance to the source position. However, multiple telescopes used to view the shower from different angles allow a stereoscopic reconstruction of the shower geometry. The direction of the photon can be reconstructed with an accuracy of less than 0.1^o. The only disadvantage of the stereoscopic approach is a non negligible loss in the detection rate because the shower detection areas of the individual telescopes overlap. However, this loss of statistics is largely compensated for by a significant reduction of the energy threshold when the telescopes work in coincidence mode. In a similar way, the shower core location can be better established, leading to improved energy resolution (due to dependence of Cherenkov light intensity on impact distance). The improved shower geometry also leads to better hadron rejection, the primary rejection parameter width can be replaced by the mean scaled width, normalized based on ex-

Table 3.1 Characteristics of selected important Cherenkov telescopes. The energy threshold given is the approximate trigger-level threshold for observations close to zenith. The approximate sensitivity is expressed as the minimum flux (as a percentage of that of the Crab Nebula: $\approx 2 \times 10^{-11}$ photons cm^{-2} s^{-1} above 1 TeV) of a point-like source detectable at the 5σ significance level in a 50 hour observation (Hinton, 2009). [†] This instrument have pixels of two different sizes.

Instrument	Alt. (m)	Tels.	Tel. Area (m^2)	Total A. (m^2)	Pixels	FoV (°)	Thresh. (TeV)	Sensitivity (% Crab)
H.E.S.S.	1800	4	107	428	960	5	0.1	0.7
VERITAS	1275	4	106	424	499	3.5	0.1	1
MAGIC	2225	1	234	234	574	3.5[†]	0.06	2
CANGAROO-III	160	3	57.3	172	427	4	0.4	15
Whipple	2300	1	75	75	379	2.3	0.3	15
HEGRA	2200	5	8.5	43	271	4.3	0.5	5

pectations of γ-ray showers (for given image amplitude and impact distance) and averaged over all telescopes. The optimal separation of telescopes in an array seems to be close to the radius of the Cherenkov light-pool ($\sim$ 100 m), with closer spacing improving low-energy performance at the expense of effective collection area at higher energies (and vice versa).

3.2 Space-based γ-ray Telescopes

Space-based γ-ray telescopes give us the chance to directly detect γ-ray photons with space satellites. When we deal directly with high energy photons, we do not have light that can be refracted by a lens or focused by a mirror like optical light. Since the fluxes from the γ-ray sources are quite low and decrease rapidly with increasing energy, there is a maximum energy that a space-based detector can detect. Above this energy, the detector will be too small to detect enough photons and provide a detection. The most recent satellite, Fermi LAT, can detect (ideally) photons up to 300 GeV.

Space-based telescopes directly detect γ-ray photons. The problem of the background events because of the cosmic rays is also present as in the ground
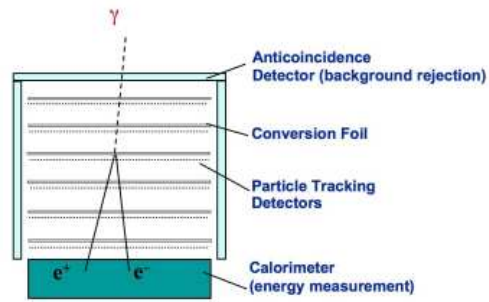
Figure 3.5 The track of a γ-ray photon and its products (e^-e^+) through a space γ-ray detector. (source: http://www-glast.stanford.edu/)

based observations. In order to eliminate false events, a plastic anticoincidence detector is used. The cosmic rays interact with the plastic detector and its signal is removed. The γ-rays pass freely through the detector and interact later with one of the thin tungsten foils in the detector. The photon produces an electron-positron pair which in turn produces ions in thin silicon strip detectors. The silicon strips alternate in X and Y direction allowing us to track the origin of the high energy photon. The particles, after their tracks are stopped by a cesium iodine calorimeter (which measures the total energy deposited), have their energy estimated (see Fig. 3.5).

Chapter 4

Extragalactic Background Light

> There is not enough darkness in all the world
> to put out the light of even one small candle.
> *-Robert Alden*

The EBL is the diffuse light between the galaxies that comes from the starlight. Its origin is extragalactic and so is expected to be isotropic on large scales. Its spectrum consists of two bumps spreading from UV to far infrared (4.1). The first one is in the optical energy range and the second one in the infrared region. The optical light consists of emitted photons from stars. Part of this light is absorbed by dust in the universe and is re-emitted in the infrared energy range, where the second bump is found. Discrete sources contribute at least partially to the EBL, that is why the background has fluctuations superimposed on the isotropic signal. Our interest in the EBL comes from the fact that this background light has the right energy to absorb the high energy γ-rays coming from distant sources, through $\gamma\gamma$ absorption, $\gamma\gamma \rightarrow e^-e^+$. Since the level of attenuation depends also on the distance of the source, the effect is stronger for the more distant sources.

Direct observations of the EBL light are very hard. Some of the challenges
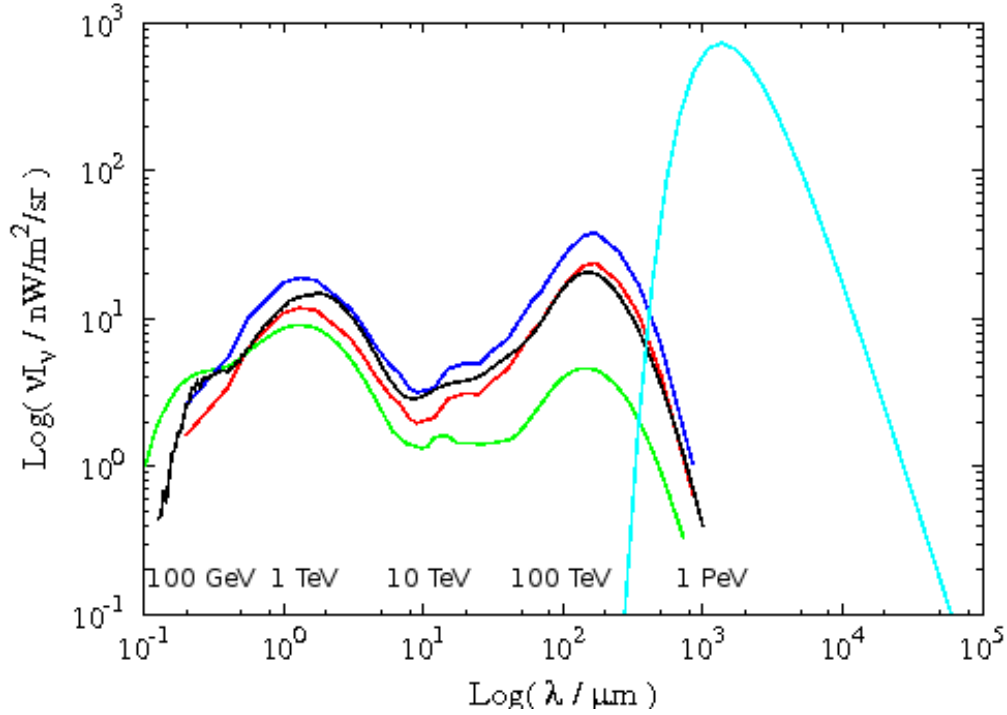
Figure 4.1 The light blue line is the Cosmic Microwave Background (CMB). The other solid lines represent different models of the EBL. The green line is the EBL from Primack et al. (2001), the black line from Kneiske et al. (2004), the red from Franceschini et al. (2008) and the blue is the Franceschini et al. (2008) model scaled by a factor of 1.6 (see the text for details). At the bottom it is shown the energy of the γ-rays that are attenuated by the specific energy of the radiation fields of the x-axis.

observers face are due to bright foreground radiation fields (e.g. zodiac light) which need to be removed. Also, the scattered or diffracted light from local bright sources like the Sun, the Moon and Earth has to be eliminated. At the same time, the EBL has to be discriminated from discrete (e.g. stars) and diffuse galactic sources (light scattered and emitted by interplanetary dust) (for a review see Hauser & Dwek (2001b)). There are only two spectral windows through which we can get reasonable observations for the EBL. They are the near infrared window near $3.5\,\mu m$, which is the minimum between scattered and emitted light from the interplanetary dust, and the submillimeter window between $\sim 100\,\mu m$, the peak of the interstellar dust emission, and the CMB. We have to add that only the lower limits of the EBL spectrum are strict and come from the galaxy and star counts theoretical calculations. In Fig. 4.2 the observational data points and limits are presented.

Due to high uncertainties on the EBL measurements, there is space for the development of different models to predict the EBL spectrum. The three different models depicted in Fig. 4.1 come from Primack et al. (2001) - green line, Kneiske et al. (2004) - black line, Franceschini et al. (2008) (referred as F1.0 from so on) - red line. In addition, with the blue line we show the Franceschini et al. (2008) model scaled by a factor of 1.6 (referred as F1.6 from so on). The last scaling comes from the Levenson & Wright (2008) where a lower limit of the EBL is derived at $3.6\,\mu m$ of $9.0^{+1.7}_{-0.9}\,nW m^{-2} sr^{-1}$, which exceeds the corresponding flux in the EBL model suggested by Franceschini et al. (2008) by a factor of ~ 1.6. For comparison we also plot the CMB with a light blue line. At the bottom of the figure it is shown the photon energy, E_γ, which maximizes the cross section of the $\gamma\gamma$ interaction for the specific EBL photon of the energy ε indicated on the x-axis. This energy is given by the formula $E_\gamma \varepsilon \approx 4(m_e c^2)^2 \approx 1\,MeV^2$ or $\lambda \approx 1.24 E_\gamma (TeV)$. The γ-rays that are mainly attenuated are in the energy range $1 - 100\,TeV$.

The spectral intensity $I_\nu(\nu_0)$ of the EBL at the observed frequency ν_0 is given by the integral over its sources (Peebles, 1993):

$$I_\nu(\nu_0) = \left(\frac{c}{4\pi}\right) \int_0^\infty \mathcal{L}_\nu(\nu, z) \left|\frac{dt}{dz}\right| dz, \tag{4.1}$$

where $\mathcal{L}_\nu(\nu, z)$ is the spectral luminosity density of all luminous objects and radiating particles in a comoving volume element at redshift z, $\nu = \nu_0(1+z)$ is the frequency in the rest frame of the luminous objects and $|dt/dz|$ is given by the equation:

$$\left|\frac{dt}{dz}\right| = \frac{1}{H_0} (1 + z)^{-1} \left[(1 + z)^2 (1 + \Omega_M z) - z (2 + z) \Omega_\Lambda\right]^{-1/2}, \tag{4.2}$$

where $\Omega_M \equiv \rho_M/\rho_c$ is the present mass density of the universe normalized to the critical density, and $\Omega_\Lambda \equiv \Lambda/3H_0^2$ is the dimensionless cosmological constant.

If there was no dust in the universe, then the spectral luminosity density, $\mathcal{L}_\nu(\nu, z)$, could be calculated knowing the spectrum of the emitting sources and how their emission evolved in time. In our case, where dust is present, the total intensity remains the same but the energy is redistributed over the entire spectrum. The difficulty in having a model of the EBL that works properly is in the estimation of the spectral luminosity density. A lot of parameters need to be known like the properties of the dust that absorbs and re-emits the light, the dust composition and grain size distribution, the dust abundance and the relative spatial distribution of energy sources and absorbing dust. Even if all of these are known or estimated, the temporal evolution should be taken into account. The cumulative spectrum of all the sources is changing with time, there are processes that destroy the dust, modify it or redistribute it relative to the radiant sources. Although the sources which mostly contribute to the EBL are the ones with redshift $z < 2$ because of cosmic expansion, luminous infrared sources at high redshifts can dominate the EBL. Non-nuclear sources do not contribute to the overall EBL but they could play a significant role at specific wavelengths. The result is that EBL models have an extra challenge to face: they need to understand

the exact contribution of the distinct energy sources to every part of the spectrum.

4.1 Categories of EBL models

There are different models that try to calculate the $\mathcal{L}_\nu(\nu, z)$ and subsequently the EBL. Depending on how they approach it, they are divided to two main categories, backward evolution (BE) and forward evolution (FE) models. Two additional categories are the semianalytical (SA) and cosmic chemical evolution (CCE) models. In what follows we give a brief overview to each of them. All of them assume that the energy is coming only from nuclear processes. The energy released from AGN (the main nonnuclear contributor) is at most $10 - 20\%$ of that released from nuclear processes.

Backward Evolution Models

BE uses the spectral properties of local galaxies to extrapolate the spectrum to higher redshifts using some parametric function for their evolution. Some of these models are referred to as no evolution (NE) models. In this simple case the models assume that the SED and the comoving number density of the galaxies do not evolve with time. As a consequence, the spectral luminosity density $\mathcal{L}_\nu(\nu, z)$ loses its dependence on the redshift and becomes $\mathcal{L}_\nu(\nu, 0)$. For a specific frequency ν_0, the spectral luminosity density is just the product of the galaxy spectral luminosity L_{ν_0} determined from observations of local galaxies, and the local galaxy luminosity function $\phi(L_{\nu_0})$:

$$\mathcal{L}_\nu(\nu, 0) = L_{\nu_0} \cdot \phi(L_{\nu_0}) \qquad (4.3)$$

Then the EBL is calculated by integrating the local luminosity density up to the redshift z_{max}, when the first galaxies are formed. It is very important to note that the spectral luminosity density is different for different wavelengths, since the origin of the light is different, i.e. at UV, optical, and near-infrared
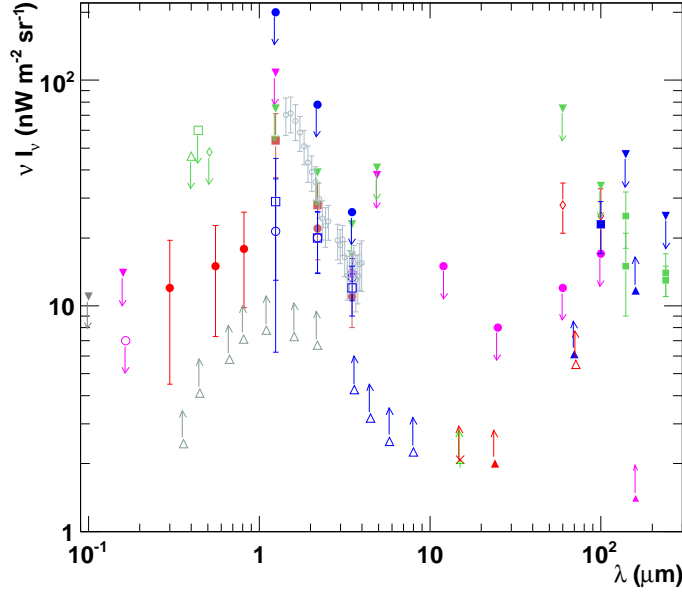
Figure 4.2 EBL measurements and limits. Image taken from Mazin & Raue (2007).
Upper limits in the UV to optical: Edelstein et al. (2000) (grey filled triangle), Martin
et al. (1991) (open pink circle), Brown et al. (2000) (filled pink triangle), Mattila (1990)
(open green triangle), Toller (1983) / Leinert et al. (1998) (open green square), Dube et al.
(1979) / Leinert et al. (1998) (open green diamond); Tentative detection in the UV/optical:
Bernstein et al. (2002, 2005) (filled red circle); Lower limits from source counts: Madau
& Pozzetti (2000) (open grey triangles), Fazio et al. (2004) (open blue triangles), Elbaz
et al. (2002) (green cross), Metcalfe et al. (2003) (2003) (red x), Papovich et al. (2004)
(filled red triangle), Dole et al. (2006) (filled pink triangles), Frayer et al. (2006) (open red
triangle); Detections in the near IR: Dwek & Arendt (1998) (open pink cross), Gorjian
et al. (2000) (filled brown circle), Wright & Reese (2000) (open blue squares), Cambrésy
et al. (2001) (filled brown squares), Matsumoto et al. (2005) (small open grey circles),
Levenson et al. (2007) (open blue circles); Upper limits from direct measurements: Hauser
et al. (1998) (filled green triangles), Dwek & Arendt (1998)) (filled pink triangles), Lagache
& Puget (2000) (filled blue triangles); Upper limits from fluctuation analysis: Kashlinsky
et al. (1996) (filled blue circles), Kashlinsky & Odenwald (2000) (filled pink circles); Lower
limits from stacking analysis in the far-IR: Dole et al. (2006) (blue triangles); Detections in
the far-IR: Hauser et al. (1998) (filled green squares), Lagache & Puget (2000) (tentative,
filled blue square), Finkbeiner et al. (2000) (tentative, open red diamonds).

the emission is primarily starlight, but in the mid-to far-infrared the emission is dominated by thermal emission from dust. Therefore, different luminosity functions need to be used for different energy bands.

Generally, comparing the number counts predicted by NE models and observations, we notice that the NE models give less counts than what we observe. This indicates the nececity to introduce the evolution in the BE models. Evolution can be introduced into BE models as pure luminosity evolution by scaling the galaxy spectra as a function of redshift, or as pure density evolution, by changing the comoving number density of galaxies with redshift. The scaling is usually done with the factor $(1 + z)^\gamma$, where γ can vary with redshift. For a summary see Lonsdale (1996).

The weak point of these models is that they do not take into consideration the physical processes that take place in the galaxies they represent, like the star and metal formation or radiative transfer processes. Their advantage is that they are simple and they offer a quick way to compare the observations with predicted galaxy number-magnitude, number-redshift, colour-magnitude and other relations.

Forward Evolution Models

Forward evolution models come to fill some of the gaps that BE models leave. The FE models use a spectral evolution code that evolves stellar populations and calculates the stellar, gas and metallicity content and SED of a galaxy as a function of time starting at the onset of star formation. These models were first introduced by Tinsley (1974) and now they are broadly used to model and date the SED of globular clusters and various galaxy types. The input parameters of these models are the star formation rate, the stellar initial mass function and the chemical evolution. The models rely on a wide range of computational and observational data sets, such as stellar evolutionary tracks, libraries of observed and calculated stellar atmospheres, stellar nucleosynthesis yields and the observed luminosity functions of galaxies. Then, models are set in a cosmological framework by specifying the values of H_0,

Ω_M and Ω_Λ. Assuming an initial formation epoch and using the above parameters, it is possible to evolve the galaxies forward into the redshift space. The parameters are adjusted so that the final result is what we observe now, in order to obtain a consistent mapping of the galaxy parameters with time. Of course, these models have to include the dust evolution and properties inside the galaxies in order to predict the EBL levels in the infrared.

The disadvantage of FE models is that they assume that all the galaxies were formed at the same time and evolve quiescently. There are no galaxies interactions, stochastic changes in the star formation rate or morphological evolution of galaxies taken into account. The problem that comes up is that these models fail to match the $850\,\mu m$ galaxy number counts, that is why they introduce a new population of ultraluminous infrared galaxies to solve it. The advantage of these models is that they manage to fit the SED of individual galaxies, galaxy number counts in select bands, and the general characteristics of the EBL as well.

In our calculations in Chapter 5 and 6 we are going to use the model presented in Franceschini et al. (2008) which is a FE model.

Semi-Analytical Models

Semi-analytical models study the development of galaxies and clusters of galaxies in a hierarchical scenario for galaxy formation (for a review and more references see Cole et al. (2000)). They need to include numerous physical processes in order to reproduce the observable galaxy properties. In addition to the stellar spectral evolution and chemical evolution models that are used in the FE models, the SA models include models for the cooling of the gas that falls into the halos, for the star formation efficiency during merger events etc. Again, the parameters are adjusted so the model matches the observational properties of the galaxies in the local universe.

The disadvantage of SA models is that, although they introduce a lot more physical processes and detailed models, there are still some discrepancies between the predictions and observations. In addition, since the models

are quite complicated it is not easy to find the source of the problem. It could be the approximations in the description of the physical processes, the uncertainties of the input data, fundamental shortcomings of the approach or a combination of these factors. Nevertheless these models still do not include dust parameters, the geometry of emitters and absorbers and their evolution. Their advantage is that they provide a physical approach to the formation and evolution of galaxies. They use two components for the overall cosmic star formation rate. The first one is a quiescent component representing the formation of stars in galactic discs. The second one is a stochastic one representing the contribution from bursts of star formation during major galaxy interaction or merging events. However, most of the SA models need to introduce a starbust component or push their parameters to the limit to explain the far infrared number counts.

Cosmic Chemical Evolution Models

The CCE models uses the idea that the EBL gives us information on the properties of the universe summed over time and over the wide variety of physical processes and systems. So, these models use the averaged properties of the universe over time in a self consistent way. The input parameters of th model are the information on the stellar activity and the initial stellar mass function in galaxies. The simplicity of the model and its global nature are the advantages. These models do not require the detailed information the SA models need. For example, the CCE models do not need explicitly the merger history of the galaxies. At the same time, since the approach is global, the CCE models do not predict galaxy counts (for a review see Fall (2001)).

4.2 EBL Absorption and Blazars

In this dissertation we are studying the spectra of blazars. Data from telescopes are analyzed to give us the blazars' spectra and then they are fitted

with models to understand the properties of the objects. However, what we observe is not necessarily the intrinsic spectrum of the source. As we show in Section 2.2.3 and in Fig. 4.1, high energy γ-rays coming from blazars are attenuated by the EBL background while they approach us.

In Fig. 4.3 the EBL density is shown for the four different models of Fig. 4.1. The green line corresponds to the Primack et al. (2001) model that is close to the low limits of the EBL spectrum. The black line corresponds to the Kneiske et al. (2004) model. The red line is the density of the Franceschini et al. (2008) and the blue line of the F1.6 case. In high energies (low wavelengths) there are not a lot of differences. But as we go to lower energies (higher wavelengths) the differences between the two extreme cases are greater, around one order of magnitude. Even if this difference may not seem so big, any difference is crucial because EBL photons with energy more than 0.1 eV are the ones that interact with the high energy γ-ray photons and the optical depth of their interaction is sensitive to the EBL energy density.

The optical depth for a high energy photon E_γ travelling through a cosmic medium filled with low energy photons with density $n_\gamma(z')$ (in our case those photons are the EBL) from a source at redshift z to an observer at the present time is :

$$\tau\left(E_\gamma, z\right) = c \int_0^z dz' \frac{dt}{dz'} \int_0^2 dx \frac{x}{2} \int_{\frac{2m_e^2 c^4}{E_\gamma \varepsilon x (1+z)}}^\infty d\varepsilon \frac{dn_\gamma\left(\varepsilon, z'\right)}{d\varepsilon} \sigma_{\gamma\gamma}(\beta) \qquad (4.4)$$

where $\sigma_{\gamma\gamma}$ is given by Eq. 2.24 and the factor s in that equation becomes :

$$s \equiv 2E_\gamma \varepsilon x (1+z). \qquad (4.5)$$

For a flat universe the differential of time in Eq. 4.4 is given by Eq. 4.2. The Hubble constant that we will use has the value $H_0 = 72\,km/s$. $\Omega_M \equiv \rho_M / \rho_c$ is the present mass density of the universe normalized to the critical density, $\Omega_M = 0.3$. $\Omega_\Lambda \equiv \Lambda / 3H_0^2$ is the dimensionless cosmological constant, $\Omega_\Lambda = 0.7$

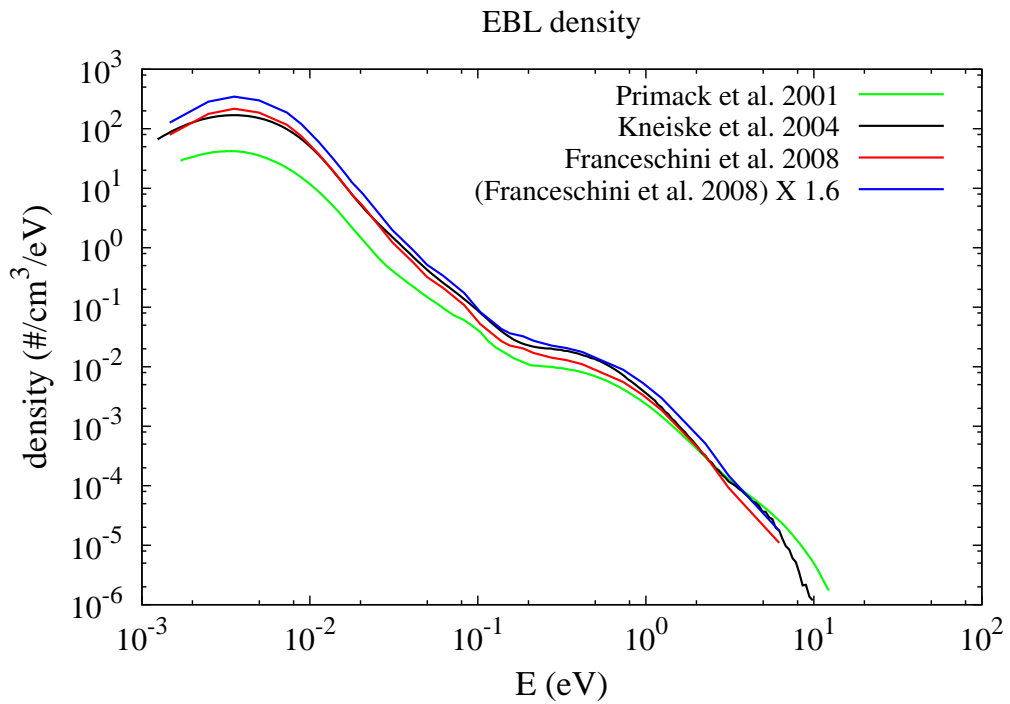Eq. (4.4) shows the dependence of the optical depth from the redshift.

EBL density

Figure 4.3 The number density of the EBL for different models. With green line is shown the Primack et al. (2001) model, with the black line the Kneiske et al. (2004), with the red line the Franceschini et al. (2008) and with the blue the F1.6 case.

That is because the EBL does not have the same energy density in all the epochs. What we can measure, with a lot of uncertainties as we saw, is the number density in the present time, $z = 0$. However what we observe is the sum of all the contribution from galaxies which are evolving through time. The local background intensity as seen from an observer with redshift z' takes into account only the sources that radiate between $z = z'$ and $z = z_{max}$, the maximum redshift of the source distribution. Sources with $z < z'$ clearly they do not contribute. The contribution to the local background intensity is given by (e.g. in Peacock (2000)):

$$I_{\nu_0}(z') = \frac{1}{4\pi}\frac{c}{H_0}\int_{z'}^{z_{max}}dz\frac{j[\nu_0(1+z),z]}{1+z}\left[(1+z)^2(1+\Omega_M z) - z(2+z)\Omega_\Lambda\right]^{-1/2}$$
(4.6)

where $j[\nu_0]$ is the galaxy comoving volume emissivity at redshift z:

$$j[\nu_0, z] = \int_{L_{min}}^{L_{max}} dlogL_{\nu_0} \cdot n_c(L_{\nu_0}, z) \cdot K(L_{\nu_0}, z) \cdot L_{\nu_0},$$
(4.7)

where $K(L, z)$ is the K-correction, $K(L, z) = (1 + z)L_{\nu_0(1+z)}/L_{\nu_0}$, and n_c is the comoving luminosity function at the redshift z expressed as the number of galaxies per Mpc^3 per unit logarithmic interval of the luminosity L at frequency ν_0. In Eq. 4.6 the j and n_c are per comoving volume. If we want to use the proper volumes we need a factor of $[1 + z]^4$.

In Fig. 4.4 the optical depth τ and the attenuation factor $e^{-\tau}$ for two different redshifts is shown, for z=0.1396 (distance of 1ES 0229+200) and z=0.4444 (distance of 3C 66A), for two EBL spectra, F1.0 and F1.6.

In Fig. 4.5 and 4.6 the observed γ-rays are shown for our two sources 1ES 0229+200 and 3C 66A, respectively, and the reconstructed spectra using the F1.0 model and the modified F1.6. In the case of 1ES 0229+200 the spectral index after the reconstruction with F1.0 becomes $dN/dE \propto E^{-0.97}$ and if the F1.6 is used, $dN/dE \propto E^{1.5}$. 3C 66A has a spectral index of 1.36 when reconstructed with F1.0 and 0.36 when F1.6 is used.
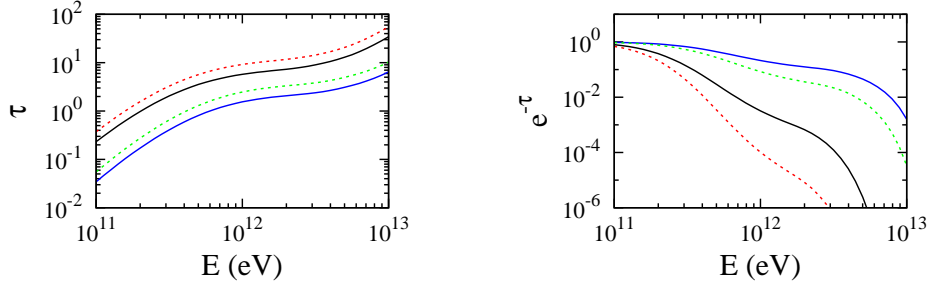
Figure 4.4 **Left panel:** The optical depth for the $\gamma\gamma$ interaction for $z = 0.1396$ (distance of 1ES 0229+200): model F1.0 solid black lines, and model F1.6 dashed red line; for $z = 0.444$ (distance of 3C 66A): model F1.0 solid blue line, and model F1.6 dashed green line (see the text for details). **Right panel**: The attenuation factor, $e^{-\tau}$, for the optical depth of the left panel.
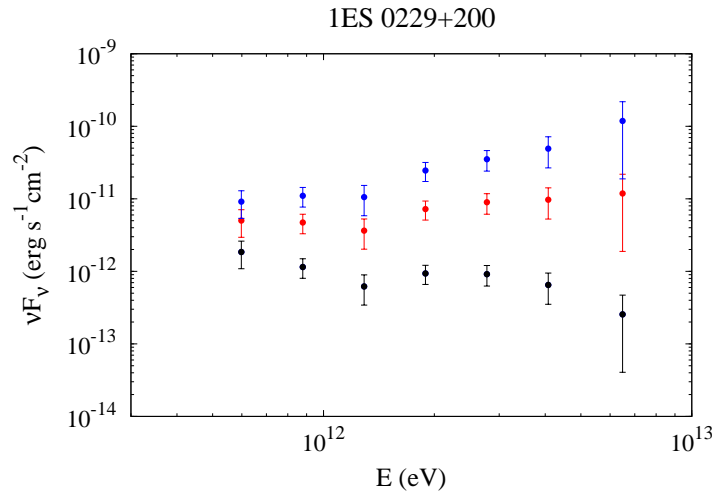
Figure 4.5 The observed spectrum of 1ES 0229+200 is presented with black points as observed by H.E.S.S. (Aharonian et al., 2007). The red points correspond to the reconstructed spectrum using the F1.0 model (spectral index of 0.97) and the blue points to the FR1.6 (spectral index of 1.5).
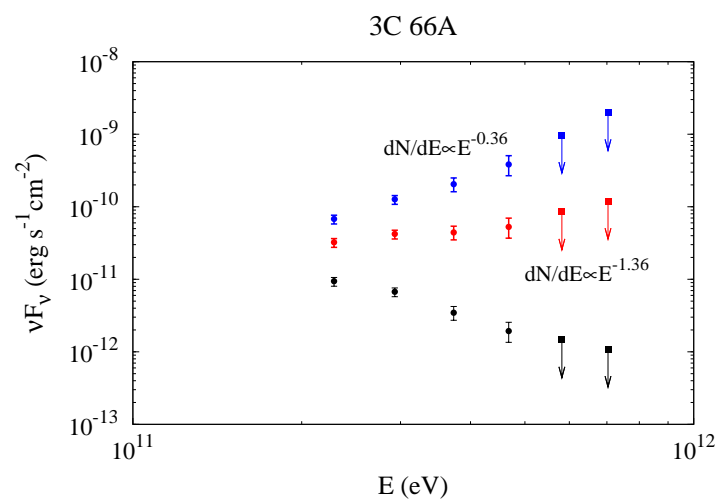
Figure 4.6 The observed spectrum of 3C 66A is presented with black points as observed with VERITAS (Acciari et al., 2009). The red points correspond to the reconstructed spectrum using the F1.0 model and the blue points to the F1.6.

Chapter 5

A Proton Synchrotron Model with Internal Absorption

> The beginnings of all things are small.
>
> *-Cicero*

The following two Chapters are based on the submitted paper Zacharopoulou O. et al. (2010). We will discuss now only briefly what is happening in this proton-synchrotron model, since in the following section it will be presented thoroughly. We assume a blob of radius R_{blob} in which protons are accelerated in high energies ($\sim 10^8$ TeV). The blob is moving with Lorentz factor Γ through a soft photon field which occupies a region of radius R. The high energy protons emit γ-rays through synchrotron radiation because of the magnetic field B in the blob. These γ-rays interact with the present soft photon field through $\gamma\gamma$ pair production and produce pair of electrons-positrons. In their turn, the secondary electron-positrons emit synchrotron radiation but in lower energies. If the production of the pairs takes place inside the blob then the synchrotron radiation emitted by them is Doppler boosted and can be observed. Otherwise, the radiation is not boosted and
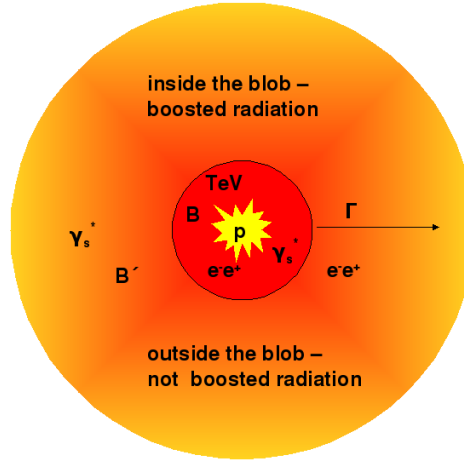
Figure 5.1 A sketch of the proton synchrotron model with internal absorption: a blob of radius R_{blob} (region filled with red colour) moves with a bulk Lorentz factor Γ through a region of typical size R filled with a soft photon field γ'_s (outer circle - orange region). Protons are accelerated in the blob and emit synchrotron radiation due to the present magnetic field B. The proton synchrotron γ-rays can be absorbed due to pair production inside the soft photon field. The pairs created in the blob can produce detectable synchrotron emission, while the emission of secondary pairs produced outside the blob will not be Doppler boosted and remain undetectable. The magnetic field outside the blob could have a different value B'.

most likely not observable. A sketch of our scenario is shown in Fig. 5.1. The three main components of the model, primary γ-ray emitter, target photon field and absorption created electron-positron pairs, are discussed in detail bellow.

5.1 Primary γ-rays

We consider an emission model in the framework of the proton synchrotron scenario. Generally, in such a scenario the energy is stored in the magnetic field, and episodically due to some event, e.g. reconnection, is transferred to protons, forming a non-thermal population of particles (see for detail Aharonian, 2000). Thus, the energy available for non-thermal protons is expressed

by:

$$E'_{tot} \simeq 2 \cdot 10^{45} \left(\frac{\kappa}{10^{-3}} \right) \left(\frac{R_{blob}}{10^{15}\,cm} \right)^3 \left(\frac{B}{100\,G} \right)^2 erg\,, \qquad (5.1)$$

where κ is the fraction of the blob magnetic energy transferred to non-thermal protons. The non-thermal proton spectrum may continue up to ultra high energies. The energy is limited only either by the confinement in the accelerator (*Hillas criterion*) or by the synchrotron losses. The Hillas criterion has geometric origin, it demands that the Larmor radius of a particle with energy E, $R_L = E/(qB)$, cannot exceed the size of the acceleration region. So, the maximum energy E_{Hillas} of an accelerated particle of electric charge q inside a magnetic field B when the size of the accelerator is R_H is $E_{Hillas} = qBR_H$. In TeV units, the maximum energy is

$$E_{Hillas} \lesssim 3 \cdot 10^7 \left(\frac{R_{blob}}{10^{15}\,cm} \right) \left(\frac{B}{100\,G} \right) TeV\,. \qquad (5.2)$$

The constrain we obtain from the synchrotron losses is

$$E_{max} \lesssim 2 \cdot 10^7 \left(\frac{B}{100\,G} \right)^{-1/2} TeV\,, \qquad (5.3)$$

and the synchrotron proper cooling time of such protons

$$t_{syn} \simeq 5 \cdot 10^4 \left(\frac{E}{10^7\,TeV} \right)^{-1} \left(\frac{B}{100\,G} \right)^{-2} s \qquad (5.4)$$

is comparable to the confinement time assuming Bohm-type diffusion

$$t_{con} \simeq \frac{3 \cdot 10^5}{\kappa_D} \left(\frac{E}{10^7\,TeV} \right)^{-1} \left(\frac{B}{100\,G} \right) \left(\frac{R_{blob}}{10^{15}\,cm} \right)^2 s\,, \qquad (5.5)$$

where κ_D is the ratio of the proton diffusion coefficient to the Bohm one. We note that the confinement time t_{con} cannot be shorter than the light crossing time

$$t_{IC} \simeq 3 \cdot 10^4 \left(\frac{R_{blob}}{10^{15}\,cm} \right) s\,. \qquad (5.6)$$

Given the identical dependence on the particle energy in Eqs.(5.4-5.5), the cooling regime is defined by the following parameter:

$$\xi = \frac{t_{con}}{t_{syn}} = \frac{6}{\kappa_D} \left(\frac{B}{100\,G} \right)^3 \left(\frac{R_{blob}}{10^{15}\,cm} \right)^2 , \qquad (5.7)$$

implying *fast cooling* for $\xi > 1$ and *slow cooling* for $\xi < 1$. In the case of slow cooling only a fraction ξ of the proton non-thermal energy will be emitted through the synchrotron channel. In the blob frame the synchrotron emission is expected to be isotropic with SED extending up to the energy

$$E_{maxH} \simeq 0.2\xi\ TeV \qquad (5.8)$$

if the proton maximum energy is determined by the Hillas criterion Eq.(5.2), i.e. $\xi < 3$; or

$$E_{maxS} \simeq 0.4\ TeV \qquad (5.9)$$

if the high energy cutoff is due to synchrotron losses.

In the laboratory reference frame the proton emission of such a blob is characterized by a luminosity of

$$L_\gamma \simeq 3 \cdot 10^{46} \left(\frac{\kappa}{10^{-3}} \right) \left(\frac{R_{blob}}{10^{15}\,cm} \right)^3 \left(\frac{B}{100\,G} \right)^4 \left(\frac{E}{10^7\,TeV} \right) \left(\frac{\delta}{30} \right)^4 erg/s , \qquad (5.10)$$

where δ is Doppler boosting factor, with a typical variability time-scale of

$$t_{var} \simeq 2 \cdot 10^3 min(1,\xi) \left(\frac{\delta}{30} \right)^{-1} \left(\frac{E}{10^7\,TeV} \right)^{-1} \left(\frac{B}{100\,G} \right)^{-2} s \qquad (5.11)$$

Formally, the VHE spectrum of the boosted proton synchrotron may extend up to

$$E_{max} \simeq 10 \min(1,\xi/3) \left(\frac{\delta}{30} \right) TeV . \qquad (5.12)$$

However, we note that the actual shape of the spectra close to the cutoff may be rather smooth with a remarkable fraction of particles above the for-

mal cutoff energy (e.g. for non-relativistic diffusive shock acceleration see Zirakashvili & Aharonian, 2007). This effect may significantly relax the constraints imposed by Eq.(5.12), given quadratic dependence of the synchrotron photon energy on the energy of the parent particles.

For the model calculations, we have assumed the spectrum of the nonthermal protons to be a power law with exponential cutoff, which was defined according to Eq.(5.3), i.e. we assume very high acceleration efficiency. We have considered two cases of the power-law index: (i) the value 2.2 close to the conventional value 2; and (ii) a very hard case with power-law index of -0.5, as predicted by the converter mechanism (Derishev et al., 2003). The emission was assumed to be produced in the *slow cooling* regime. This approximation is valid for time intervals shorter than variability time scale defined by Eq.(5.11). Under this assumption, the VHE emission component is characterized by a photon index 1.6 in the (i) case and by the synchrotron hardest possible value of 2/3 in the case of the converter mechanism. We note that the latter case involves VHE spectra harder than the conventionally accepted, but this value is achievable only for flaring episodes. In the case of steady VHE emission, the dominant cooling mechanism should modify the proton spectrum. Thus, in the steady case the VHE photon index should be close to 1.5 or 1 in the cases of dominant synchrotron or *adiabatic* losses, respectively.

5.2 Internal absorption

There are many possible sources of UV – soft X-ray emission close to the base of the jet in AGN: accretion disc, corona, etc. This emission may be reprocessed by matter surrounding the jet. This leads to the formation of BLRs, which are characterized, in a case of powerful blazars, by a size of 10^{18} cm with luminosities of 10^{45} erg/s (for theoretical modeling of BLR spectrum see e.g. Tavecchio & Ghisellini, 2008). Such dense photon fields imply significant $\gamma\gamma$ absorption, at least if the production area is located

close to the jet base. In the scenario of the internal absorption (Aharonian et al., 2008) the intrinsic γ-ray spectrum is to be significantly absorbed at energy ≤ 0.1 TeV to harden the VHE band. The $\gamma\gamma$ optical depth for a γ ray photon interacting with a soft photon with energy that maximizes the cross section, can be estimated approximately by:

$$\tau(E_\gamma) \simeq 0.2\sigma_T R n_{ph} \left(3.5m^2c^4/E_\gamma\right) , \qquad (5.13)$$

where σ_T is the Thomson cross-section, R is the radius of the sphere with the soft photon field through which the γ-ray travels, and n_{ph} is the density of the target photons. In our model we prescribe the maximum optical depth for a given size R. Therefore, the density of the photons can be calculated by Eq. (5.13) and we can estimate the luminosity of the photon field:

$$L_{ph} \simeq 4\pi R^2 \frac{\varepsilon_{ph} n_{ph} c}{4} \simeq 5 \cdot 10^{42} \left(\frac{E_\gamma}{100\,GeV}\right)^{-1} \left(\frac{\tau}{5}\right) \left(\frac{R}{10^{17}\,cm}\right) \frac{erg}{s} , \quad (5.14)$$

where τ is the maximum opacity which occurs for the γ-ray energy E_γ. In general, the photon field required for the internal absorption scenario has quite low luminosity, and may be undetectable. In order to obtain a hard spectra after the internal absorption and have a non-homogenous absorption in the γ-rays, we assume the target photon field to be a grey body, i.e. diluted Planckian distribution, characterized by temperature T and dilution coefficient η.

5.3 Secondary emission

The energy of the absorbed γ-rays is transferred to an electron-positron pair, through the process $\gamma\gamma \rightarrow e^- e^+$, discussed in detail in Sec. 2.2.3. Since the internal absorption scenario requires a large optical depth $\tau \geq 1$, a significant fraction of energy Eq.(5.1) is shared with non-thermal electrons. These pairs can produce synchrotron radiation in lower energies than the protons but their observational appearance depends strongly on their creation region.

Namely, if the pair is created outside the blob, the emission is not boosted, and remains most likely undetectable. On the other hand, if the electrons are created in the blob, they are fast isotropized and emit synchrotron radiation due to the strong magnetic field in the blob. This radiation component may be detected and below we focus on its properties.

In the blob reference frame the target photon field is strongly anisotropic. Thus, the optical depth in the blob depends on the direction of the γ-ray with respect to bulk velocity. Since we assume the blob to be homogeneous, we introduce the optical depth τ_{in} averaged over the γ-ray directions (in the blob rest frame) that characterizes the absorption in the blob. We have to note at this point that in our model two different optical depths are introduced. The first one is the optical depth τ in Eq 5.13 that describes the interaction of γ-rays while they travel out of the region of the soft photon field. The second optical depth involved is the τ_{in} which is the optical depth only for the region of the blob. Of course, $\tau_{in} \leq \tau$ and the absorption inside the blob is the one that will give us the observable secondary synchrotron radiation. The optical depth of the whole region, τ, is important for the formation of the hard spectrum in the γ-rays.

It is possible to estimate the optical depth τ_{in} in the blob since basically all the emission is focused towards the direction of the proper motion. Indeed, the optical depth for a γ-ray propagating in the direction of the proper motion will be

$$\tau_{in}(E_\gamma) \simeq 0.2\sigma_T R_{blob}\Gamma n_{ph} \left(3.5m^2c^4/E_\gamma\right) , \qquad (5.15)$$

where Γ is blob bulk Lorentz factor (for detail see e.g. Begelman et al., 2008). But actually in our computation the blob size is characterized by the internal optical depth and the relation (5.15) was used to derive the size of the blob. Thus, a simple relation between the size of the BLR region, the size of the blob, the maximum optical depth τ, the blob optical depth τ_{in} and the bulk Lorentz factor is:

$$\frac{\tau_{in}}{\tau} \simeq \frac{\Gamma R_{blob}}{R} . \qquad (5.16)$$

This ratio indicates that in the case of a compact region filled with the photon field, $R \sim 10^{17}$ cm, the optical depth in the blob is quite high:

$$\tau_{in} \simeq 1 \left(\frac{\tau}{5}\right) \left(\frac{R_{blob}}{10^{15}\,cm}\right) \left(\frac{\Gamma}{20}\right) \left(\frac{R}{10^{17}\,cm}\right)^{-1}. \tag{5.17}$$

The injection spectrum of secondary electrons depends on the photon index of the primary γ-rays, the target photon field, the bulk Lorentz factor of the blob and the internal optical depth. If the target photon field is characterized by a peak energy ε (which should be close to 10 eV), then the maximum injection rate in the blob should occur close to

$$E_e \simeq 5 \left(\frac{\varepsilon}{10\,eV}\right)^{-1} \left(\frac{\Gamma}{20}\right)^{-1} GeV. \tag{5.18}$$

However, we have to note that depending on the primary γ-ray spectrum slope, this value can change significantly. Since the synchrotron cooling time of these electrons,

$$t_{syn} \simeq 40 \left(\frac{E_e}{1\,GeV}\right)^{-1} \left(\frac{B}{100\,G}\right)^{-2} s, \tag{5.19}$$

is very short compared to both the typical time scales for the system and the electron inverse Compton cooling time,

$$t_{ic} \simeq 7 \cdot 10^3 \left(\frac{E_e}{1\,GeV}\right)^{-1} \left(\frac{\Gamma}{20}\right)^{-1} \left(\frac{R_{blob}}{10^{15}\,cm}\right) \left(\frac{\varepsilon}{10\,eV}\right)^{-1} \left(\frac{\tau_{in}}{1}\right)^{-1} s, \tag{5.20}$$

all the absorbed energy will be immediately released through the synchrotron channel.

The secondary synchrotron emission should appear at energies close to

$$\varepsilon_{sec} \simeq 1.5 \left(\frac{\Gamma}{20}\right)^{-2} \left(\frac{\delta}{30}\right) \left(\frac{\varepsilon}{10\,eV}\right)^{-2} \left(\frac{B}{100\,G}\right) keV. \tag{5.21}$$

However, we must note that in the case of large internal absorption or high

bulk Lorentz factor, the secondary synchrotron component has a rather broad distribution. The variability time-scale of the synchrotron emission of secondary pairs is determined by the change of the injection, i.e. by the change of primary γ-ray component, and it is possible to radiate effectively through this channel approximately (in the case of small internal opacity and assuming the non-thermal proton to be distributed over the energy interval between $1\,GeV$ and $10^7\,TeV$ with spectrum slope to be close to 2)

$$L_{sec} \simeq 10^{44} \left(\frac{\tau_{in}}{0.25}\right) \left(\frac{\kappa}{10^{-3}}\right) \left(\frac{R_{blob}}{10^{15}\,cm}\right)^3 \left(\frac{B}{100\,G}\right)^4 \left(\frac{\delta}{30}\right)^4 \, erg/s\,. \quad (5.22)$$

Another important connection appears between the slopes of the intrinsic γ-ray spectrum and the highest energy part of the secondary synchrotron components. Namely, it is possible to derive an analytical representation of the high energy part of the secondary e^-e^+ spectrum. This part of the spectrum is produced by electron-positron pairs which are created significantly above the threshold of the $\gamma\gamma$ interaction, thus it is possible to use the asymptotic limit of the cross section. Moreover, in such an interaction regime one of the created leptons gets almost all the parent γ-ray energy. Thus, the cross section can be approximated as the following

$$\frac{d\sigma}{dE_e} \propto \frac{\delta\left(E_e - E_\gamma\right)}{E_\gamma}. \quad (5.23)$$

Then, the spectrum of the secondary pair injection directly connected to the intrinsic spectrum of VHE γ-rays is:

$$\frac{dN_e}{dE_e dt} \propto c \int dE_\gamma \frac{d\sigma}{dE_e} \frac{dN_\gamma}{dE_\gamma} = \frac{c}{E_e} \frac{dN_\gamma}{dE_e}. \quad (5.24)$$

In particular, if the intrinsic γ-ray spectrum is a power law in this energy band, with a photon index s, then, since the dominant cooling mechanism is synchrotron radiation, the energy distribution of the secondary leptons is a power law with an index $s + 2$ and the high energy part of the synchrotron spectrum is described by a power law of photon index $(s + 3)/2$. We note

that even for a very hard intrinsic spectrum of $s \sim 1.5$, the synchrotron emission of secondary pairs will be characterized by a photon index ~ 2.25. Such behaviour is expected at the energies

$$\varepsilon_{limit} \geq 200 \left(\frac{\Gamma}{20}\right)^{-2} \left(\frac{\delta}{30}\right) \left(\frac{\varepsilon}{10\,eV}\right)^{-2} \left(\frac{B}{100\,G}\right) keV \,. \tag{5.25}$$

For the model calculation, we assumed the blob to be homogeneous. The pair production kernel, i.e. the energy distribution of secondary electrons produced by a γ-ray of a certain energy, was calculated using anisotropic differential pair production cross section obtained by Boettcher & Schlickeiser (1997) convolved with boosted Planckian distribution and averaged over the initial γ-ray direction. The injection rate of electrons was calculated by convolving the pair production kernel with proton synchrotron spectrum multiplied by the factor $(1 - \exp(-\tau_{in}))$ connected to the absorption in the blob. The energy distribution of electrons was calculated using the approximation of continuous losses accounting for dominant synchrotron losses only. The secondary synchrotron emission was calculated using the obtained distribution of electrons. The variability properties of this radiation component are related to the variability of the intrinsic γ-rays and to a possible change of the absorption rate. Any detailed discussion of this issue is beyond the scope of this study.

Chapter 6

Fitting of the Sources

> We are bits of stellar matter that got cold by accident,
> bits of a star gone wrong.
> *-Sir Arthur S. Eddington*

To study the implication of the internal absorption scenario, we focus on two distant blazars 1ES 0229+200 and 3C 66A, located at redshifts $z = 0.1396$ and $z = 0.444$, respectively. These AGN have very different properties as seen in γ-rays, both in the TeV and GeV energy bands. In particular, the blazar 1ES 0229+200 displays an apparently persistent γ-ray emission, without significant flux or spectral changes between two HESS measurements separated by one year (Aharonian et al., 2007). Moreover, the Fermi LAT was not able to detect GeV emission from the direction of 1ES 0229+200, providing upper limits below the TeV intrinsic flux level (as expected for the least intensive EBL).

The blazar 3C 66A displays a variable VHE signal, as seen with VERITAS (Acciari et al., 2009), with a 6% Crab flux flaring episode. Fermi LAT detected a significant GeV γ-ray excess from the source. Moreover, an increase of the GeV flux simultaneous with the VHE flare was observed (Reyes

et al., 2009). Importantly, as we will discuss, the GeV flux level exceeds significantly the de-absorbed VHE flux, unless the VHE component gets very hard. Thus, a smooth connection of these radiation components seems difficult to achieve, for the assumed redshift z=0.444.

To study the impact of the intergalactic absorption, the VHE spectra were de-absorbed using the EBL model calculated by Franceschini et al. (2008), with two different intensities: (i) as in the original paper (F1.0); and (ii) scaled up by a factor of 1.6 (F1.6). The latter case was considered in order to satisfy the lower limits obtained by Levenson & Wright (2008). In Fig. 4.4 the VHE γ-ray optical depths together with the attenuation factors for the blazars are shown for the two EBL intensities: F1.0 and F1.6. The calculated attenuation was used to reconstruct the initial spectra obtained with H.E.S.S. from 1ES 0229+200 (Aharonian et al., 2007) and with VERITAS for 3C 66A (Acciari et al., 2009). The obtained spectrum for 1ES 0229+200 is shown in Fig. 6.1 and for 3C 66A in Fig. 6.2. In both figures the black points correspond to the observed spectra, the red points to the spectra reconstructed with F1.0 EBL model, and the blue points to the spectra reconstructed with F1.6 EBL intensity. As it can be seen from the figures the reconstructed spectra are significantly harder compared to the observed ones. In particular, in the case of a high EBL intensity, the spectra have photon indices $\Gamma \sim 1$ and 0.4 for 1ES 0229+200 and 3C 66A, respectively; i.e. they are remarkably harder than the conventional spectrum of photon index 1.5.

To study the case of 1ES 0229+200, we have combined the reconstructed VHE spectra with available X-ray and optical data from SWIFT (Tavecchio et al., 2009) and BeppoSAX (Costamante et al., 2002), together with Fermi LAT observations (Reyes et al., 2009). The observation data are summarized in Fig. 6.3. We have applied the internal absorption scenario as described in Sec. 5 to reproduce the VHE spectrum (for both levels of intergalactic absorption) together with the X-ray spectrum. We considered two cases for the proton energy distribution: "standard" power-law with an index 2 and very hard. In the case of a proton distribution with power-law
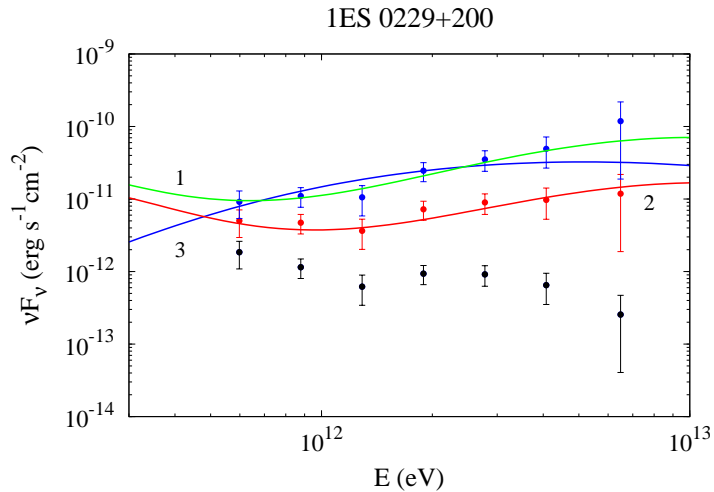
Figure 6.1 The H.E.S.S. observations of the source 1ES 0229+200 (Aharonian et al., 2007, black points), the de-absorbed spectrum using F1.0 EBL model (red points) resulting to $dN/dE \propto E^{-1.50}$; and using the F1.6 EBL (blue points) resulting to $dN/dE \propto E^{-0.97}$. Each line 1, 2 and 3 corresponds to a different set of parameters of the model that fits the data (see Table 6.1).

index 2 the proton synchrotron radiation below the peak has photon index close to 1.5, i.e. formally can explain the VHE data points without invoking internal absorption. Thus, in this case the key question is whether the internal absorption scenario can provide a consistent explanation of the X-ray component. Given the strict upper limits provided by Fermi-LAT, the available energy budget for the secondary pairs is quite limited, unless the target photons have a broad energy distribution extending to X-rays and thus providing significant attenuation also in the Fermi energy band, or the proton energy distribution has a very high lower-energy-cutoff. Without these two conditions, the X-ray synchrotron flux of secondary pairs would be approximately an order of magnitude below the reported X-ray fluxes. Thus, in this specific case, the internal absorption scenario requires additional ad-hoc assumptions, in particular very high lower-energy cutoff in the proton distribution, to provide a self-consistent interpretation of the TeV and X-ray data.

In the case of the higher EBL flux, i.e. the model F1.6, the reconstructed

Table 6.1 The table contains the values of the parameters used in the model fits of Fig. 6.1, 6.3 and 6.4. B, Γ are the obvious parameters, T is the temperature of the soft photon field, τ is the optical depth for distance R where the soft photons are, τ_{in} is the optical depth inside the blob, R_{blob} is the radius of the blob, δ is the Doppler factor, L_{ph} the soft photons luminosity and L_{γ} the intrinsic luminosity of the γ-rays before any absorption. A dimensionless value $\eta_0 > 1$ is a scaling parameter related to a change of photon field density. This parameter has no impact on the model radiation output.

Parameter	1ES 0229+200		
	Fit 1	Fit 2	Fit 3
$B'\,(\mathrm{G})$	80	40	100
$T\,(\mathrm{K})$	7×10^3	5×10^3	10^5
τ	3	3	5
τ_{in}	0.9	0.8	1.2
$R'_{blob}\,(\mathrm{cm})/\eta_0$	10^{15}	5×10^{15}	5×10^{15}
$R\,(\mathrm{cm})/\eta_0$	3×10^{16}	6×10^{17}	2.1×10^{17}
Γ	10	30	10
δ	11	8	8
$L_{ph}\,(\mathrm{erg/s})/\eta_0$	2.3×10^{41}	2.8×10^{42}	3×10^{43}
$L_{\gamma}\,(\mathrm{erg/s})$	5×10^{40}	1.6×10^{41}	2.9×10^{41}

VHE spectrum would have a photon index close to 1, i.e. harder than any unabsorbed proton synchrotron spectrum. In Fig. 6.4 the spectrum of 1ES 0229+200 is shown before and after the internal absorption for the fits of the multiwavelength spectrum. As shown, internal absorption allows to harden the TeV spectrum to the required level, but in case of a conventional proton distribution, the discrepancy with the Fermi-LAT upper limits is very strong. The correction of this conflict requires to further suppress the GeV emission by introducing other ad-hoc assumptions like again an additional absorption or lower energy cutoff. However, we believe that these assumptions cannot be endorsed without an additional observational or theoretical justification.

On the other hand, assuming a hard proton distribution (Derishev et al., 2003), there is no collision with the Fermi LAT upper limits, and the internal
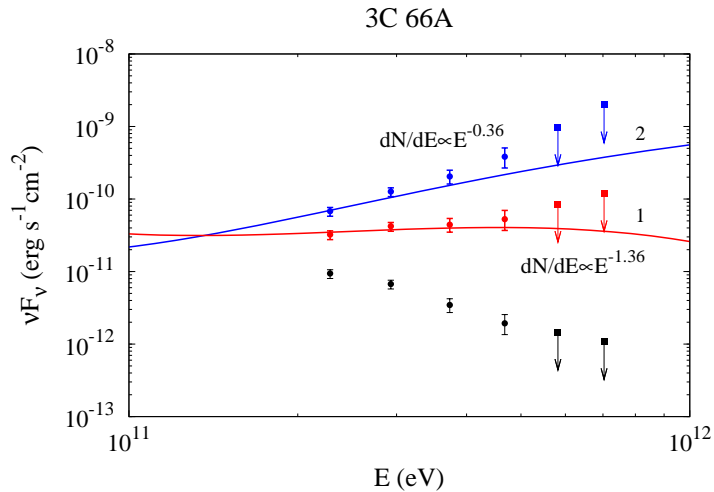
Figure 6.2 The observational data of 3C 66A from VERITAS (Acciari et al., 2009, black points), the de-absorbed spectrum using the EBL model F1.0 (red points) resulting to $dN/dE \propto E^{-0.36}$, and using the EBL spectrum F1.6 (blue points) resulting to $dN/dE \propto E^{1.36}$. The two lines, labeled 1 and 2, are two different runs of our model to fit the data (see Table 6.2).

absorption allows to harden the VHE spectrum to the required slope independently on the EBL flux level. In particular, the parameter sets 1 and 2 (columns 2 and 3 in the Table 6.2) correspond to the case of the high EBL level (photon index ~ 1), and the model curve labeled 2 has VHE slope of value ~ 1.5, as required by the EBL level obtained by Franceschini et al. (2008). In the calculations we have adopted a grey body distribution for the target photons (see Table 6.1 and 6.2 for detail).

The synchrotron radiation of secondary electron-positron pair, calculated self-consistently with the hard VHE component, can explain the X-ray data obtained from 1ES 0229+200, with the caveat that the X-ray data are not simultaneous with TeV observations. A characteristic feature of the secondary pairs origin of the X-ray emission is a quite broad radiation component. This prediction can be tested above 10 keV with hard X-ray instruments like Suzaku, or with the future missions NuStar or Astro-H.

For the case of the blazar 3C 66A, we have combined the reconstructed VHE VERITAS spectrum with the spectrum detected by Fermi-LAT during

Table 6.2 The table contains the values of the parameters used in the model fits of Fig. 6.2, 6.5 and 6.6. B, Γ are the obvious parameters, T is the temperature of the soft photon field, τ is the optical depth for distance R where the soft photons are, τ_{in} is the optical depth inside the blob, R_{blob} is the radius of the blob, δ is the Doppler factor, L_{ph} the soft photons luminosity and L_γ the intrinsic luminosity of the γ-rays before any absorption. A dimensionless value $\eta_0 > 1$ is a scaling parameter related to a change of photon field density. This parameter has no impact to the model radiation output.

| | **3C 66A** | | |
Parameter	Fit 1a	Fit 1b	Fit 2
$B'\,(\mathrm{G})$	100	100	1.2
$T\,(\mathrm{K})$	8×10^4	8×10^4	5×10^4
τ	2	2	1.6
τ_{in}	0.6	6×10^{-3}	0.26
$R'_{blob}\,(\mathrm{cm})/\eta_0$	5×10^{17}	5×10^{15}	10^{18}
$R\,(\mathrm{cm})/\eta_0$	7×10^{19}	7×10^{19}	6×10^{19}
Γ	40	40	10
δ	15	15	4
$L_{ph}\,(\mathrm{erg/s})/\eta_0$	4×10^{45}	4×10^{45}	2×10^{45}
$L_\gamma\,(\mathrm{erg/s})$	7×10^{42}	7×10^{42}	4×10^{44}

the VHE flare, and with available X-ray/optical data from MDM and Swift (Reyes et al., 2009). The observational data are summarized in Fig. 6.5. We have applied the internal absorption scenario as described in the Sec. 5 to fit the VHE spectrum (for both levels of intergalactic absorption). For the de-absorption of the VHE spectrum we have used the standard value of the source redshift, i.e. $z = 0.444$. This physical parameter is not firmly measured for the source, and there are some indications that the source is located significantly closer. In particular, Prandini et al. (2010) suggested that the source redshift value should not exceed 0.34. This conclusion, however, was derived by using an empirical postulate that the initial VHE γ-ray spectrum cannot be harder than the high energy (HE) spectrum measured with Fermi LAT. This approach is based on the assumption that GeV and TeV spectra are closely connected being two parts of a relatively smooth
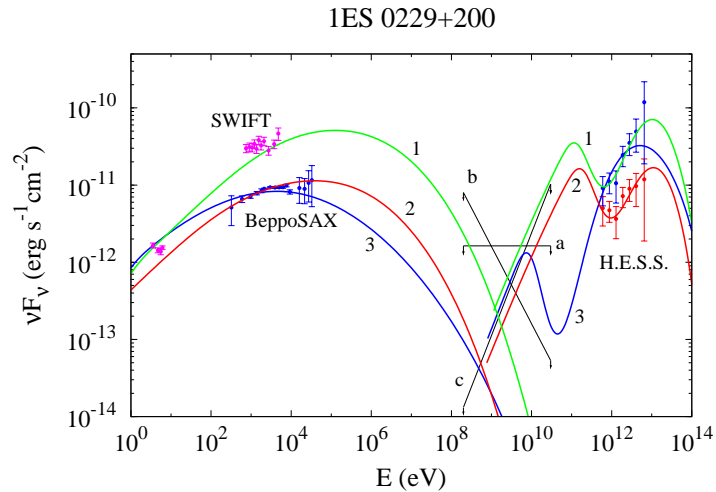
Figure 6.3 The red and blue points in γ-rays and the lines 1, 2 and 3 are the ones described in Fig. 6.1. Additionally the SWIFT data are plotted (magenta points) and the BeppoSAX (blue points in X-rays). The solid black lines between $30\,MeV$ and $30\,GeV$ are the upper limits based on FERMI LAT observations (Abdo et al., 2009), for $\Gamma = 2$ (a), $\Gamma = 1.5$ (b) and $\Gamma = 3$ (c).

spectrum. On the other hand, if the redshift is indeed $\gtrsim 0.4$, the TeV and GeV parts look quite different. This does not imply however that they are of different origin. Our model, nevertheless, can explain both components by a single proton population as parts of the smooth proton synchrotron spectrum, but later severely deformed by the energy-dependent internal absorption. A good agreement can be achieved assuming a proton energy distribution with power-law index of 2.2. The required hard VHE photon indices of value 1.4 and 0.4 (for the EBL models F1.0 and F1.6 respectively) can be naturally combined with high Fermi LAT fluxes. In Fig. 6.5 the spectrum of the source before and after the internal absorption for the model fits is presented and in Fig. 6.6 a zoom-in the high energies is shown. In the Table 6.2, the parameters used for the modeling of the multiwavelength properties of this source are shown. A weak internal absorption (with maximum optical depth near 1.6) allows the hardening of the VHE spectrum to the required photon index 1.4 in the case of the EBL model F1.0 (see the line marked with 2 in Fig. 6.2). A rather small change of the target photon field properties, e.g. an increase
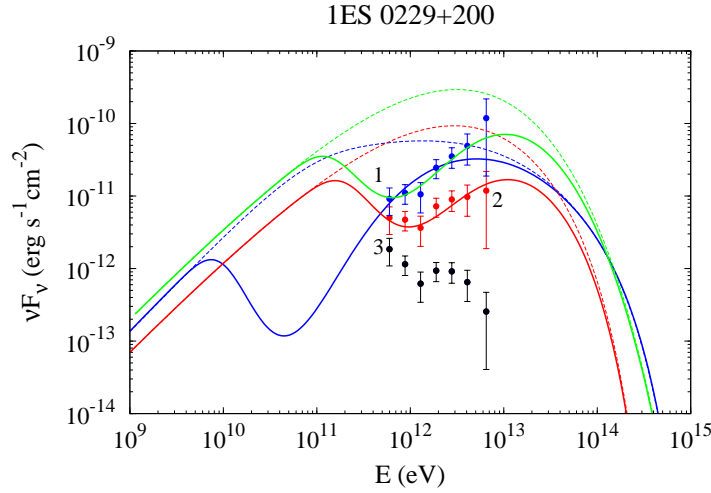
Figure 6.4 The H.E.S.S. observations of the source 1ES 0229+200 (Aharonian et al., 2007, black points), the de-absorbed spectrum using F1.0 EBL model (red points) and using the F1.6 EBL (blue points). The solid lines in green (1), red (2), blue (3) correspond to a different set of parameters for the fit of the source (see Table 6.1). The dashed lines correspond to the same set of parameters as the solid lines but they represent the spectrum of the source before the internal absorption from the planckian-type radiation field.

of the maximum optical depth from 1.6 to 2 together with higher photon field temperature, leads to the formation of a VHE spectrum with photon index 0.4, as required in the case of the higher intensity of EBL (the model F1.6).

In general, the flux level expected from secondary pair synchrotron radiation may be comparable to the detected one, although different model parameters can affect this emission component significantly. This is demonstrated in Fig. 6.5 with model curves marked 1a and 1b. The only difference between these cases is the size of the relativistically moving blob. In the case of a small production region, the majority of the secondary pairs are created outside the blob, thus their radiation mostly will not contribute to the system emission. We have to note that, although the secondary emission can be at the level of the observational points, the observed optical and X-ray spectra cannot be explained by the secondary emission only. The reason for that is
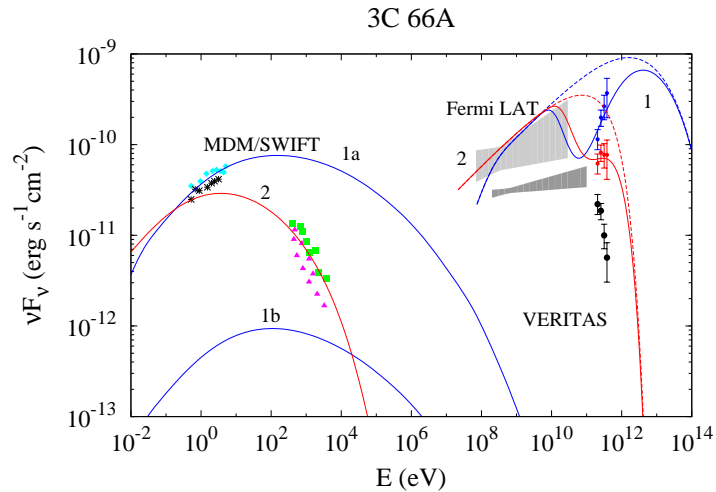
Figure 6.5 The observational data of 3C 66A from VERITAS (Acciari et al., 2009, black points), the de-absorbed spectrum using the EBL model F1.0 (red points) , and using the EBL spectrum F1.6 (blue points). The two lines, labeled 1 and 2, are two different runs of our model to fit the data. The light grey butterfly comes from the FERMI LAT observations taking place at the same time as the VERITAS observations of the source (Reyes et al., 2009). The X-ray part shows observations from the MDM and SWIFT.

the relatively broad and smooth shape of this radiation component. Indeed, since the internal absorption scenario requires a significant attenuation of the VHE radiation over approximately two decades (see Figs. 6.3 and 6.5), the secondary synchrotron component has to be at least 4 decades broad (with additional broadening related to the relativistic motion of the production region). The strong magnetic field required in the proton synchrotron model provides fast cooling of the pairs, thus the radiation spectrum will be featureless without the cooling break. In the case of small size of the production region, the effective particle injection in the blob may be rather narrow, but in this case the flux level will be significantly below the observed points. As it is shown in Fig. 6.5, the synchrotron emission from secondary pairs may explain the X-ray spectrum obtained with Swift, while the optical MDM data require an additional radiation component.

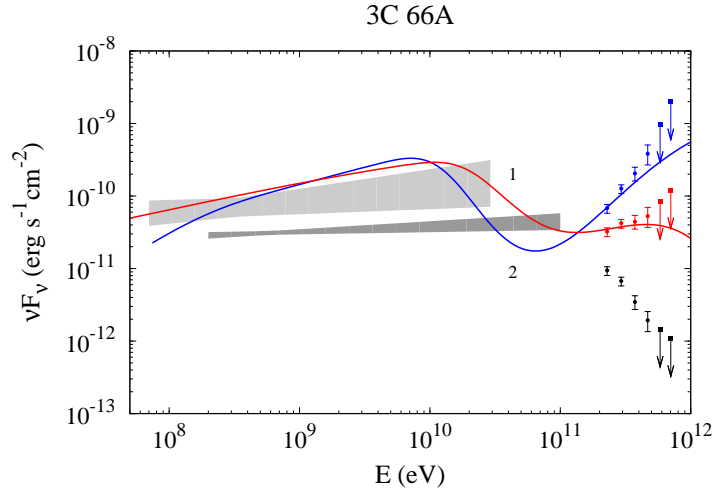As we see, after we get the reconstructed spectra because of the EBL

Figure 6.6 The observational data of 3C 66A from VERITAS (Acciari et al., 2009, black points), the de-absorbed spectrum using the EBL model F1.0 (red points) resulting to $dN/dE \propto E^{-0.36}$, and using the EBL spectrum F1.6 (blue points) resulting to $dN/dE \propto E^{1.36}$. The two lines, labeled 1 and 2, are two different runs of our model to fit the data (see Table 6.2). The light grey butterfly comes from the FERMI LAT observations taking place at the same time as the VERITAS observations of the source (Reyes et al., 2009).

absorption, choosing the right set of parameters gives us a multiwavelength fit of the two sources. The total optical depth of the γ-rays moving inside the region of the soft photons determines how hard the spectrum is, the higher the internal absorption, the harder the spectrum. Then the temperature of the diluted Planckian distribution decides the energy of the γ-rays that are absorbed the most. The choice of the blob size gives us the optical depth inside the blob that determines the transformation ratio of the γ-rays energy to Optical-X-ray photons. For a bigger blob, the absorption inside it is higher so more electron-positron pairs are produced in the blob and their synchrotron radiation is boosted and can be detected. Overall, the parameters can be chosen according to the reconstructed spectrum and the observed Optical/X-ray spectrum and as we saw, the sources' multiwavelength spectrum is fitted successfully.

Chapter 7

MHD Jets

> The important thing in science is not so much to obtain new
> facts as to discover new ways of thinking about them.
> *-Sir William Lawrence Bragg*

7.1 Jets

Jets are long, thin gaseous structures observed in different forms and scales.
They channel away mass, energy, angular momentum and magnetic flux from
stellar, galactic or extra-galactic objects. Geometrically they are narrow
conical or cylindrical/semi-cylindrical ridges. Charged particles are launched
from the disc or between the central object and the disc or from the central
object (different theories exist on the launching region) forming a jet which
remains collimated by strong magnetic fields or a wind, for a distance many
times larger than the radius of the jet. Such a structure is called jet when its
length is at least four times larger than its diameter, when in high resolution
observations it can be distinguished from other extended structures (if any
around) either because of its luminosity contrast or because of its dimensions,

and when it is aligned with a compact nearby source or a protostar. If we have a series of luminous moving knots, then these form a jet if there are more than two such regions or when some of them have been elongated along their length.

The first observation of an astrophysical jet took place in 1918 by Curtis H., when he observed in optical the jet of M87. The term "jet" for extragalactic objects was introduced for the first time in 1954 from Baade and Minkowsky to describe M87, writing on the relevant paper that they could not form at that time a theory on how this jet is formed, on the state of its matter and which mechanism connects the jet with the observed radiation in radio. Since then a lot of jets have been observed, a lot of progress has been made in understanding them but still a lot of questions remain unanswered.

Jets are associated with a variety of objects, Young Stellar Objects, Planetary Nebulae Nuclei, symbiotic stars, microquasars, X-ray Binaries, GRBs, AGN. The mass of the central object can be $1 - 10^9 \, M_\odot$ and its luminosity up to $10^{48} \, erg/s$. Its length can be a few thousands AU or up to a few million parsecs. Although the jets of each of the above objects has different characteristics, there are some common features in all of the jets. Usually the objects associated with jets are compact like white dwarves, neutron stars, black holes, but jets are also associated with protostars. In most of the cases there are 2 jets moving into opposite directions. Some of the jets show knots created because of non-continuous injection of flow that moves with almost the same speed keeping almost a steady distance between each other. Also, at the end of the jet similar features appear. While the jet propagates in the ambient medium, material is accumulated at the edge of the jet causing its deceleration. At the head of the flow a strong shock is formed (Mach disc), which partially thermalizes the jet bulk kinetic energy. The overpressured shocked jet material forms a backflow along the sides of the jet and inflates a cocoon whose size becomes more prominent as the density ratio between jet and ambient material decreases; finally, a second shock (bow-shock) is driven into the external medium.

In most of the observed jets, there is an accretion disc surrounding the central object. It is not clear how the jet is forming but there are indications that its launching is relating to the disc. This is because the disc is both a source of energy and provides the required axial symmetry. In addition, studies on the different classes of objects that produce jets show that the ratio of the observed jet velocity to the escape velocity from the central object, v_j/v_{escape}, is of the order of unity, indicating that jets originate from the centre of the accretion disc. In the case of YSOs, there are observations connecting jets to the centres of accretion discs. As a result any model about the acceleration and collimation of the jets should originate the injection from the disc or the central object and the jet velocity should be of the order of the escape velocity from the disc.

The universal mechanism for jet acceleration and collimation that is widely accepted relies on an accretion disc threaded by a perpendicular large-scale magnetic field (Blandford & Payne, 1982). The classic mechanical analogue for the acceleration mechanism is a bid on a wire. If the wire is the poloidal magnetic field emerging from the surface of an accretion disc, then the bead is an element of the gas. The bead starting from rest at the disc and carried with constant angular velocity by the wire, will be moved outwards if the wire/magnetic field makes an angle of less than 60° to the vector on the disc pointing away from the black hole. The magnetic field lines are anchored on the disc, rotate with it and wound up by the disc rotation. The material is forced to follow the lines and is centrifugally accelerated along them (see Fig. 7.1).

In this study we are interested in the properties of AGN jets. Their typical size is larger than $10^6\,pc$ and charged particles are injected with velocity close to the speed of light. Some of these jets are the largest structures observed in the universe. These particular jets are relativistic, they are formed within a few Schwarzchild radii from the black hole event horizon and some of them show superluminal motion, a geometrical effect occurring in some cases when the jet is almost pointing directly towards Earth.
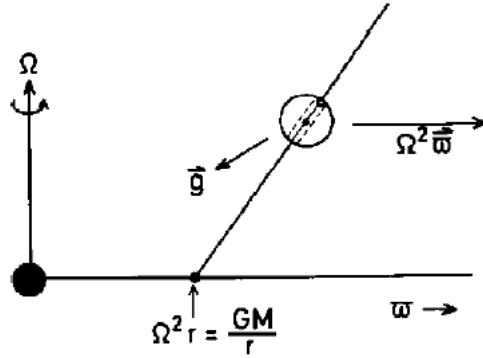
Figure 7.1 The particle is following the magnetic lines and is accelerated due to the centrifugal force. The mechanical analogue is a bid moving on a wire.

The spectrum of AGN jets comes from non-thermal emission, from synchrotron radiation and inverse Compton scattering. There are no emission lines and as a consequence we cannot calculate some basic characteristics like its consistency. But the existence of strong magnetic fields is strongly supported by the observation of the synchrotron emission in the radio band.

Another open question is what kind of particles the jet constists of, it could be electron-protons or electron-positrons. Electrons and positrons emit the same synchrotron radiation spectrum and linear polarization, so it is impossible to verify the existence of positrons. One method that was used to identify the composition of a jet is simulations of relativistic $e^- - e^+$ and $e^- - p$ jets for given kinetic luminosities and jet ambient density ratios (Scheck et al., 2002). The result was that both the morphology and the dynamical behavior is almost independent of the assumed jet composition.

Whatever the consistency of the jet, the charged particles moving inside the jet generate field patterns due to their motion and the field patterns force the particles to move in those orbits, and of course the system is time dependent. The equations describing this problem are too many to be solved. A way to simplify the problem is to treat the jet as a plasma fluid. In this case, the jet launching and the propagation are described with the ideal MHD equations.

7.2 MHD

7.2.1 (R)MHD

As mentioned in Section 7.1, in MHD plasma is treated as a fluid rather than considering each particle independently. The total number of the particles in the jet is too high to deal with each of them individually. Instead, we are treating each fluid element as whole. First some assumptions need to be made about the properties of the system in order for MHD to apply:

(a) the medium cannot be magnetized or polarized: $\varepsilon = \mu = 0$,

(b) flow speeds are small compared to the speed of light: $v/c = \gamma_* \ll 1$,

(c) the speeds of changes in field properties are small compared to the speed of light: $u/c = \beta \ll 1$,

(d) conductivity is high and thus strong electric fields are immediately canceled: $E/B = \alpha \ll 1$,

(e) the displacement current can be ignored compared to the induction current.

MHD is a theory that is linear in α, β and γ_* and ignores all terms of second or higher order of these quantities. Now we can present the MHD equations describing the fluid:

- Maxwell's equations

$$\nabla \cdot \mathbf{E} = 4\pi\rho \,, \tag{7.1}$$

$$\nabla \cdot \mathbf{B} = 0 \tag{7.2}$$

$$\nabla \times \mathbf{E} = -\frac{1}{c}\frac{\partial B}{\partial t} \quad \text{(Faraday's law)} \,, \tag{7.3}$$

$$\nabla \times \mathbf{B} = \frac{4\pi}{c}\mathbf{j} \quad \text{(Ampère's law)} \,; \tag{7.4}$$

$\mathbf{E}$ and $\mathbf{B}$ are the electric and magnetic field, respectively, $\mathbf{j}$ is the current density, ρ is the mass density of the fluid. In the ideal MHD the displacement current in Eq. (7.4) is neglected. This is because there are no space effects

present, the particles have always time to neutralize any charge imbalance on the scale of motion of the plasma.

- Ohm's law

$$\mathbf{j} = \sigma \left(\mathbf{E} + \frac{\mathbf{v} \times \mathbf{B}}{c} \right) ; \qquad (7.5)$$

$\mathbf{v}$ is the velocity at a point of the fluid and σ is the electrical conductivity of the plasma.

- equation of mass continuity

$$\frac{\partial \rho}{\partial t} + \nabla(\mathbf{v}\rho) = 0 ; \qquad (7.6)$$

- equation of motion

$$\rho \frac{\partial \mathbf{v}}{\partial t} + \rho(\mathbf{v} \cdot \nabla)\mathbf{v} = -\nabla p + \frac{\mathbf{j} \times \mathbf{B}}{c} + \rho \mathbf{g} + \mathbf{F}_\nu ; \qquad (7.7)$$

p its pressure, $\mathbf{g}$ is the gravitational acceleration and $\mathbf{F}_\nu$ represents viscous forces. This equation shows that the total force $\rho d\mathbf{v}/dt = \rho \partial \mathbf{v}/\partial t + \rho(\mathbf{v} \cdot \nabla)$ that acts on a particular element of the fluid in the reference frame which moves with the plasma comes from the thermal pressure force $-\nabla p$, the magnetic force $(\mathbf{j} \times \mathbf{B})/c$, the external gravitational force $\rho \mathbf{g}$, and the viscous forces $\mathbf{F}_\nu$.

- adiabatic equation of state

$$\frac{d}{dt} \left(\frac{p}{\rho^\gamma} \right) = 0 . \qquad (7.8)$$

γ is the ratio of specific heats.

Since AGN jets are relativistic, to study them we need the MHD equations that take into account relativistic effects. In the study of the jets we are going

to perform, we consider the case of special relativity, where the jet is moving with Lorentz factor Γ. The external gravitational field of the black hole is important in the launching of the jet and that would demand to include general relativity, but in the case of the propagation of the jet in which we are interested in, is neglected, the jet has already higher velocity than the escape velocity from the black hole. In what follows the speed of light in vacuum is $c = 1$ and the factor $1/\sqrt{(4\pi)}$ is absorbed into the definition of the magnetic field. We use the spacetime metric (-1,1,1,1). The equations given are the ones that the numerical code PLUTO (see Section 7.3), the code we are going to use, is solving:

$$
\frac{\partial}{\partial t}
\begin{pmatrix} D \\ \mathbf{m} \\ E \\ \mathbf{B} \end{pmatrix}
+ \nabla \cdot
\begin{pmatrix} D\mathbf{v} \\ w_t \gamma^2 \mathbf{vv} - \mathbf{bb} + p\mathbf{I} \\ \mathbf{m} \\ \mathbf{vB} - \mathbf{Bv} \end{pmatrix}^T
= \mathbf{0}
\tag{7.9}
$$

where D is the laboratory density, $\mathbf{m}$ is the momentum density, E is the total energy, $\mathbf{v}$ is the velocity and p is the thermal pressure:

$$
\begin{aligned}
D &= \Gamma \rho \\
\mathbf{m} &= w_t \Gamma^2 \mathbf{u} - b^0 \mathbf{b} \\
E &= w_t \Gamma^2 - b^0 b^0 - p_{total}
\end{aligned}
$$

$$
\begin{aligned}
b^0 &= \Gamma \mathbf{v} \cdot \mathbf{B} \\
\mathbf{b} &= \mathbf{B}/\Gamma + \Gamma(\mathbf{v} \cdot \mathbf{B})\mathbf{v} \\
w_t &= \rho h + \mathbf{B}^2/\Gamma^2 + (\mathbf{v} \cdot \mathbf{B})^2 \\
p_{total} &= p + \frac{\mathbf{B}^2/\Gamma^2 + (\mathbf{v} \cdot \mathbf{B})^2}{2}
\end{aligned}
$$

p_{total} is the total plasma pressure, the sum of the thermal and magnetic pressure. Eq. 7.9 shows the conservation laws for the density, momentum and energy. In PLUTO the quasi-linear form of the RMHD is not available, but the momentum density and the energy can be written as:

$$\mathbf{m} = (\rho h \Gamma^2 + |\mathbf{B}|^2)\mathbf{v} - (\mathbf{v} \cdot \mathbf{B})\mathbf{B} \qquad (7.10)$$

$$E = \rho h \gamma^2 - p + \frac{|\mathbf{B}|^2}{2} + \frac{|\mathbf{v}|^2|\mathbf{B}|^2 - (\mathbf{v} \cdot \mathbf{B})^2}{2} \qquad (7.11)$$

The equation that gives the enthalpy is:

$$h = 1 + \frac{\gamma}{\gamma - 1}\frac{p}{\rho} \qquad (7.12)$$

The above equations are coupled and there is no general analytical solution. Numerical simulations are necessary to investigate the problem of relativistic MHD jets.

7.3 Numerical Simulations

In order to study the jets one has to take into account the non linear dynamics involved in the problem. In most cases there are no proper approximations and simplifications to solve the MHD equations analytically and numerical methods are needed. For our study we use the finite volume numerical code PLUTO[1] (Mignone et al., 2007).

7.3.1 Initial and Boundary Conditions

PLUTO solves the MHD equations for different cases, e.g. jets, torus, blasts, shocks, using different approaches i.e., hydrodynamics (HD), RHD, MHD or relativistic magnetohydrodynamics (RMHD). The simulations we run are axisymmetric 2.5-D cylindrical outflows and we use the RMHD module. The numerical code is using a computational box (see Fig. 7.2). Material is

---

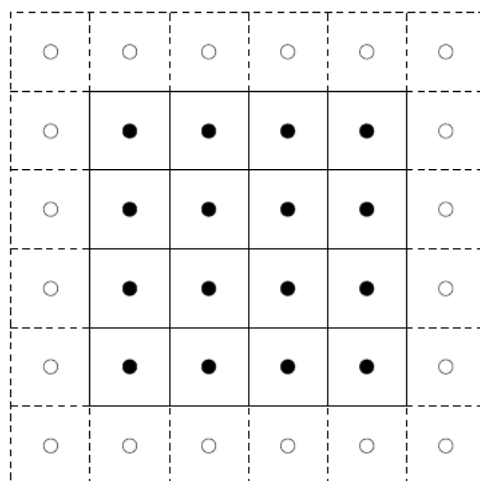[1]The code is public and can be downloaded here: http://plutocode.ph.unito.it/ .

Figure 7.2 The PLUTO grid. The filled circles represent the interior values part of the solution and the empty circles represent the boundary values.

injected from the bottom of the box inside it. So, the bottom of the box is the launching region of the jet and the box itself is the ambient medium in which the jet will propagate. For each simulation we need to set the initial and boundary conditions. The boundary conditions for outflow are:

$$\frac{\partial q}{\partial n} = 0, \ \ \frac{\partial u}{\partial n} = 0 \ \ \frac{\partial B}{\partial n} = 0 \tag{7.13}$$

where q represents the density and the pressure and n is the coordinate orthogonal to the boundary plane. The initial conditions give the values of the parameters inside the box for the ambient medium. With the boundary conditions we set the parameters for the injected jet from the bottom of the box into the box/ambient medium. To succeed this additional ghost cells are assigned outside of the main computational domain (boxes with empty circles in Fig. 7.2).

7.3.2 Problem setup

The physical parameters in PLUTO are normalized and we need to give the normalization factors to estimate the physical values. Three values are

needed, the unit velocity, length and density. The unit velocity that we choose is the speed of light,

$$v_0 = c = 3 \times 10^{10} \ cm$$

so, any speed calculated in PLUTO cannot exceed unity. The unit length we choose is the jet radius estimated for AGN jets and we normalize the jet radius in the grid to 1 unit,

$$\begin{aligned} L_0 = r_j &= 0.05 \ pc \\ &= 10^{17} \ cm \end{aligned}$$

Since the number density for AGN jets is estimated $10^{-5} - 10^{-3} \ cm^{-3}$, using a value of $10^{-4} \ cm^{-3}$ we estimate the unit density for electron population as:

$$\rho_0 = 1.6 \times 10^{-31} \ gr/cm^3$$

and this is also the value of the density inside the jet initially.

The resolution of the grid is 100×300 and its the normalized size is 10×30. Using the above unit parameters we can estimate that the physical size of the box of the simulations is $0.5 \times 1.5 \ pc$. The unit time corresponding to these values is

$$t_0 = \frac{L_0}{v_0} = 5 \times 10^6 \ sec.$$

The simulations we are going to present run for t=35 or $t \simeq 5.6$ yrs. Correspondingly the unit pressure and magnetic field are:

$$p_0 = \rho_0 v_0^2 = 1.4 \times 10^{-10} \ \text{Ba},$$

$$B_0 = \sqrt{4\pi \rho_0 v_0^2} = 4.2 \times 10^{-5} \ \text{G}$$

From so on when we give a value of a parameter without units, then we refer to the normalized parameter, otherwise cgs units are used.

As we mentioned, The initial value of the jet density is $\rho_j = 1$. For the

density of the ambient medium we are going to use the value $\rho_e = 10$, since AGN jets are underdense. The ratio between the ambient and jet density can be as high as 10^5, (Massaglia et al., 1996). It is demonstrated that the morphology of an overdense propagating jet is different than the one of an underdense jet, with the latter one to be closer into morphology with the observations. Here, we look in less dense environments that lead to more stable jet configurations over longer distances.

Inside the box, initially, the density of the ambient medium is $\rho_e = 10$ and there is only one component of the magnetic field present, $B_z = 1$. The external pressure is not the same for all the simulations, so it will be given in each case seperately. Also, the ambient gas has zero velocity, $v_z = v_r = v_\phi = 0$.

For the boundary conditions, the jet is injected along the z-axis and only the v_j component of the velocity is present. However, in our calculations is not the velocity that is prescribed but the Lorentz factor Γ. So, the velocity is calculated accordingly:

$$v_j = \sqrt{1 - \frac{1}{\Gamma^2}} \tag{7.14}$$

At this point we should note, that the Mach number, the Lorentz factor and the ratio of the jet to the ambient density in the AGN jet can not be constrained directly by observations (Massaglia, 2003). And these are the three minimum parameters for analytical and numerical modeling of jets. Only statistical statistical analyzes can be used like in Giovannini et al. (2001) where it is concluded that the Lorentz factor of FR I and II AGN is $3 < \gamma < 10$.

The jet is injected with pressure $p_j = 0.5$. The magnetic field of the jet has a z- and ϕ-component, $B_z = 1$ and $B_\phi = 0.5r$, $r \leq 1$. All the boundary conditions for the jet are set for $r \leq 1$, for the region inside the jet radius. The polytropic index used is $\gamma = 4/3$. The normalized parameters and the physical values are given in Table 7.1. The parameters that change depending the simulation are not mentioned on the table and are given when each simulation is discussed.

Table 7.1 The quantities below are the initial values of the jet parameters ($r \leq 1$) used in all the simulations of this study.

	Jet parameters	
	normalized	cgs
ρ_j	1	1.6×10^{-31}
P_j	0.5	7×10^{-11}
v_r	0	0
v_ϕ	0	0
B_z	1	4.2×10^{-5}
B_r	0	0
B_ϕ	0.5r	$2.1 \times 10^{-5} r/r_j$

7.4 Results

We are interested in setups that result in compression of the magnetic field. Compression of plasma and magnetic field leads to enhancement of the latter one, because of conservation of magnetic flux. Such a configuration can lead to acceleration of particles in high energies and production of synchrotron radiation. This is the point where this work is connected with the proton synchrotron model described in Chapter 5, numerical simulations could verify our theoretical model.

We have to note that our results are preliminary, therefore they can only give us indications for future investigations. We compare simulations with variable injection profiles and with steady outflow. Two sets of simulations are presented. The first one in Sec. 7.4.1 deals with a jet with steady in time injection (steady Lorentz factor) and a jet with variable in time Lorentz factor. The second set compares two jets with variable Γ and different thermal to magnetic pressure ratio.

At this point we should introduce some quantities that we are going to use, the Mach numbers. The Mach number is the ratio between the jet speed

v_j and the speed of sound c_s,

$$M = \frac{v_j}{c_s},$$ (7.15)

c_s is calculated as

$$c_s = \sqrt{\frac{\gamma(\gamma - 1)P}{(\gamma - 1)\rho + \gamma P}}$$ (7.16)

where γ is the polytropic index, ρ the density of the medium and P the pressure. For the density and the pressure we can give two set of values, one set corresponds to the interior of the jet and the second one to the ambient medium. So two Mach numbers can be calculated, an internal and an external one, respectively. If we are interested in the behaviour of the terminal shock which is forming because of the interaction of the jet with the ambient medium, then we are interested in the external Mach number, M_{ext}. If we are looking for internal shocks and how the fluid behaves inside the jet, then the internal Mach number, M_{int} will give us the necessary information. When the flow is supersonic, shock waves can be formed. High internal Mach number means that internal shocks can be formed. We should add at this point that shock waves are characterized by an abrupt, nearly discontinuous change in the characteristics of the medium. Between the upstream and downstream region there is always an extremely rapid rise in pressure, temperature and density of the flow. The actual difference between a supersonic and subsonic jet is that in the latter one, whatever perturbation takes place, it will propagate through the whole jet, both downstream and upstream, affecting the initial conditions that we set. On the other hand, if the flow is supersonic, then any perturbation will affect the jet only in the downstream part. However, since we are dealing with relativistic jets, we need to use the relativistic Mach number,

$$\mathcal{M} = M\frac{\Gamma}{\Gamma_s}$$ (7.17)

where $\Gamma_s = 1/\sqrt{1 - c_s^2}$ is the Lorentz factor computed from the sound speed.

Another number we are going to calculate is the Alfvén Mach number $M_a = v_j/v_a$, the jet over the Alfvén velocity (Lichnerowicz, 1967)

$$v_a = \sqrt{\frac{\sigma}{\sigma + 1 + \frac{\gamma p}{(\gamma-1)\rho}}}, \tag{7.18}$$

where σ is the ratio of magnetic to rest-mass energy density

$$\sigma = \frac{2P_{mag}}{\rho}. \tag{7.19}$$

In ideal MHD, plasma and magnetic fields are tightly coupled ("frozen in" condition). In a very simplified view, if the flow is sub-alfvenic ($M_a \leq 1$), then the magnetic field is "strong" and the plasma follows the field lines. Conversely, if the flow is super-alfvenic ($M_a \geq 1$) then the field is "weak" and the field lines are dragged by the fluid motion. The Alfvén Mach number then gives us an idea of how strongly the magnetic field is able to influence the dynamic of the plasma.

7.4.1 Variable and Non-Variable Jet Injection

In this section we present the preliminary results of our study on the differences appearing in time-dependent and independent Lorentz factor jet simulations. For the values of the jet initial parameters see Table 7.1. The external pressure for both simulations is $P_e = 0.5$ or $P_e = 7 \times 10^{-11}$ Ba. Simulation A has a steady in time Lorentz factor, $\Gamma = 10$. However, simulation B has Lorentz factor changing with time as:

$$\Gamma = \text{Max}[\Gamma_{min}, \Gamma_{max} \sin^4(t)] \tag{7.20}$$

In Fig. 7.3 the Lorentz factor is shown when $\Gamma_{min} = 5$ and $\Gamma_{max} = 10$, which are the values we are going to use in our simulations. Changing the Lorentz factor instead of the velocity removes any concern on having velocities higher than the speed of light and the condition $v \leq 1$ is always satisfied.
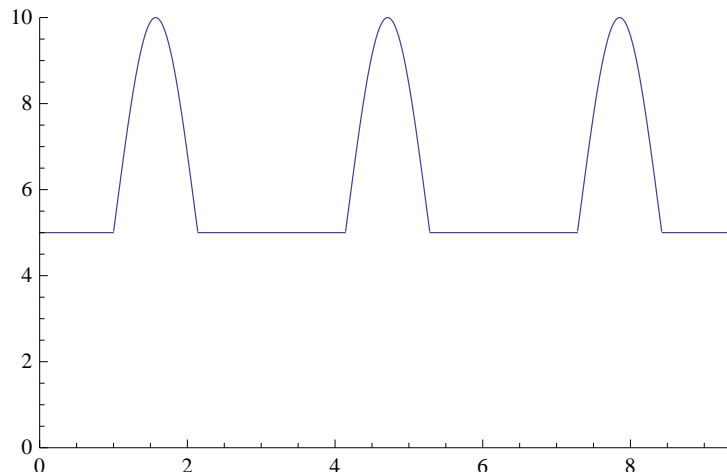
Figure 7.3 The time dependent Lorentz factor described in Eq. 7.20 for $\Gamma_{min} = 5$ and $\Gamma_{max} = 10$.

The internal speed of sound c_{s_int}, the external speed of sound c_{s_ext} of the ambient medium, the corresponding Mach numbers for the non-relativistic and relativistic case and the Alfvén number are shown in Table 7.2. For both simulations these values are the same. The only difference is that simulation B has a maximum and minimum value of the internal and external relativistic Mach number, both of these numbers change as the Lorentz factor is changing, $\mathcal{M} \propto \Gamma$. In the table it is listed only the maximum number that the relativistic Mach numbers can have. The minimum values are $0.5\mathcal{M}$. We note that both simulations produce supersonic flows. But judging from the Mach number the shocks created in simulation B are slightly weaker than the ones in simulation A.

In Fig. 7.4 the density map (logscale) of a jet with steady Lorentz factor is shown for different times, t=5, 15, 25 and 35. The same maps for simulation B are shown in Fig. 7.5. Observing the density plots we notice that the jet in both simulations follows the general structure observed in previous simulations by Norman et al. (1982) and Massaglia et al. (1996). In particular, both jets produce a bow shock in the external medium, as expected. Since the relativistic external mach number is the same, we expect the same behaviour for this shock. The simulations confirm this point. The only difference regards
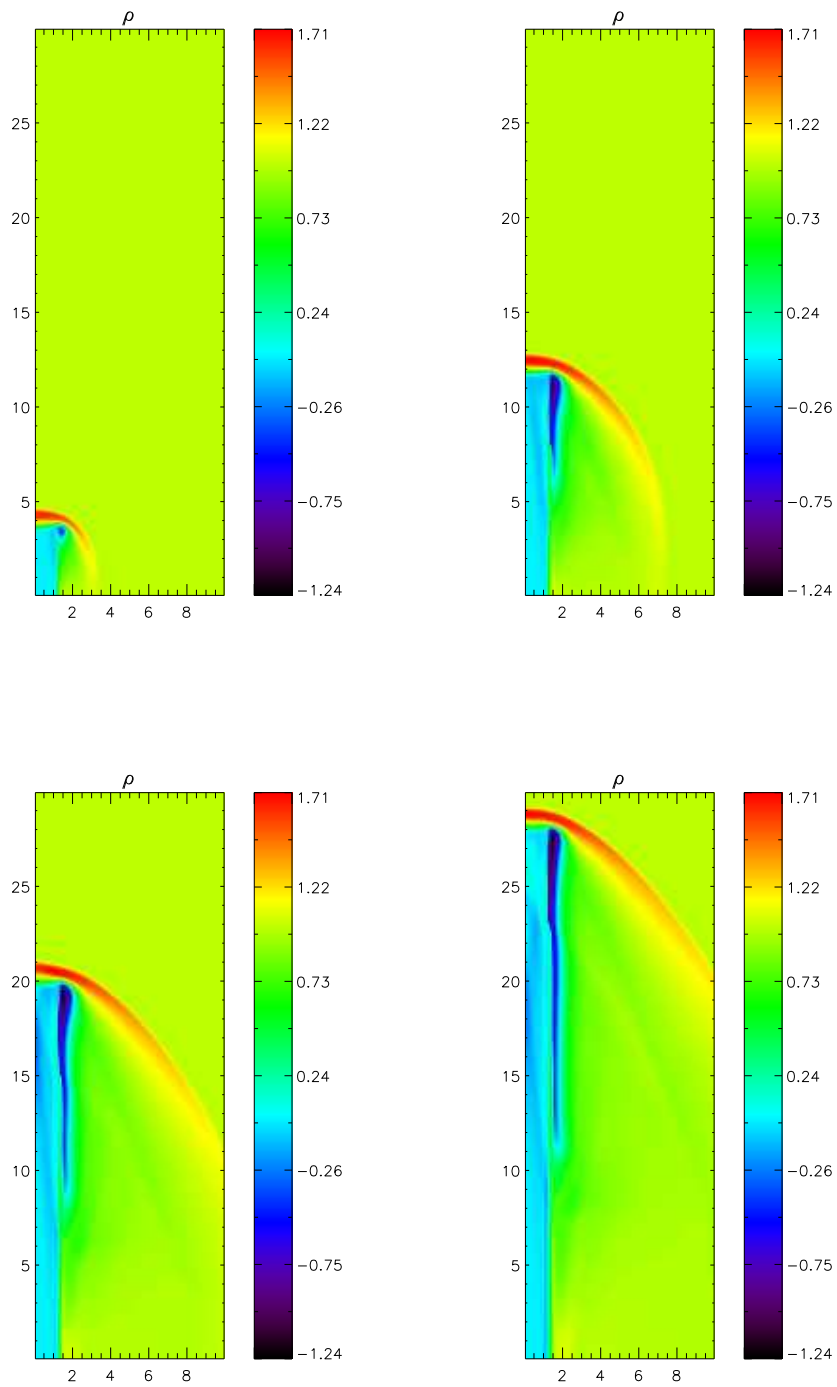
Figure 7.4 The density map in log scale for the simulation A for four different times, t=5, 15, 25, 35 from top left clockwise.
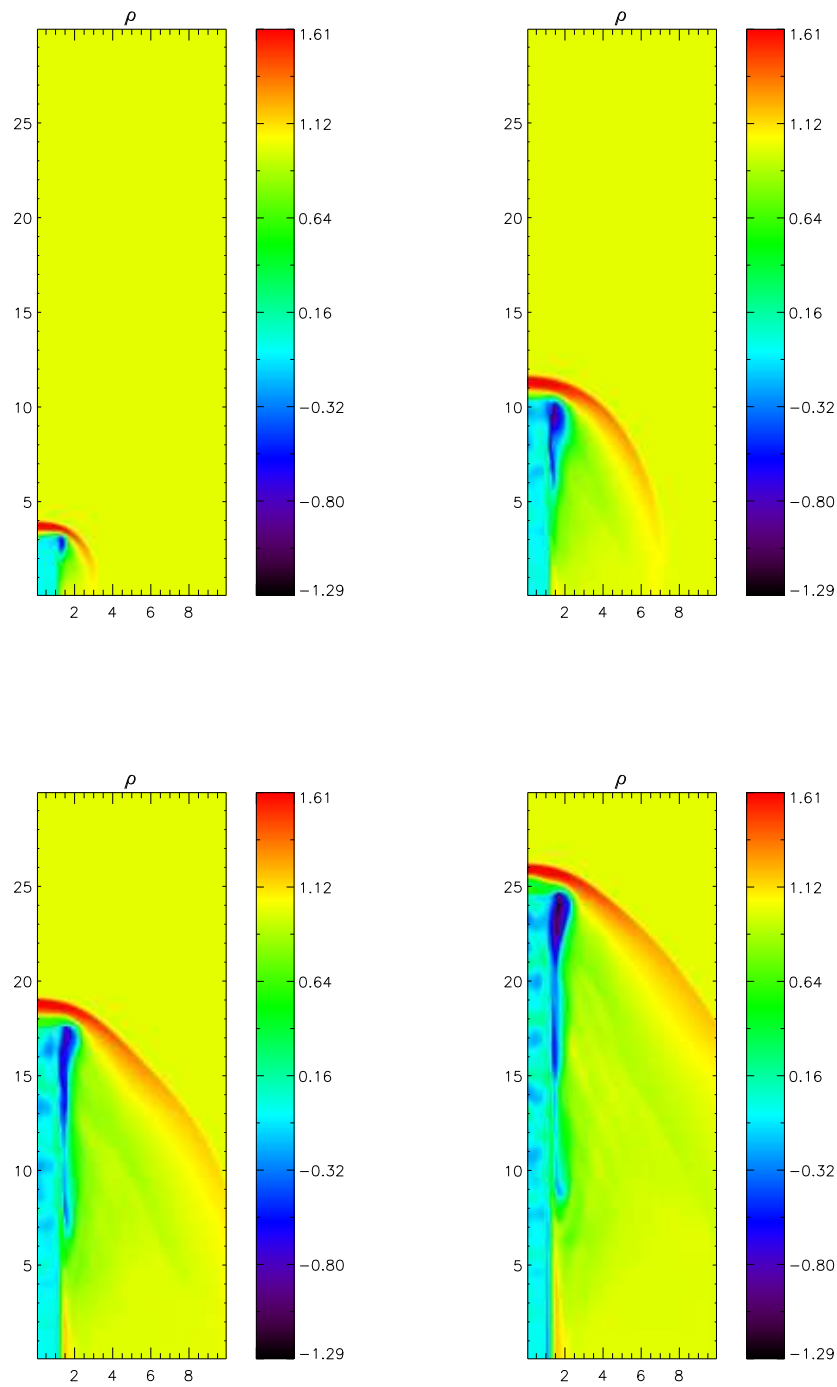
Figure 7.5 The density map in log-scale for the simulation B for four different times, t=5, 15, 25, 35 from top left clockwise.

Table 7.2 The quantities below are calculated for the simulation of jets with steady (simulation A) and variable injection (simulation B). In case of B, the maximum numbers of $\mathcal{M}$ are given.

	Simulations
	A & B
c_{s_int}	0.47
c_{s_ext}	0.24
M_{int}	2.11
M_{ext}	4.22
$\mathcal{M}_{int}$	18.6
$\mathcal{M}_{ext}$	41
M_a	14.5
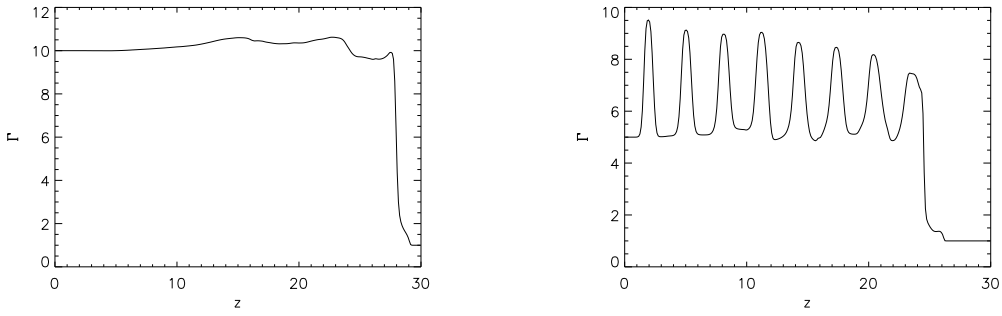
Figure 7.6 The variable Lorentz factor over the z-axis for $r = 0.45r_j$ for t=35. On the left simulation A and on the right simulation B.
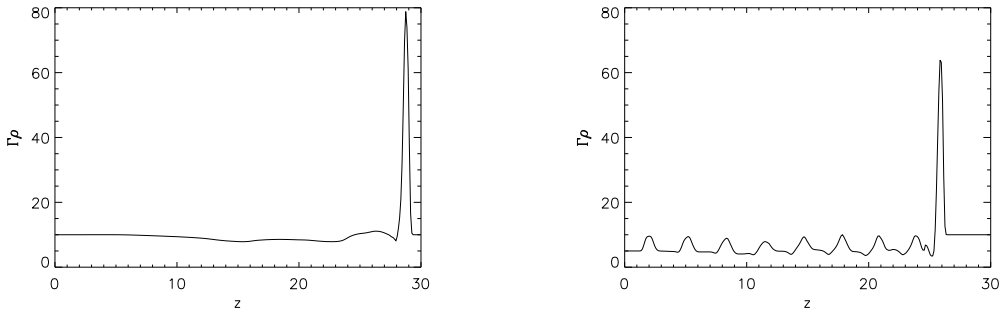
Figure 7.7 The conserved relativistic quantity $\Gamma\rho$ over the z-axis for $r = 0.45r_j$ for t=35. On the left simulation A and on the right simulation B.
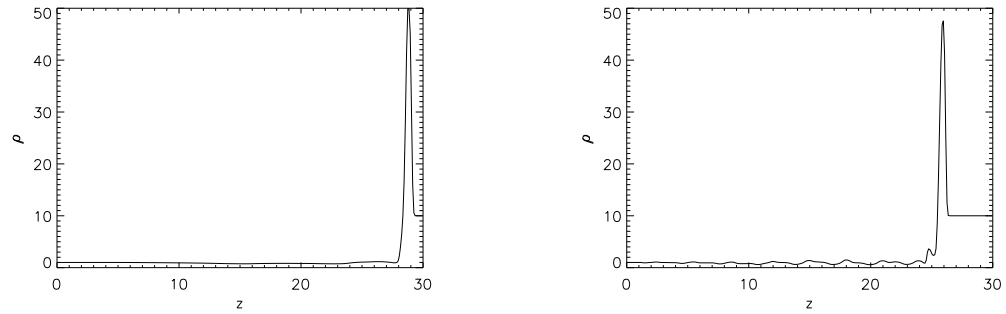
Figure 7.8 The conserved relativistic quantity ρ over the z-axis for $r = 0.45r_j$ for t=35. On the left simulation A and on the right simulation B.
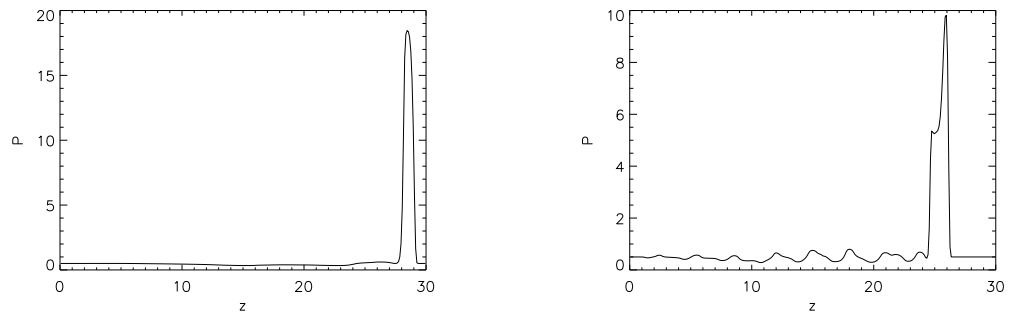
Figure 7.9 The pressure over the z-axis for $r = 0.45r_j$ for t=35. On the left simulation A and on the right simulation B.
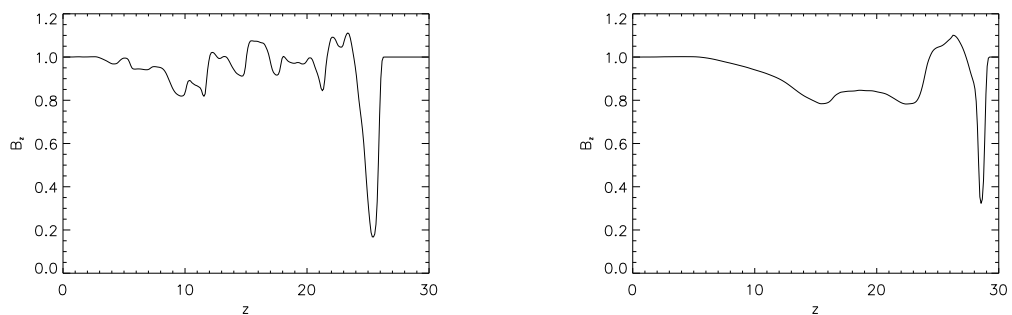

Figure 7.10 The magnetic component B_z over the z-axis for $r = 0.45r_j$ for t=35. On the left simulation A and on the right simulation B.
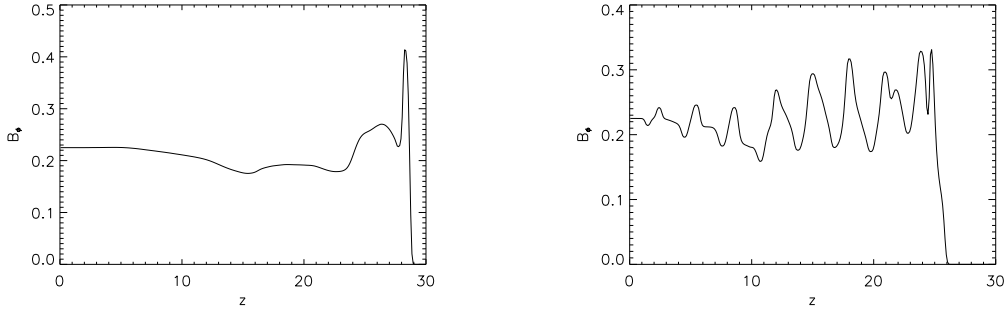
Figure 7.11 The magnetic component B_ϕ over the z-axis for $r = 0.45r_j$ for t=35. On the left simulation A and on the right simulation B.

the length of the jet. As expected, the jet with the steady Lorentz factor manages to propagate further than the one in simulation B, since on average its injection velocity is higher. Despite the variability in the Gamma factor, in both simulations the flow is decelerated at the jet head by a strong shock (Mach disc), which partially thermalizes the jet bulk kinetic energy. Once shocked by the Mach disc, the jet material forms a backflow along the sides of the jet, clearly visible in the simulations as the dark blue stripe going down from the jet head. Despite the variability in Γ, in both simulations the flow is decelerated at the jet head and the Mach disc is formed, which partially thermalizes the jet bulk kinetic energy. Once shocked by the Mach disc, the jet material forms a backflow along the sides of the jet, clearly visibly in the simulations as the dark blue stripe going down from the jet head. However, the backflow in simulation B is perturbated, possibly because it is influenced by the not so smooth jet.

In Fig. 7.6 the Lorentz factor is plotted for t=35 along the jet when $r = 0.45r_j$. It is clear how the Lorentz factor is changing according to Eq. 7.20 for simulation B (right panel) and that is decreasing as it moves deeper inside the ambient medium. Such a decrease is expected since the jet is decelerated while more material is accumulating at the jet termination shock, decelerating the jet. On the right panel one can see that the Lorentz factor for simulation a does not show almost any change and towards the end

of the jet there is even a small increase in its value.

In Fig. 7.7 it is plotted the observed quantity $\Gamma\rho$, in Fig. 7.8 the density, in Fig. 7.9 the thermal pressure, in Fig. 7.10 the B_z and in Fig. 7.11 the B_ϕ, along the jet axis at $r = 0.45r_j$ and for $t = 35$. As expected in both cases at the termination shock there is a strong change in the density and in the pressure. The change in the density is comparable in both the simulations. However, simulation A shows higher change in the pressure, from 0.5 to 18, when in simulation B the maximum pressure is ~ 10, almost two times lower. The difference could be because in simulation A the jet has higher velocity than in simulation B, creating a stronger shock. The result is in accordance with the estimated Mach numbers. Looking at the plots of the magnetic field we see that there is no important compression of B_ϕ as we would like to have and the change in B_ϕ is slightly higher in simulation A. However, the value of B_ϕ in simulation B is changing periodically as Γ.

7.4.2 Variable Lorentz factor and Differences in Pressure

In this section we present the preliminary results of two simulations, simulation A' and B. In both of them the Lorentz factor is changing with time as:

$$\Gamma(t) = \text{Max}[\Gamma_{min}, \Gamma_{max} \sin^4(t)] \tag{7.21}$$

with $\Gamma_{min} = 5$ and $\Gamma_{max} = 10$ (see Fig. 7.3 for a plot of the function). The parameters chosen for the physical quantities are shown in Table 7.1. Simulation B is the same as simulation B in Section 7.4.1. The difference between A' and B lays on the pressure of the ambient medium. For simulation A' $P_e = 5$ or $P_e = 7 \times 10^{-10}$ Ba and for simulation B $P_e = 0.5$ or $P_e = 7 \times 10^{-11}$ Ba, the same value as the pressure of the jet initially.

The only difference between the two simulations is the value of the pressure inside and out of the jet. However, we can express this difference in the

Table 7.3 The quantities below are calculated for the simulation A' and B for jets with variable injection profiles.

	Simulations	
	A'	B
c_{s_int}	0.56	0.47
c_{s_ext}	0.24	0.24
M_{int}	1.77	2.11
M_{ext}	4.22	4.22
$\mathcal{M}_{int}$	14.6	18.6
$\mathcal{M}_{ext}$	41	41
M_a	14.5	14.5

value of the plasma β parameter

$$\beta = \frac{P}{B^2/2},\tag{7.22}$$

the ratio between the thermal pressure and the magnetic pressure. This parameter gives us the relative importance of the thermal pressure over the magnetic field as the restoring force to any disturbance. If $\beta \gg 1$, then the magnetic force is negligible on the dynamics but the magnetic field is still advected by the flow. In the opposite case that $\beta \ll 1$, it is the gas pressure that is negligible but it can influence slightly the geometry of any equilibrium. In our case, with the given values of parameters, the initial β depends on the radial position inside the jet:

$$\beta = \begin{cases} \frac{10}{1+0.25r^2}, & \text{simulation A'} \\ \frac{1}{1+0.25r^2}, & \text{simulation B} \end{cases}\tag{7.23}$$

The maximum value that β can have is 10 or 1 at centre of the jet and the minimum value is 8 or 0.8 at the jet radius, for simulation A' and B respectively. We see that there is a difference of factor of 10 between the maximum and minimum values of the two simulations, since $P_{A'} = 10 P_B$.

In Fig. 7.4 and 7.12 the density maps of the two simulations are presented

for four different times of the simulation, t=5, 15, 25, 35, so we can see their evolution in time. We can see in simulation B that the gas is better confined by the magnetic toroidal field inside the jet. However, in simulation A' where the thermal pressure is more important compared to the magnetic force, more complicated morphology is developed in the jet. In addition the jet in simulation A' does not propagate as long as in simulation B, $z \simeq 24$ instead of $z \simeq 26$. This is expected looking at Fig. 7.13, the Lorentz factor Γ over z at distance $0.45r_j$ from the centre of the jet. Γ is oscillating over time but the different layers of the jet with the higher Lorentz factors almost maintain its value while moving through the jet, left panel of Fig. 7.13. Of course, it is expected that there will be a deceleration of the jet because of its interaction with the ambient medium, that is being reflected in the value of Γ. In A' case, after $z \simeq 10$, the jet loses its strict cylindrical shape and the Lorentz factor of some jet layers that begun with high Γ, have been decelerated, resulting to a slower jet. But in both cases, it is clear how the Lorentz factor is changing over time.

We obtain a similar figure if we plot the conserved quantity $\Gamma\rho$ that is observed from Earth, over z, as shown in Fig. 7.14, again for $r = 0.45r_j$ and t=35 (see also the map for t=35 of $\Gamma\rho$ in Fig. 7.19). In addition we can see the final shock created where the jet is moving through the ambient medium. In case B there is one final shock where the density is changing from 1 to ~ 50. In case A' the density at the final shock has increased from 1 to ~ 25, but another region with increased density has been formed at $z \simeq 10$ with density ~ 10, see Fig. 7.15. We are interested in having strong shocks in order to have the right environment for radiation emission. That is the reason why we should investigate also the behaviour of B_ϕ, Fig. 7.18, of pressure, Fig. 7.16. In case B the B_ϕ is not changing a lot and no important compression of the magnetic field is present, not even at the final shock. On the other hand, in case A' there a two regions where the magnetic field component is compressed, at the end of the jet and at $z = 10$. The pressure shows similar behaviour with the difference that in case B the pressure in
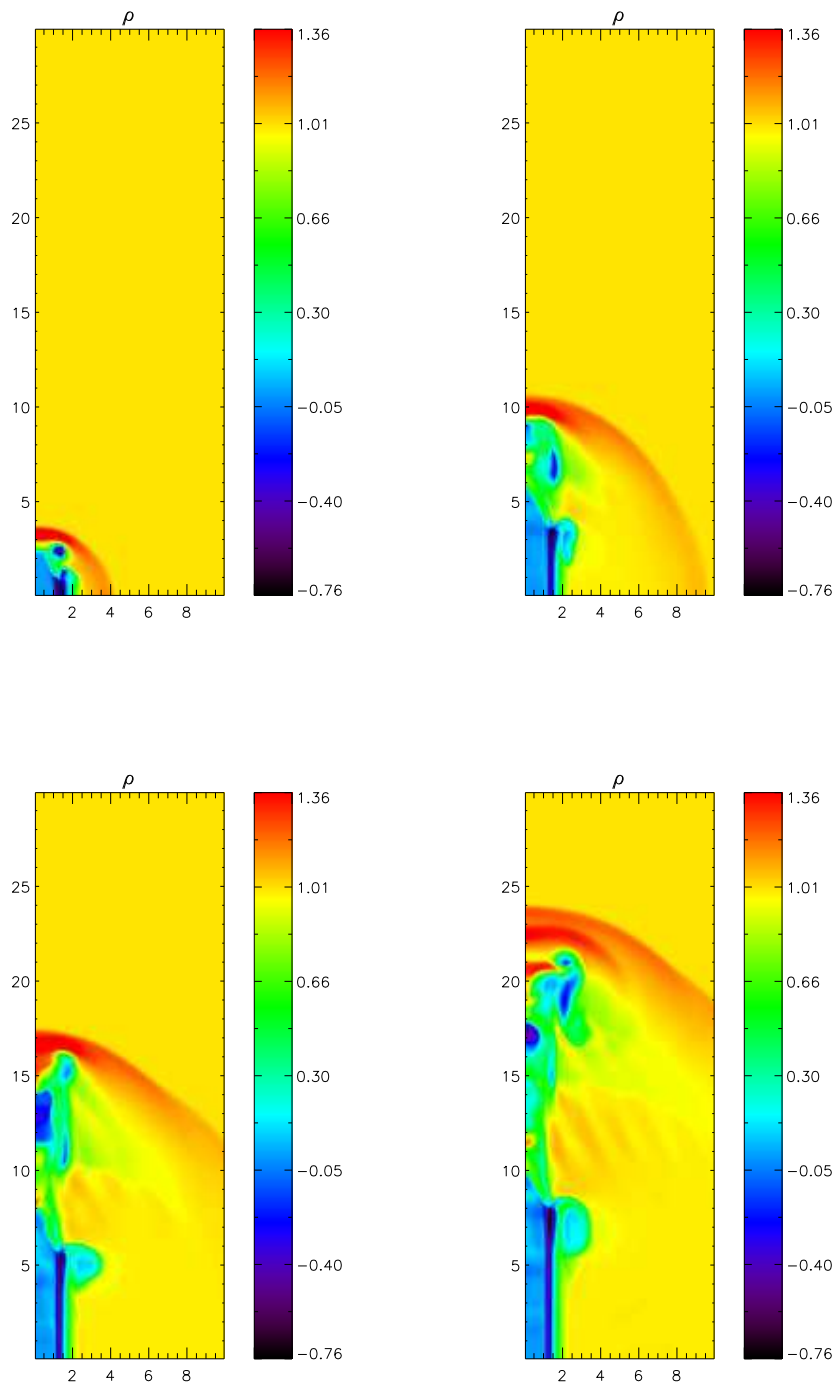
105

Figure 7.12 The density map in log scale for the simulation B for four different times, t=5, 15, 25, 35 from top left clockwise.
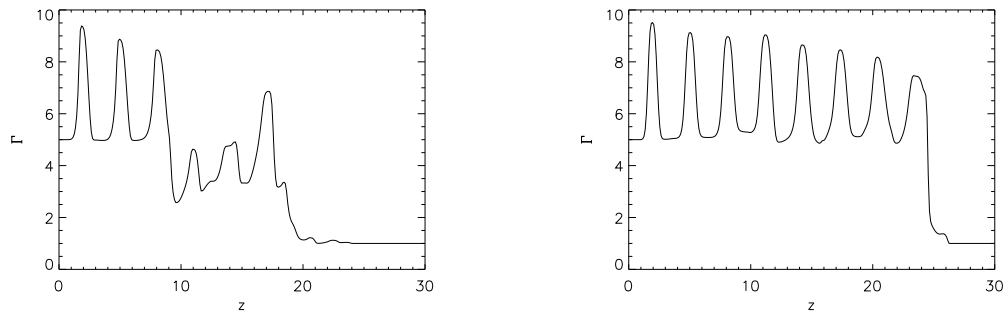
Figure 7.13 The variable Lorentz factor over the z-axis for $r = 0.45_j$ for t=35. On the left simulation A and on the right simulation B.

the final shock is increased more than in case A'. Further investigation is needed to understand why the magnetic field compression is present only in simulation A' and what is happening in $z = 10$. To be complete, in Fig. 7.17 the z-component of the magnetic field is plotted.

The values of the Mach numbers are on Table 7.3. Both outflows are supersonic. The Alfvén Mach number is $M_a = 14.5$ for both simulations. This suggests that the magnetic field does not play a dominant role in the dynamics of the jets, but it follows the flow. Therefore, in both cases shocks and plasma compressions will be able to compress and amplify the magnetic field as well. On the other hand, comparing the two different plasma beta parameters, we can expect that the jet in simulation B will be more tightly constrained by the presence of the magnetic field. Although the internal Mach number of simulation B is a bit higher than the one of simulation A', it is actually during simulation A' that we notice morphology that could be internal shocks. More investigation on the topic is required.

In summary, our simulations suggest that the behaviour of relativistic pulsating jets is strongly influenced by the value of the beta parameter. Moreover, simulations indicate that a bigger value of the plasma beta is more favorable for the production of the conditions necessary for a strong synchrotron emission. Indeed, the initially less important magnetic field allows the formation of shocks and structures which lead to higher compression.
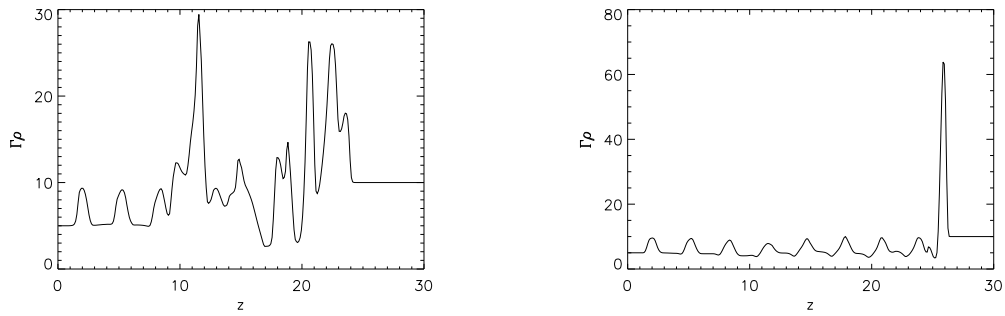
Figure 7.14 The conserved relativistic quantity $\Gamma\rho$ over the z-axis for $r = 0.45r_j$ for t=35. On the left simulation A and on the right simulation B.
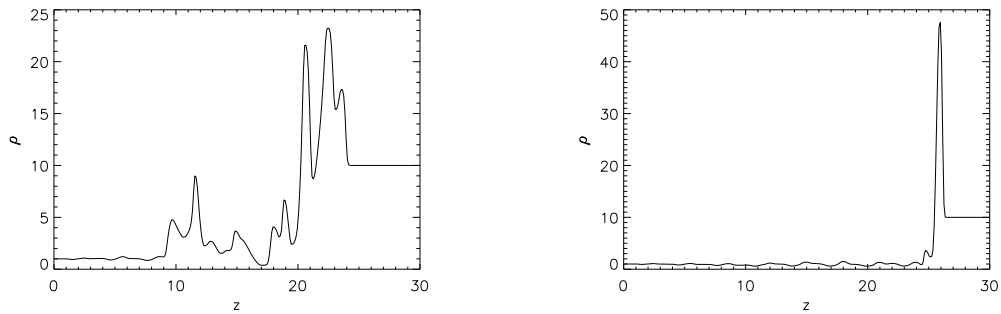

Figure 7.15 The conserved relativistic quantity ρ over the z-axis for $r = 0.45r_j$ for t=35. On the left simulation A and on the right simulation B.
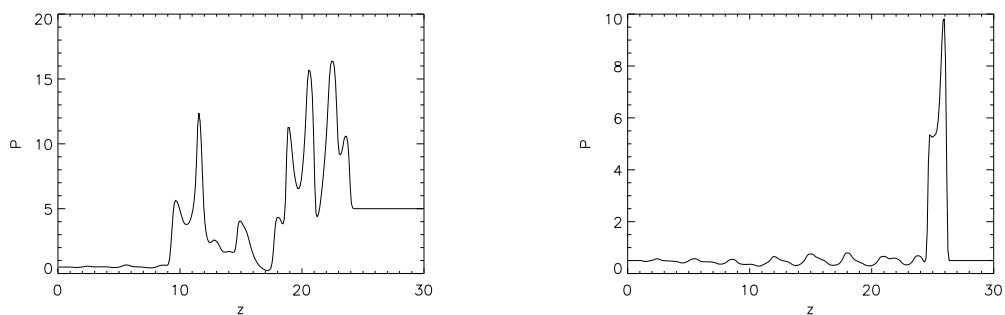

Figure 7.16 The pressure over the z-axis for $r = 0.45r_j$ for t=35. On the left simulation A and on the right simulation B.
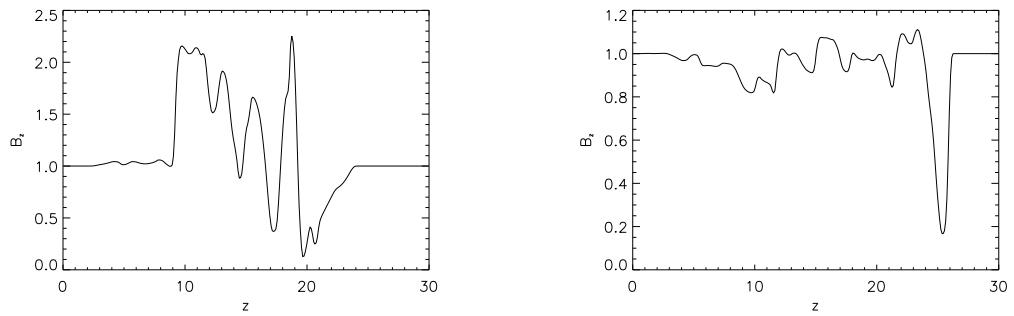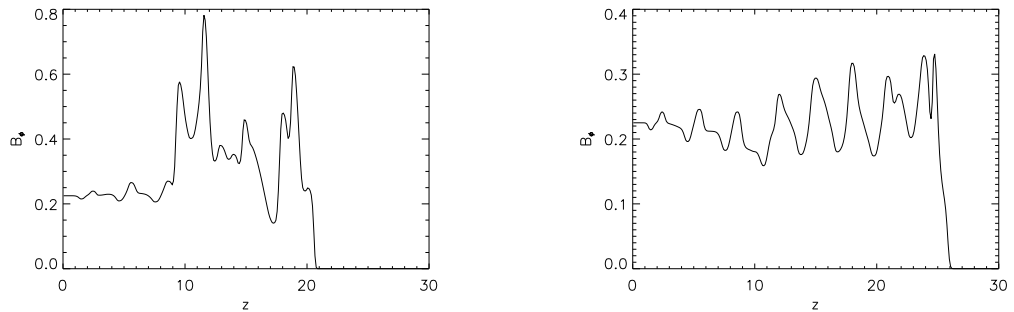
108

Figure 7.17 The magnetic component B_z over the z-axis for $r = 0.45r_j$ for t=35. On the left simulation A and on the right simulation B.

Figure 7.18 The magnetic component B_ϕ over the z-axis for $r = 0.45r_j$ for t=35. On the left simulation A and on the right simulation B.
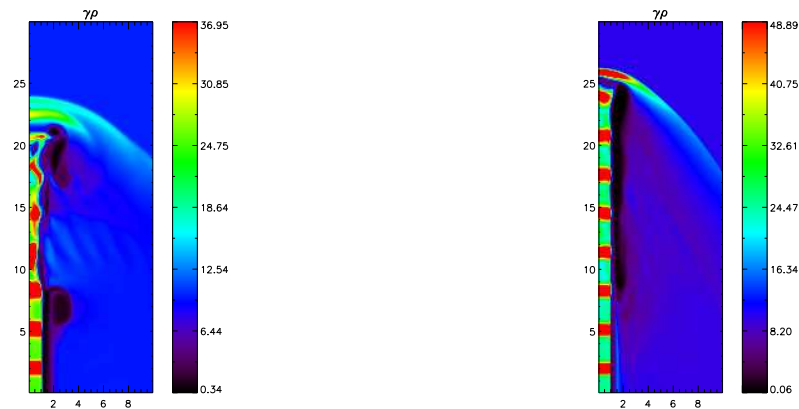

Figure 7.19 The variable Lorentz factor over the z-axis for $r = 0.45r_j$ for t=35. On the left simulation A and on the right simulation B.

Further investigation is needed to understand precisely why the magnetic field compression is present mainly in simulation A' but almost absent in B, and what are the dynamical processes leading to the features observed at $z \sim 10$.

Conclusions

> Nothing exists except atoms and empty space;
> everything else is opinion.
> *-Democritus*

The motivation of this dissertation was to better understand the unusually hard spectra observed in some blazars, in some cases as hard as $dN/dE \propto E^{-1.5}$, having the observations as a starting point. From what we observe until the fitting of the spectrum, there is an intermediate challenging step, the EBL correction. High energy γ-rays are attenuated by the EBL photon field and the larger the distance to the source, the stronger the effects are. The spectrum needs to be corrected for this attenuation. The real challenge lays on the estimation of the EBL spectrum. Observations of EBL cannot restrict its spectrum sufficiently, some of the problems are the strong foregrounds difficult to be reduced from the observations or the uncertainties in the star formation rate and the evolution models applied to estimate the cosmic EBL evolution. The result is a variety of EBL estimations/models that influence the final behaviour of the blazars' intrinsic spectrum since the attenuation is quite sensitive to the EBL energy density. Trying to cover different cases, we chose to use two different EBL levels. The first one comes from the EBL model of Franceschini et al. (2008) (F1.0) and the second one comes from the scaling of F1.0 by a factor of 1.6 to include a lower limit of

EBL derived at 3.6 μm of $9.0^{+1.7}_{-0.9} \, nWm^{-2}sr^{-1}$ in Levenson & Wright (2008). It is shown in Chap. 4 that even this small difference of 1.6 can result to a much harder spectrum, e.g. from $dN/dE \propto E^{-1.4}$ to $dN/dE \propto E^{-0.4}$ in the case of 3C 66A, that current models fail to describe.

After the reconstruction of the blazar spectrum, we move directly to the modeling (Chap. 5) using a proton synchrotron model. Protons are accelerated in very high energies and produce γ-rays through synchrotron radiation in the presence of strong magnetic fields. We assume that the γ-rays are produced inside a blob that moves relativistically with Lorentz factor Γ. If the blob is moving inside a soft photon field, then we have internal absorption and the γ-rays will be attenuated due to pair production. For a Planckian distribution of the soft photons, we show that an arbitrary hard spectrum can be produced by changing the optical depth of the γ-rays' attenuation. We show that the sources' spectrum is fitted by the model, combining the right values of the magnetic field and the temperature of the diluted Planckian distribution, for both of the two different EBL spectra.

In addition, the energy lost because of the absorption is transferred to electron-positron pairs that emit synchrotron radiation in the Optical/X-ray regime through synchrotron radiation. The secondary pairs that are created inside the blob have their radiation boosted and possibly detectable, but the radiation of the pairs created out of the blob cannot be observed because it is not boosted. The detectable radiation is constrained by the optical depth of the blob. Although the γ-rays produced by the protons undergo attenuation as long as they move inside the photon field region, only the part of them that is absorbed inside the blob will create pairs that in their turn will produce detectable radiation in the Optical/X-ray regime. The model can describe the multiwavelength spectrum of 1ES 0229+200 and 3C 66A with success, taking into account also the upper limits introduced by FERMI LAT in the GeV regime (Chap. 6).

Towards an attempt to study further the radiation from blazars, we perform some numerical simulations (Chap. 7). Knowing that compression of

the magnetic field means acceleration of particles and radiation, we search for a physical configuration that can produce internal shocks, regions prominent to produce synchrotron radiation. Using the numerical code PLUTO and choosing a basic setup for a relativistic MHD jet with time independent or time variable Lorentz factor, we investigate the properties of the formed jet. We are not interested in the launching of the jet but only on the propagation. For a certain configuration, while the Lorentz factor is changing with time as $\Gamma(t) = \mathrm{Max}[\Gamma_{min}, \Gamma_{max} \sin^4(t)]$, compression of the magnetic field is produced. The results we presented here are only preliminary and the estimation of radiation was not done. However, our findings are encouraging to continue the study and find the proper setup that results to internal shocks and estimate the produced radiation.

A step forward for the current work would be the improvement of the instrumentation. So far the available Cherenkov telescopes have their maximum sensitivity at $\sim TeV$ and the low energy threshold is at 100 GeV (except from MAGIC). Distant sources often are detected only when there is a flare incidence. An increase to the sensitivity of the instruments and a lower energy threshold would be helpful in order to get high energy spectrum in a wider energy range and possibly in less observational time. Cherenkov Telescope Array (CTA) is a promising new project that with its completion we will have an instrument at least 10 times more sensitive in the region of $0.1 - 50 \, TeV$ and it will allow thousand new sources to be detected (Wagner et al., 2009). At the same time, the increased sensitivity will allow shorter observation times, higher time resolution of variable sources (sub-minute resolution instead of the current resolution of minutes) and more follow-up observations.

With the new window on the high energy universe that will open on observations, we will be able to get detailed spectra from the VHE sources and if we take advantage of multiwavelength campaigns, we could have simultaneous observations in all the energy bands. A more thorough study would be possible. In addition, more sources will be detected and their spectra will

be available for study. It would be interesting to have a larger sample of blazars to see how many of them have hard spectrum, what are the values of the physical parameters that our model gives in order to describe them and whether there is a pattern behind the required parameters.

Acronyms

Aknowledgements

Real life isn't always going to be perfect or go our way,
but the recurring acknowledgement of what is working in our lives
can help us not only to survive but surmount our difficulties.
-Sarah Ban Breathnach

I feel very privileged that I have so many people to thank. First of all I would like to thank Prof. Aharonian for his supervision, his inspiration and passion. I learnt a lot from him and I admire his approach on physics. Then I would like to thank PD Dr. Fendt for his guidance during my first contact with numerical simulations and for offering the warmest welcome in Heidelberg. You are the best IMPRS coordinator we could have asked, with a lot of patience and will to help. Felix and Christian, thank you for the opportunity you offered me to work with you and for being the referees of this thesis. I would like also to thank Prof. Grebel and Prof. Hofmann for accepting to be part of my examination committee.

My special thanks to Mitya for the scientific collaboration, for reading my posters/ talks/ proceedings, for installing/ re-installing/ uninstalling so many programs on my computer and answering all of my questions! Martin, thank you for helping me with the EBL. Then there is aso Stefano, Sabrina, Anna, Andrew, Ervin and Emma for all the scientific, technical and personal discussions! I should also mention the people of "our corridor" for all the

nice company during lunches and tea breaks. Many thanks also to Frank for the German abstract, and Dave and Roland for their corrections in English (wherever there are mistakes, it is my fault!).

Then there are the people that filled my life outside work and created beautiful memories to take with me and made sunnier the life of a Mediterranean girl in cold Heidelberg. Starting for the most important person for me in these years, Matteo. For having this huge amount of patience with me, for being innocent and full of trust on people, his help with PLUTO, his comments on my thesis and a lot more things that can be summarized in "for just being next to me". Thanks to my unique friends, Giovanna, Sara, Viviana, Isabel, Denija, Kelly, Giovanni, Lisa, Emma, Massimo. And also, Giulia, Claudia, Jamie, Baybars, Dusan. There is also Swetlana and Federica that unfortunately I did not have as much time as I wanted to know them better but they are very special to me. A special place has also Bambi and all the girls in her school that the last 2.5 years made me feel comfortable with them although I could not understand almost anything of what they were saying in German (!) and made every Thursday an exciting day! Of course I could not forget to mention my dear ladies, Kelly (again), Kathrin, Sirin, Anna, Cecile, Claudine and Mr. Dave for all the delicious nights of our "cooking club"!

Changing country, I would like to thank my family for having faith on me and my choices. Then there are all of my friends, Anna, Maria, Chryssavghi, Stamatis, Grigoris, Stavros, Giannis, Giorgos and especially Vassilis for all the kind of support they offered me during my stay in Heidelberg.

Last but not least, I would like to specially thank Apostolos Mastichiadis for all the discussions and advice and because without him I wouldn't have been in Heidelberg for a Ph.D!

References

Abdo, A. A., Ackermann, M., Ajello, M., et al. 2009, Astrphysical Journal, 707, 1310

Acciari, V. A., Aliu, E., Arlen, T., et al. 2009, Astrophysical Journal Letters, 693, L104

Aharonian, F., Akhperjanian, A. G., Barres de Almeida, U., et al. 2007, Astronomy and Astrophysics, 475, L9

Aharonian, F., Akhperjanian, A. G., Bazer-Bachi, A. R., et al. 2006, Nature, 440, 1018

Aharonian, F. A. 2000, New Astronomy, 5, 377

Aharonian, F. A. 2004, Very high energy cosmic gamma radiation : a crucial window on the extreme Universe, ed. Aharonian, F. A.

Aharonian, F. A., Atoian, A. M., & Nagapetian, A. M. 1983, Astrofizika, 19, 323

Aharonian, F. A., Khangulyan, D., & Costamante, L. 2008, Monthly Notices of the Royal Astronomical Society, 387, 1206

Aliu, E., Anderhub, H., Antonelli, L. A., et al. 2009, Astrophysical Journal Letters, 692, L29

Bai, J. M., Liu, H. T., & Ma, L. 2009, Astrphysical Journal, 699, 2002

References

Begelman, M. C., Fabian, A. C., & Rees, M. J. 2008, Monthly Notices of the Royal Astronomical Society, 384, L19

Bernstein, R. A., Freedman, W. L., & Madore, B. F. 2002, Astrphysical Journal, 571, 107

Bernstein, R. A., Freedman, W. L., & Madore, B. F. 2005, Astrphysical Journal, 632, 713

Blandford, R. D. & Payne, D. G. 1982, Monthly Notices of the Royal Astronomical Society, 199, 883

Blumenthal, G. R. & Gould, R. J. 1970, Reviews of Modern Physics, 42, 237

Boettcher, M. & Schlickeiser, R. 1997, Astronomy and Astrophysics, 325, 866

Bonometto, S. & Rees, M. J. 1971, Monthly Notices of the Royal Astronomical Society, 152, 21

Böttcher, M. 2007, Astrophysics and Space Science, 309, 95

Bregman, J. N. 1990, Astronomy and Astrophysics Review, 2, 125

Brown, T. M., Kimble, R. A., Ferguson, H. C., et al. 2000, Astronomical Journal, 120, 1153

Cambrésy, L., Reach, W. T., Beichman, C. A., & Jarrett, T. H. 2001, Astrphysical Journal, 555, 563

Cole, S., Lacey, C. G., Baugh, C. M., & Frenk, C. S. 2000, Monthly Notices of the Royal Astronomical Society, 319, 168

Costamante, L., Aharonian, F., Buehler, R., et al. 2009, ArXiv e-prints

Costamante, L., Ghisellini, G., Celotti, A., & Wolter, A. 2002, in Blazar Astrophysics with BeppoSAX and Other Observatories, ed. P. Giommi, E. Massaro, & G. Palumbo, 21–+

Derishev, E. V., Aharonian, F. A., Kocharovsky, V. V., & Kocharovsky, V. V. 2003, Physical Review D, 68, 043003

Dole, H., Lagache, G., Puget, J., et al. 2006, Astronomy and Astrophysics, 451, 417

Dominguez, A., Primack, J. R., Rosario, D. J., et al. 2010, ArXiv e-prints

Dube, R. R., Wickes, W. C., & Wilkinson, D. T. 1979, Astrphysical Journal, 232, 333

Dwek, E. & Arendt, R. G. 1998, Astrophysical Journal Letters, 508, L9

Edelstein, J., Bowyer, S., & Lampton, M. 2000, Astrphysical Journal, 539, 187

Elbaz, D., Cesarsky, C. J., Chanial, P., et al. 2002, Astronomy and Astrophysics, 384, 848

Fall, S. M. 2001, in IAU Symposium, Vol. 204, The Extragalactic Infrared Background and its Cosmological Implications, ed. M. Harwit & M. G. Hauser, 401–+

Fazio, G. G., Ashby, M. L. N., Barmby, P., et al. 2004, Astrophysical Journal Supplement Series, 154, 39

Finkbeiner, D. P., Davis, M., & Schlegel, D. J. 2000, Astrphysical Journal, 544, 81

Franceschini, A., Rodighiero, G., & Vaccari, M. 2008, Astronomy and Astrophysics, 487, 837

Frayer, D. T., Huynh, M. T., Chary, R., et al. 2006, Astrophysical Journal Letters, 647, L9

Giovannini, G., Cotton, W. D., Feretti, L., Lara, L., & Venturi, T. 2001, Astrphysical Journal, 552, 508

References

Gorjian, V., Wright, E. L., & Chary, R. R. 2000, Astrphysical Journal, 536, 550

Gould, R. J. & Schréder, G. P. 1967, Physical Review, 155, 1408

Hauser, M. G., Arendt, R. G., Kelsall, T., et al. 1998, Astrphysical Journal, 508, 25

Hauser, M. G. & Dwek, E. 2001a, Annual Review of Astronomy and Astrophysics, 39, 249

Hauser, M. G. & Dwek, E. 2001b, Annual Review of Astronomy and Astrophysics, 39, 249

Hinton, J. 2009, New Journal of Physics, 11, 055005

Kashlinsky, A., Mather, J. C., Odenwald, S., & Hauser, M. G. 1996, Astrphysical Journal, 470, 681

Kashlinsky, A. & Odenwald, S. 2000, Astrphysical Journal, 528, 74

Katarzyński, K., Ghisellini, G., Tavecchio, F., Gracia, J., & Maraschi, L. 2006, Monthly Notices of the Royal Astronomical Society, 368, L52

Kneiske, T. M., Bretz, T., Mannheim, K., & Hartmann, D. H. 2004, Astronomy and Astrophysics, 413, 807

Kneiske, T. M. & Dole, H. 2010, Astronomy and Astrophysics, 515, A19+

Krennrich, F., Dwek, E., & Imran, A. 2008, Astrophysical Journal Letters, 689, L93

Lagache, G. & Puget, J. L. 2000, Astronomy and Astrophysics, 355, 17

Leinert, C., Bowyer, S., Haikala, L. K., et al. 1998, Astronomy and Astrophysics Supplement, 127, 1

Levenson, L. R. & Wright, E. L. 2008, Astrphysical Journal, 683, 585

Levenson, L. R., Wright, E. L., & Johnson, B. D. 2007, Astrphysical Journal, 666, 34

Lichnerowicz, A. 1967, Relativistic Hydrodynamics and Magnetohydrodynamics, ed. Lichnerowicz, A.

Liu, H. T. & Bai, J. M. 2006, Astrphysical Journal, 653, 1089

Liu, H. T., Bai, J. M., & Ma, L. 2008, Astrphysical Journal, 688, 148

Longair, M. S. 1992, High energy astrophysics. Vol.1: Particles, photons and their detection, ed. Longair, M. S.

Lonsdale, C. 1996, in American Institute of Physics Conference Series, Vol. 348, American Institute of Physics Conference Series, ed. E. Dwek, 147–158

Madau, P. & Pozzetti, L. 2000, Monthly Notices of the Royal Astronomical Society, 312, L9

Martin, C., Hurwitz, M., & Bowyer, S. 1991, Astrphysical Journal, 379, 549

Massaglia, S. 2003, Astrophysics and Space Science, 287, 223

Massaglia, S., Bodo, G., & Ferrari, A. 1996, Astronomy and Astrophysics, 307, 997

Matsumoto, T., Matsuura, S., Murakami, H., et al. 2005, Astrphysical Journal, 626, 31

Mattila, K. 1990, in IAU Symposium, Vol. 139, The Galactic and Extragalactic Background Radiation, ed. S. Bowyer & C. Leinert, 257–268

Mazin, D. & Raue, M. 2007, Astronomy and Astrophysics, 471, 439

McBreen, B. 1979, Astronomy and Astrophysics, 71, L19

Metcalfe, L., Kneib, J., McBreen, B., et al. 2003, Astronomy and Astrophysics, 407, 791

References

Mignone, A., Bodo, G., Massaglia, S., et al. 2007, Astrophysical Journal Supplement Series, 170, 228

Miller, J. S. 1989, in Lecture Notes in Physics, Berlin Springer Verlag, Vol. 334, BL Lac Objects, ed. L. Maraschi, T. Maccacaro, & M.-H. Ulrich, 395–+

Nikishov, A. I. 1962, Sov. Phys. JETP, 14, 393

Norman, M. L., Winkler, K., Smarr, L., & Smith, M. D. 1982, Astronomy and Astrophysics, 113, 285

Papovich, C., Dole, H., Egami, E., et al. 2004, Astrophysical Journal Supplement Series, 154, 70

Peacock, J. 2000, Cosmological Physics (Cambridge University Press), 355

Peebles, P. J. E. 1993, Principles of physical cosmology, ed. Peebles, P. J. E.

Prandini, E., Bonnoli, G., Maraschi, L., Mariotti, M., & Tavecchio, F. 2010, Monthly Notices of the Royal Astronomical Society, 405, L76

Primack, J. R., Gilmore, R. C., & Somerville, R. S. 2008, in American Institute of Physics Conference Series, Vol. 1085, American Institute of Physics Conference Series, ed. F. A. Aharonian, W. Hofmann, & F. Rieger, 71–82

Primack, J. R., Somerville, R. S., Bullock, J. S., & Devriendt, J. E. G. 2001, in American Institute of Physics Conference Series, Vol. 558, American Institute of Physics Conference Series, ed. F. A. Aharonian & H. J. Völk, 463–478

Reimer, A. 2007, Astrphysical Journal, 665, 1023

Reyes, L. C., for the Fermi LAT collaboration, & the VERITAS collaboration. 2009, ArXiv e-prints

Rybicki, G. B. & Lightman, A. P. 1986, Radiative Processes in Astrophysics, ed. Rybicki, G. B. & Lightman, A. P.

Scheck, L., Aloy, M. A., Martí, J. M., Gómez, J. L., & Müller, E. 2002, Monthly Notices of the Royal Astronomical Society, 331, 615

Sitarek, J. & Bednarek, W. 2008, Monthly Notices of the Royal Astronomical Society, 391, 624

Tavecchio, F. & Ghisellini, G. 2008, Monthly Notices of the Royal Astronomical Society, 386, 945

Tavecchio, F., Ghisellini, G., Ghirlanda, G., Costamante, L., & Franceschini, A. 2009, Monthly Notices of the Royal Astronomical Society, 399, L59

Tavecchio, F. & Mazin, D. 2009, Monthly Notices of the Royal Astronomical Society, 392, L40

Toller, G. N. 1983, Astrophysical Journal Letters, 266, L79

Urry, C. M. & Padovani, P. 1995, Publications of the Astronomical Society of the Pacific, 107, 803

Wagner, R. M., Lindfors, E. J., Sillanpää, A., et al. 2009, ArXiv e-prints

Wright, E. L. & Reese, E. D. 2000, Astrphysical Journal, 545, 43

Zirakashvili, V. N. & Aharonian, F. 2007, Astronomy and Astrophysics, 465, 695